

Analysis and Applications of Microstructure and Holey Optical Fibers

by
Jeong I. Kim

Dissertation submitted to the Faculty of the
Virginia Polytechnic Institute and State University
in partial fulfillment of the requirements for the degree of

Doctor of Philosophy
in
Electrical and Computer Engineering

Dr. Ahmad Safaai-Jazi, Co-Chairman
Dr. Anbo Wang, Co-Chairman
Dr. Ting-Chung Poon
Dr. Russell May
Dr. Timothy Pratt
Dr. Werner Kohler

September 10, 2003

Blacksburg, Virginia

Keywords: Photonic Crystal Waveguides, Holey Fibers, Fiber-Optic Communications

Copyright 2003, Jeong I. Kim

Analysis and Applications of Microstructure and Holey Optical Fibers

Jeong I. Kim

ABSTRACT

Microstructure and photonic crystal fibers with periodic as well as random refractive-index distributions are investigated. Two cases corresponding to fibers with one-dimensional (1D) radial index distributions and two-dimensional (2D) transverse index distributions are considered. For 1D geometries with an arbitrary number of cladding layers, exact analytical solutions of guided modes are obtained using a matrix approach. In this part, for random index distributions, the average transmission properties are calculated and the influence of glass/air ratio on these properties is assessed. Important transmission properties of the fundamental mode, including normalized propagation constant, chromatic dispersion, field distributions, and effective area, are evaluated. For 2D geometries, the numerical techniques, FDTD (Finite-Difference Time-Domain) method and FDM (Finite Difference Method), are utilized. First, structures with periodic index distributions are examined. The investigation is then extended to microstructure optical fibers with random index distributions.

Design of 2D microstructure fibers with random air-hole distributions is undertaken with the aim of achieving single-mode guiding property and small effective area. The former is a unique feature of the holey fiber with periodic air-hole arrangement and the latter is a suitable property for nonlinear fiber devices. Measurements of holey fibers with random air-hole distributions constitute an important experimental task of this research. Using a section of a holey fiber fabricated in the draw tower facility at Virginia Tech, measurements of transmission spectra and fiber attenuation are performed. Also, tests results for far-field pattern measurements are presented.

Another objective of this dissertation is to explore new applications for holey fibers with random or periodic hole distributions. In the course of measuring the holey fibers, it was noticed that robust temperature-insensitive pressure sensors can be made with these fibers. This offers an opportunity for new low-cost and reliable pressure fiber-optic sensors. Incorporating gratings into holey fibers in conjunction with the possibility of dynamic tuning offers desirable characteristics with potential applications in communications and sensing. Injecting gases or liquids in holey fibers with gratings changes their transmission characteristics. These changes may be exploited in designing tunable optical filters for communication applications or making gas/liquid sensor devices.

Acknowledgements

I would like to sincerely express appreciation to Dr. Ahmad Safaai-Jazi for suggesting this interesting area. I should not forget his kind advice, support and patience. I also would like to thank Dr. Anbo Wang for allowing me to do my research work in photonics laboratory, which is currently the Center for Photonics Technology. And I would like to thank Dr. Timothy Pratt, Dr. Ting-Chung Poon, Dr. Russell May, and Dr. Werner Kohler for serving on my advisory committee. They gave me helpful impression and knowledge during classes or discussions.

I also would like to express my thankfulness to the Air Force Office of Scientific Research for sponsoring the project during my PhD program. I would like to give thanks to Dr. Roger Stolen, Dr. Gary Pickrell, and Dan Kominsky who have initiated or worked on this interesting project. I also would like to thank all the staffs and colleagues in CPT. They are so much friendly and generous. I have been glad and happy to be there.

To my friends and family, I wish to express thanks for being there always. My father to be in Heaven has inspired me to study and work harder. And my mother has given immeasurable love and concern to me. Their effort and care have given me courage and strength. I would like to thank God for making this dissertation work accomplished.

Table of Contents

Chapter 1 Introduction.....	1
Chapter 2 Background Information and Literature Survey	4
2.1 Introduction	4
2.2 Background Information on Photonic Crystal Structures.....	5
2.2.1 One-Dimensional Photonic Crystal Structures.....	6
2.2.2 Two-Dimensional Photonic Crystal Structures	7
2.2.3 Three-Dimensional Photonic Crystal Structures	10
2.3 Literature Review	11
2.3.1 Theoretical Analysis.....	11
2.3.2 Experimental Analysis.....	13
2.3.3 Applications.....	14
Chapter 3 Analysis on One-Dimensional Cylindrical Photonic Crystal Waveguides	17
3.1 Introduction	17
3.2 Field Solutions.....	18
3.3 Boundary Conditions and Characteristic Equation	21
3.4 Numerical Results	26
3.4.1 Propagation Constant and Chromatic Dispersion.....	26
3.4.2 Field Distributions.....	34
3.4.3 Effective Area.....	38
Chapter 4 Analysis of Two-Dimensional Photonic Crystal and Holey Fibers	41
4.1 Introduction	41
4.2 Finite-Difference Time-Domain (FDTD) Formulation of Maxwell's Equations.....	42

4.2.1 Perfectly Matched Layer (PML)	47
4.2.2 Parameters and Stability	52
4.3 Finite Difference Method (FDM)	54
4.4 Test and Comparison of Methods	57
4.5 Numerical Results for Holey Fibers	60
4.5.1 Propagation Constant	60
4.5.2 Mode Field Distributions	66
4.5.3 Effective Area	72
4.5.4 Chromatic Dispersion	72
Chapter 5 Microstructure Optical Fibers with Random Cladding	
Index Distributions	75
5.1 Microstructure Optical Fibers with One-Dimensional Random Cladding	
Index Distributions	75
5.2 Holey Fibers with Random Air-Hole Distributions	86
5.2.1 Simulation Results by FDTD method	87
5.2.2 Simulation Results by FDM	91
Chapter 6 Measurements of Holey Fibers	96
6.1 Transmission Properties	97
6.2 Loss Measurement	100
6.3 Mode Characteristics and Far-Field Measurement	101
Chapter 7 Applications of Holey Fibers	105
7.1 Grating-Incorporated Holey Fiber	105
7.2 Pressure Sensor Applications	110
Chapter 8 Conclusions and Recommendations for Future Work	116
8.1 Conclusions	116
8.2 Recommendations for Future Work	119

References.....120

Vita.....129

List of Figures

Figure 2.1 One-dimensional photonic crystal structure.....	6
Figure 2.2 Photonic bandgap diagram for Chigrin’s Bragg stack, (a) for TE modes, (b) for TM modes	8
Figure 2.3 Simple examples of two-dimensional photonic crystal structures, (a) with a defect, (b) top view of a unit cell	9
Figure 2.4 Two-dimensional photonic crystal structures, (a) without defect, (b) with defect.....	9
Figure 2.5 An example of three-dimensional photonic crystal structure.....	10
Figure 3.1 Refractive index profiles of one-dimensional cylindrical photonic crystal waveguides, (a) high-index core, (b) low-index core.....	18
Figure 3.2 Normalized propagation constant ($\bar{\beta}$) versus wavelength (λ) of the mode for the fundamental mode of a one-dimensional cylindrical photonic crystal waveguide with high-index core and parameters $r_1 = 1.0 \mu\text{m}$, $d_a = 0.2 \mu\text{m}$, $d_g = 0.3 \mu\text{m}$	28
Figure 3.3 Normalized propagation constant versus wavelength of the mode for the second mode in waveguides with 4 to 20 layers. The geometry and parameters of the waveguide are the same as those in Figure 3.2.....	29

Figure 3.4 Normalized propagation constant ($\bar{\beta}$) versus wavelength (λ) for (a) the fundamental mode and (b) the second mode in a one-dimensional cylindrical photonic crystal waveguide with low-index core and parameters $r_1 = 0.1 \mu\text{m}$, $r_2 = 1.0 \mu\text{m}$, $d_a = 0.2 \mu\text{m}$, $d_g = 0.3 \mu\text{m}$	31
Figure 3.5 Normalized propagation constant ($\bar{\beta}$) versus wavelength (λ) for (a) fundamental mode and (b) the second mode in a one-dimensional cylindrical photonic crystal waveguide with low-index core and parameters $r_1 = 0.3 \mu\text{m}$, $r_2 = 1.0 \mu\text{m}$, $d_a = 0.2 \mu\text{m}$, $d_g = 0.3 \mu\text{m}$	32
Figure 3.6 Variations of chromatic dispersion versus wavelength for the photonic crystal waveguide of Figure 3.2.....	34
Figure 3.7 Plots of electric field components E_r , E_ϕ , and E_z versus radial coordinate r at $\lambda = 1.55 \mu\text{m}$ for the fundamental mode of a photonic crystal waveguide with $N=10$ and parameters the same as those in Figure 3.2.....	35
Figure 3.8 Plots of the electric field component E_ϕ versus radial coordinate at $\lambda = 1.55 \mu\text{m}$ for the fundamental mode of the high-index core photonic crystal waveguide. Waveguide parameters are the same as those in Figure 3.2.....	36
Figure 3.9 Plots of electric field components E_r , E_ϕ , and E_z versus radial coordinate at $\lambda = 1.55 \mu\text{m}$ for the fundamental mode of a low-index core photonic crystal waveguide with $N=9$ and parameters the same as those in (a) Figure 3.4 (a), and (b) Figure 3.5 (a).....	37
Figure 3.10 Effective area versus wavelength for the fundamental mode of 1D cylindrical photonic crystal waveguide with (a) high-index core and parameters, $r_1 = 1.0 \mu\text{m}$, $d_a = 0.2 \mu\text{m}$, and $d_g = 0.3 \mu\text{m}$ and (b) low-index core and parameters, $r_1 = 0.3 \mu\text{m}$, $r_2 = 1.0 \mu\text{m}$, $d_a = 0.2 \mu\text{m}$, and $d_g = 0.3 \mu\text{m}$ with respect to the total number of layers.....	40

Figure 4.1 A unit cell of the FDTD lattice in Cartesian coordinates	43
Figure 4.2 A holey fiber with cross-section diameter of about 40 microns	46
Figure 4.3 FDTD simulation flow chart	53
Figure 4.4 Comparison of normalized propagation constants of the fundamental mode in a test waveguide calculated from exact analytical method, FDTF, and FDM	58
Figure 4.5 Field distributions of the first two modes of the test waveguide	59
Figure 4.6 Geometry of a holey fiber with one layer of air holes	61
Figure 4.7 Normalized propagation constant versus wavelength for the first three modes in a holey fiber with one layer of air holes	62
Figure 4.8 Structure of a holey fiber with three layers of air holes in a hexagonal arrangement	62
Figure 4.9 Normalized propagation constant of the fundamental mode in a holey fiber with a triangular air-hole lattice cladding structure	64
Figure 4.10 Comparison of normalized propagation constants of the fundamental mode in holey fibers with 3-and 5-layer air holes	65
Figure 4.11 Normalized propagation constants of 3-layer holey fibers with different radii	65
Figure 4.12 Normalized propagation constants for 3-layer holey fibers with and without center air hole	66

Figure 4.13 Field distribution for the E_x component of the fundamental mode at $\lambda=1.55 \mu\text{m}$ in a holey fiber with parameters $\Lambda=2.0 \mu\text{m}$ and $d=1.2 \mu\text{m}$ and 3 layers of air holes. (a) 3-D view, (b) top view	67
Figure 4.14 2-D field profiles at $\lambda=1.55 \mu\text{m}$ on planes (a) $x=40$ and (b) $y=40$. Fiber parameters are the same as those in Figure 4.13	68
Figure 4.15 Field distribution for the E_x component of the fundamental mode at $\lambda=15.0 \mu\text{m}$. Fiber parameters are the same as those in Figure 4.13	70
Figure 4.16 Field distribution for the E_x component of the fundamental mode in a holey fiber with a central air hole of $0.3 \mu\text{m}$ radius. Other parameters of the fiber are the same as those in Figure 4.13.....	71
Figure 4.17 Comparison of chromatic dispersions for the test dielectric rod waveguide calculated from exact analytical solution and the FDM analysis	73
Figure 4.18 Waveguide and chromatic dispersions in a holey fiber with 5 layers of air holes and parameters $\Lambda=2.0 \mu\text{m}$ and $d=1.2 \mu\text{m}$	74
Figure 5.1 Comparison of (a) normalized propagation constants, (b) dispersions, and (c) effective areas for reference fiber 1 ($r_1 = 1.0 \mu\text{m}$, $d_a = d_g = 0.3 \mu\text{m}$, and $N = 12$) and its random variations.....	78
Figure 5.2 Comparison of (a) normalized propagation constants, (b) dispersions, and (c) effective areas for reference fiber 2 ($r_1 = 1.0 \mu\text{m}$, $d_a = d_g = 0.1 \mu\text{m}$, and $N = 32$) and its random variations.....	79
Figure 5.3 Comparison of (a) normalized propagation constants, (b) dispersions, and (c) effective areas for reference fiber 3 ($r_1 = 1.0 \mu\text{m}$, $d_a = d_g = 0.07 \mu\text{m}$, and $N = 44$) and its random variations.....	80

Figure 5.4 Comparison of (a) normalized propagation constants, (b) dispersions, and (c) effective areas for reference fiber 4 ($r_1 = 1.0 \mu\text{m}$, $d_a = d_g = 0.04 \mu\text{m}$, and $N = 76$) and its random variations.....	81
Figure 5.5 Comparison of (a) normalized propagation constants, (b) dispersions, and (c) effective areas for reference fiber 5 ($r_1 = 1.0 \mu\text{m}$, $d_a = d_g = 0.02 \mu\text{m}$, and $N = 150$) and its random variations.....	82
Figure 5.6 Comparison of (a) normalized propagation constants, (b) dispersions, and (c) effective areas for a microstructure fiber with glass/air ratio of 0.7/0.3 ($r_1 = 1.0 \mu\text{m}$, $d_a = 0.012 \mu\text{m}$, $d_g = 0.028 \mu\text{m}$ and $N = 150$) and its random variations	84
Figure 5.7 Comparison of (a) normalized propagation constants, (b) dispersions, and (c) effective areas for a microstructure fiber with glass/air ratio of 0.3/0.7 ($r_1 = 1.0 \mu\text{m}$, $d_a = 0.028 \mu\text{m}$, $d_g = 0.012 \mu\text{m}$ and $N = 150$) and its random variations	85
Figure 5.8 Simplified visualization for randomly varying three parameters of air holes.....	88
Figure 5.9 Cross-sectional view of holey fibers with (a) 80 air holes, and (b) 120 air holes, which guide only a single mode	89
Figure 5.10 Spectrum for the holey fiber of Figure 5.9 (b)	89
Figure 5.11 Cross-sectional view of holey fibers with (a) 80 air holes and (b) 120 air holes, which guide a few modes.	90
Figure 5.12 Spectrum for the holey fiber of Figure 5.11 (b)	90
Figure 5.13 A cross-sectional view of an example holey fiber with 200 air holes, which is guiding a few modes	92

Figure 5.14 A cross-sectional view of an example holey fiber with 200 air holes, which is guiding a single mode	92
Figure 5.15 Chromatic dispersion versus wavelength of the fundamental mode for a holey fiber with random air-hole distributions of Figure 5.14	93
Figure 5.16 Field distribution for the E_x component of the fundamental mode at $\lambda=1.55 \mu\text{m}$ for a holey fiber with random air-hole distributions of Figure 5.14. (a) 3D view (b) top view	95
Figure 6.1 The SEM picture of the cross section of a holey fiber with random air-hole distribution	97
Figure 6.2 Transmission spectra of a holey fiber under no-load and load conditions	99
Figure 6.3 Transmission spectra of a conventional multimode fiber under no-load and load conditions.....	99
Figure 6.4 Loss spectrum of a holey fiber fabricated in the draw tower facility of Virginia Tech.....	100
Figure 6.5 Mode spectrum around 632.8-nm wavelength for the holey fiber in Figure 6.1 ..	102
Figure 6.6 Experimental setup around source point for far-field measurement	103
Figure 6.7 Far-field patterns due to interference among propagating modes	104
Figure 7.1 A schematic to realize the grating-incorporated holey fiber	108
Figure 7.2 Comparison of normalized propagation constants of the fundamental modes, when the 5 layers of small holes are occupied by air, carbon dioxide (CO_2), or kerosene for a holey fiber with $\Lambda= 1.0 \mu\text{m}$ and $d = 0.8 \mu\text{m}$	109

Figure 7.3 Reflectivity spectra for the cases when the 5-layer holes of the holey fiber
as in Figure 7.2 are filled with air (red line), CO₂ (green line), or kerosene (blue line)
..... 110

Figure 7.4 Temperature insensitivity of a holey fiber over the wavelength range between
400 nm and 1700 nm 112

Figure 7.5 Pressure sensitivity of a holey fiber over the wavelength range between 400 nm
and 1700 nm at (a) 43°C and (b) 1000°C 113

Figure 7.6 Setup schematic for isostatic pressure test 114

Figure 7.7 Isostatic pressure sensitivity of a holey fiber over the wavelength range between
400 nm and 1700 nm by forcing (a) 2000 PSI and (b) 4000 PSI at room temperature
..... 115

List of Tables

Table 4.1 Effective area for the test dielectric waveguide.....	60
Table 4.2 Effective area for a holey fiber with $\Lambda = 2.0 \mu\text{m}$, $d = 1.2 \mu\text{m}$, $R = 9.0 \mu\text{m}$ and three layers of air holes.....	72
Table 5.1 Parameters of the 5 reference fibers, which are modified to assume random cladding index distributions	76
Table 5.2 Percentage difference in dispersion and effective area	86
Table 5.3 The effective area for a holey fiber with random air-hole distributions, as shown in Figure 5.14.....	94

Chapter 1

Introduction

Optical fibers have many important applications, particularly in communication systems, sensors, medical instrumentation, and many kinds of optical components. During the past three decades, a great deal of effort has been devoted to the development of new types of optical fibers with the aim of improving the performance and reducing the cost of fibers in these applications. A holey fiber is one of the most recent advances in fiber-optic technology that has attracted considerable interest from many researchers around the world. An important feature of a holey fiber is that it can be made of a single material, in contrast to all other types of optical fibers, which are manufactured with two or more materials.

Since the introduction of holey fibers, major research and development efforts have been launched to investigate their transmission properties, explore new applications for them, refine the manufacturing and production of these fibers, and make them cost effective. Because of their novel structure and unique properties that cannot be achieved from conventional step-index fibers, holey fibers continue to be an active area of research in the foreseeable future. Holey fibers have been studied theoretically and experimentally. While many important properties of holey fibers have been studied in recent years, researchers are still exploring ways of better understanding and are developing better tools for the analysis and design of these fibers.

Holey fibers may assume different geometries depending upon the desired applications. A well-known type of holey fiber consists of a solid core region and a cladding region with air holes along the fiber axis in a periodic hexagonal arrangement. The air holes are located at the center

and six corners of each hexagon. Strictly speaking, the holey fiber does not have a clear boundary between the core and cladding regions. However, the central part of holey fibers can be regarded as the core region. In such structures, the cladding might be viewed as a medium of lower average refractive index than the central region. Light propagation in this type of holey fibers is primarily due to the index difference effect. Holey fiber operating based on index difference effect can also be fabricated by drawing a solid silica rod surrounded by several rings of glass tubes. Another type of holey fiber has an air hole in the central region, in which light guidance is believed to be primarily due to the photonic bandgap effect. Holey fiber with higher core index, in which the core is made of doped glass, have also been fabricated. A literature survey on various types of holey fibers will be presented in Chapter 2. Also, background on photonic crystal structures, from which the holey fibers originated, will be discussed.

Holey fibers have been studied both theoretically and experimentally. Moreover, the theoretical analyses of these fibers have been carried out numerically as well as analytically. Clearly with their complex geometry, holey fibers, as two-dimensional photonic crystal structures, do not lend themselves to exact analytical solutions. An exception is one-dimensional photonic crystal waveguides for which such solutions exist.

The advantage of analytical solutions is that they provide much better physical insights than the numerical solutions. In order to gain an understanding of the fundamental properties of photonic crystal waveguides, one-dimensional cylindrical photonic crystal fibers will be studied in Chapter 3. Exact solutions for electromagnetic fields are obtained and essential properties such as dispersion and effective area are investigated.

Nearly the entire research work on holey fibers has been on the types with periodic hole distributions. However, by the virtue of index guiding mechanism, holey fibers with random hole distributions seem to be capable of guiding light and thus be able to offer most functionalities of holey fibers with periodic holes. Holey fibers with random hole distributions can be manufactured using low cost techniques. Recently, researchers at Virginia Tech have developed a sol gel technique for fabrication of holey fibers with random hole distributions. A comprehensive analysis of holey fibers with random hole distributions has not yet been reported in the open literature. One of the objectives of this research is to carry out a thorough investigation of propagation properties of this type of holey fibers.

Since refractive index variations in holey fibers with random hole distributions are arbitrary, numerical techniques are best suited for the analysis of these fibers. Two numerical techniques are employed in this dissertation – FDTD (finite-difference time-domain) method and FDM (finite difference method). These methods have been widely utilized to solve electromagnetic problems numerically. Each technique has certain advantages; for example, in contrast to the FDM, the FDTD method does not generate spurious solutions (modes). Conversely, once the propagation constant of a mode is determined, the calculation of field components is more readily accomplished using the FDM. The utilization of two methods also allows for cross-checking the solutions and thus gaining confidence in the accuracy of results. The formulations of FDTD and FDM techniques are discussed in Chapter 4. Also, in this chapter solutions for holey fibers with periodic hole distributions are presented and compare with published data in order to be assured of the correctness of the formulations and related computer programs. The analyses of one- and two-dimensional holey fibers with random hole distributions are presented in Chapter 5.

Measurements of holey fibers with random air holes constitute an important experimental task of this research. In Chapter 6, measurements of transmission spectrum and absorption and scattering losses in straight fibers are addressed. Also, test results for far-field pattern measurements are presented in this chapter.

Another objective of this dissertation is to explore new applications for holey fibers with random hole distributions. In the course of measuring the holey fibers fabricated in the draw tower facility of Virginia Tech, we discovered that robust temperature-insensitive pressure sensors can be made with these fibers. Incorporating gratings into these holey fibers in conjunction with the possibility of dynamic tuning offers desirable characteristics with potential application in fiber-optic communication systems. Chapter 7 is devoted to discussing the novel applications of holey fibers. Finally, Chapter 8 summarizes the conclusions of this work and outlines the directions for further research.

Chapter 2

Background Information and Literature Survey

2.1 Introduction

Since the invention of photonic crystal fiber in mid 90's, a great deal of interest in the optics and communication communities has focused on this new kind of optical fiber during the last several years. Basically, photonic crystal fibers are optical waveguides with two-dimensional periodic microstructures. If in an optical fiber uniform and identical air holes with some type of periodic arrangement run along the direction of wave propagation, such fiber is referred to as *photonic crystal fiber* (PCF). On the other hand, some investigators have suggested that the air hole arrangement, while maintaining a regular pattern, may not be periodic or may even be completely random in shape, size, and location and yet provide light guidance. This brings another, yet broader nomenclature, the "holey fiber."

Because of its unique structure, which is different from those of the conventional step-index or graded-index fibers, a holey fiber can provide propagation properties not easily attainable from conventional fibers. For example, holey fibers can be designed to be single-mode over the entire wavelength range of interest in optical communications, provide small and nearly constant dispersion over a wide wavelength range, or be a highly nonlinear optical fiber. This novel fiber offers the potential for a variety of applications such as high-power lightguide with low loss, supercontinuum generation, grating-incorporated tunable filter, and polarization maintaining fiber.

In the following sections, first some background information on photonic crystal structures is given. Then, a survey of literature on the analysis, design, measurements, and applications of holey fibers is presented.

2.2 Background Information on Photonic Crystal Structures

A crystal is a periodic arrangement of atoms or molecules. If a small basic building block of atoms or molecules is repeated spatially, a crystal lattice will be formed. As is well known, semiconductor materials have a bandgap between the valence and conduction energy bands. Electrons are forbidden to occupy any energy level within the bandgap. Similarly, if the dielectric constant of a material changes periodically in space, the material is referred to as a photonic crystal. A photonic crystal possesses a forbidden frequency band in which propagation of electromagnetic waves is prohibited. According to the number of directions in which dielectric materials exhibit periodicity, one-, two-, or three-dimensional photonic crystal structures are possible. Scattering of light by photonic crystals can produce many of the analogous phenomena for photons to the atomic potential acting on electrons.

Photonic crystal structures are analogous to normal crystals in which atoms or groups of atoms are arranged in a repeating pattern, except that the repeat period is on the order of a micron rather than a fraction of a nanometer. In 1987, Yablonovitch suggested an application of photonic crystals in semiconductor lasers in order to control the spontaneous emission [1]. This was based on the idea that a photonic structure can be designed to introduce a frequency bandgap coinciding with the spectrum of the spontaneous emission. Other scientists have proposed applications of photonic crystal structures at millimeter and microwave frequencies in order to achieve desired performances for antennas [2-3] and waveguides [4].

The photonic bandgap (PBG) can be defined as *a range of frequencies for which photons are forbidden to travel through a photonic crystal in any direction of propagation*. In analogy to electrons in a crystal, electromagnetic waves propagating in a structure with periodically varying dielectric constants are organized into photonic bands. For certain crystal structures, that have

high enough dielectric contrast ratios, these photonic bands are separated by (photonic) gaps in which propagating states are forbidden.

2.2.1 One-Dimensional Photonic Crystal Structures

The refractive index in a one-dimensional photonic crystal varies along one direction only. An example of a one-dimensional photonic crystal (Chigrin's Bragg stack) is shown in Figure 2.1. The material is periodic in the z-direction with dielectric constants $\epsilon_{r1}=11.56$ for gray and $\epsilon_{r2}=1.96$ for blue, and is homogeneous in the xy-plane. The modes of propagation can be described in terms of $\mathbf{k}_{//}$, k_z , and n , the wave vector in the transverse plane, the wave number in the z-direction, and the band number, respectively.

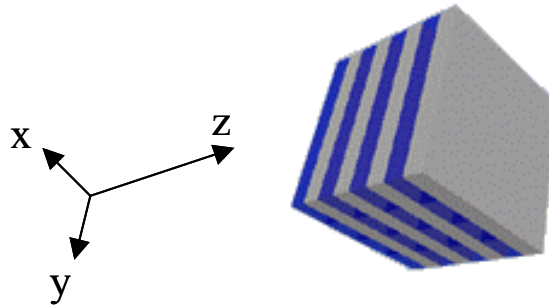


Figure 2.1 One-dimensional photonic crystal structure

Computer simulation of a one-dimensional photonic crystal, with structural variations only in the longitudinal direction in a rectangular coordinate system, was performed using a program that was downloaded from the Internet [5]. Figure 2.2 illustrates the results, which agrees well with those obtained by another researcher [6]. The wave number along the y-axis (ordinate) is related to the incident angle of the light as will be discussed in the next section. The normalized frequency along the x-axis is defined by

$$\text{Normalized frequency} = \frac{\text{Freq. (Hz)} \times \text{Lattice constant (m)}}{\text{Speed of light (m/s)}} \quad (2-1)$$

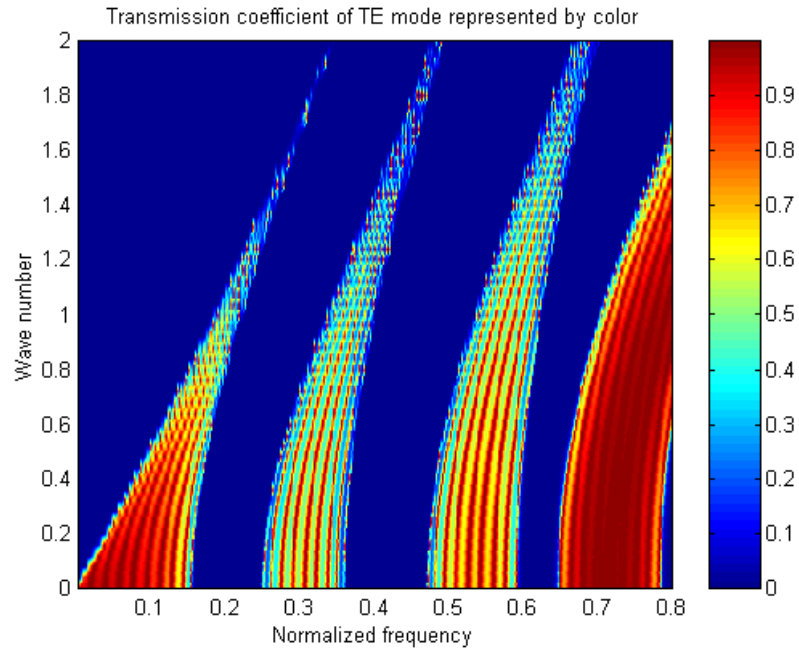
In Figure 2.2, the transmission coefficients for TE and TM modes are shown in color scales. The red color corresponds to a transmission coefficient of 1, while the blue color represents zero transmission or total reflection.

If we examine, say, the normalized frequency regions around 0.2 and 0.4, we notice a frequency gap in which no mode can exist in the (photonic) crystal. Such a gap is known as a photonic bandgap. It can be verified by the electromagnetic variational theorem that the low-frequency modes concentrate their energy in the high- ϵ regions and the high-frequency modes concentrate their energy in the low- ϵ regions [7]. Therefore, it is reasonable to state that a mode just below the gap has its power concentrated in the $\epsilon_{r1}=11.56$ regions, while a mode just above the gap has most of its power in the $\epsilon_{r2}=1.96$ regions.

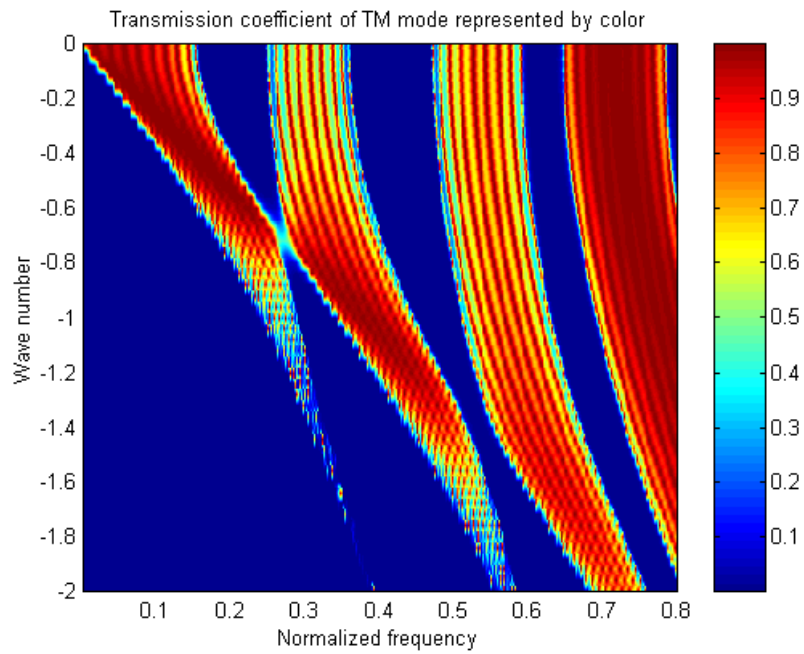
Often the low- ϵ regions are air regions. For this reason, it is convenient to refer to the band above a photonic bandgap as the air band and the band below a gap as the dielectric band. This situation is analogous to the energy band structure of semiconductors, in which the conduction band and the valence band surround the forbidden band.

2.2.2 Two-Dimensional Photonic Crystal Structures

A two-dimensional photonic crystal structure, which is the topic of interest for holey fibers, has a periodic geometry in two directions and is homogeneous in the third. A simple example of a two-dimensional photonic crystal is shown in Figure 2.3. The red column in Figure 2.3 (a) can be thought of as a defect in the photonic crystal, which will be discussed later in this section. Without the red column, Figure 2.3 (b) shows the top view in a unit cell framed in yellow. In this figure, Λ and r represent the lattice constant and the radius of a column, respectively. Figure 2.4 illustrates two other examples of two-dimensional photonic crystals.



(a)



(b)

Figure 2.2 Photonic bandgap diagram for Chigrin's Bragg stack, (a) for TE modes, (b) for TM modes

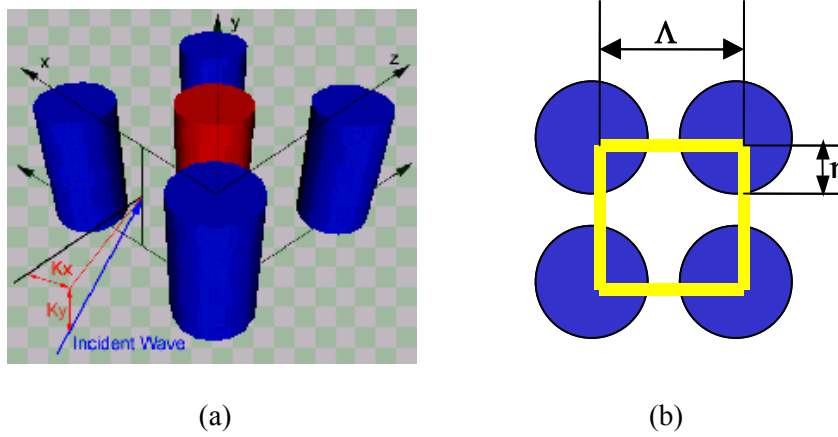


Figure 2.3 Simple examples of two-dimensional photonic crystal structures, (a) with a defect, (b) top view of a unit cell

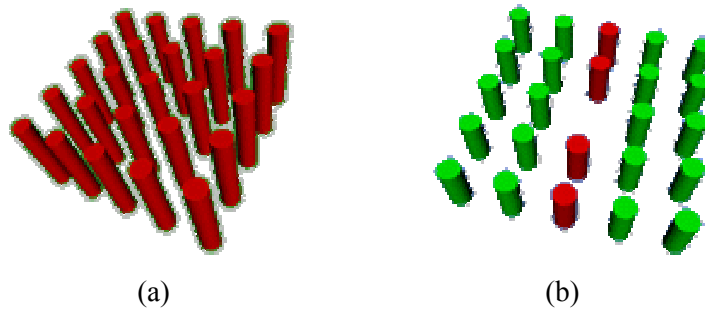


Figure 2.4 Two-dimensional photonic crystal structures, (a) without defect, (b) with defect

If no electromagnetic modes are allowed in the frequency bandgap, what happens when light with a frequency in the photonic bandgap is launched onto the face of the crystal from outside? Now, no purely real wave vector exists for any mode at that frequency. Instead, the wave vector is complex, $\mathbf{k}=\mathbf{k}_r+j\mathbf{k}_i$. The amplitude of the wave decays exponentially into the crystal and establishes evanescent modes. If a defect in the photonic crystal as in Figure 2.4 (b) has the proper size to support a mode in the band gap, then the light cannot escape and the mode will be guided through the defect. Here, it can be said that the periodic structure around the defect acts as

a perfect mirror for light with a frequency within a sharply-defined gap. Such a perfect mirror could not be made without the structural periodicity of the photonic crystal. In Figures 2.3 and 2.4, two-dimensional photonic crystal structures have a square lattice. Other types of two-dimensional photonic crystal structures with a triangular or a honeycomb lattice are possible. Electromagnetic properties of two-dimensional photonic crystal structures can be tailored by changing the lattice constant Λ , radius r , and the dielectric constants.

2.2.3 Three-Dimensional Photonic Crystal Structures

A dielectric structure that is periodic along all three orthogonal axes forms a three-dimensional photonic crystal. Because there are three directions along which the variation of material is permitted, a variety of geometries for three-dimensional photonic crystals are possible. Figure 2.5 shows an example of a three-dimensional photonic crystal. The red balls represent dielectric spheres, which are located at the sites of a diamond lattice. This type of structure can be characterized using the lattice vectors, the dielectric constants of the spheres and the embedded material, and the radius of the spheres. Another types of three-dimensional photonic crystals can be created by eliminating the red balls and connecting the sites with cylindrical dielectric tubes. To localize light in a plane or along a line in these types of photonic crystals, defects can be introduced according to the desired purpose.

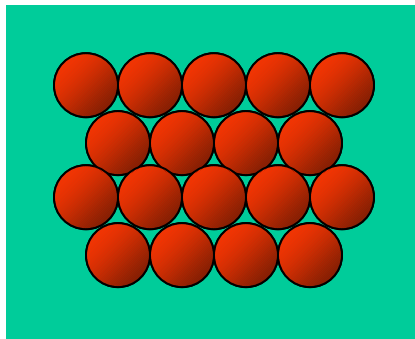


Figure 2.5 An example of three-dimensional photonic crystal structure

2.3 Literature Review

2.3.1 Theoretical Analysis

In order to analyze various types of holey fibers, several techniques have been investigated. Russell et al. employed a scalar-wave approximation to predict the propagation constant of the fundamental mode in holey fibers [8-10]. Then, realizing that guided modes are localized near the core region, they tried to improve their analysis by expressing each modal field as a sum of localized orthogonal functions [9]. They used Hermite-Gaussian functions as a set of orthogonal basis functions and calculated the group-velocity dispersion (GVD) and fields of guided modes. Later, Ferrando et al. used a full vector-wave method to investigate the electromagnetic properties of holey fibers [11-12]. In order to calculate the dispersion relations for guided modes, the two-dimensional (2D) vector-wave equations that describe the electromagnetic propagation of modes in a cylindrical structure were rewritten as an eigensystem for the L operator and its adjoint L^\dagger acting on the magnetic (\mathbf{h}_t) and the electric ($\mathbf{\bar{e}}_t$) transverse field components, respectively.

Combining the best features of the scalar-wave approximation and the full vector-wave technique, Monro et al. introduced a hybrid approach [13-14]. Even though the scalar-wave approach takes advantage of the mode localization property, it cannot be accurate unless the refractive index is represented well. For example, the index profile needs to be described using orthogonal functions such as plane waves or the Hermite-Gaussian functions or stored in a calculation machine for evaluation of large numbers of two-dimensional overlap integrals. On the other hand, the full vector-wave technique can account for any types of complicated cladding structures, permitting accurate modeling of holey fibers. However, it is not efficient, because it does not utilize the localization of guided modes and requires a large number of terms for more accurate solutions. Also, this approach uses periodic boundary conditions to extend the structure to infinity in the transverse plane, thus restricting its applicability to holey fibers that have non-periodic air-hole distributions.

Monro's approach describes the central index defect and the transverse electric field in terms of localized Hermite-Gaussian functions and the air-hole lattice with a Fourier formulation of periodic cosine functions. In the vectorial eigenvalue equations for a transverse two-dimensional

crystal structure, the transverse wave number is a scalar. This technique is applied to determine such properties as mode-field area and waveguide dispersion in terms of the size or arrangement of the air holes. Broeng et al. also utilized Monro's approach to analyze photonic crystal fibers [15-17]. They successfully calculated propagation constant, group-velocity dispersion, bending loss, and transverse field distributions.

Steel and Osgood used a plane-wave expansion method to calculate modal fields and dispersion characteristics [18]. They apply this technique to the vector Helmholtz wave equation with typically 2^{16} transverse basis functions. The weak point of the method is that only the real part of the propagation constant can be calculated. The attenuation coefficient of leaky modes cannot be predicted from this approach. Ranka et al. utilized an imaginary-distance beam-propagation method, which takes into account the polarization effect, to calculate waveguide dispersion and modal field distributions [19].

Using an approach similar to the plane-wave expansion method, White et al. devised a multipole method to calculate modal characteristics of photonic crystal fibers [20]. They utilized a multipole expansion centered on each air hole to enforce boundary conditions accurately. This method alleviates the need for assuming that the periodic structure extends to infinity, which causes the confinement loss in transverse directions to be ignored. This method takes into account both the real and imaginary parts of the propagation constant of a mode. Their method also yields the axial propagation constant in terms of frequency that is an input parameter. Therefore, material dispersion can be readily accounted for. Building on the multipole approach, Fini proposed radial scattering decomposition for modeling microstructure optical fibers [21]. Kuhlmeiy et al. also utilized the multipole method to analyze the modal cutoff in photonic crystal fibers [22]. They found out that all propagation constants are complex and explained how the second mode undergoes behavioral change in the loss and effective area.

For the calculation of chromatic dispersion in photonic crystal fibers, Lægsgaard et al. applied a perturbation approach to account for the frequency dependency of dielectric constants [23]. They also investigated how well dispersion curves converge with respect to supercell size for the fundamental defect modes of both index-guiding and photonic bandgap fiber structures. They point out that a proper choice of the transverse part of the Bloch wave vector in a supercell

calculation can significantly enhance the convergence of dispersion results in terms of the supercell size.

Numerical techniques have also been widely used in the analysis and design of holey fibers. Kim et al. utilized the Galerkin's method with trigonometric functions as basis functions to investigate dispersion characteristics of holey fiber [24]. In exploring the application of holey fiber as a dispersion-compensating fiber, Shen et al. designed photonic crystal fibers which exhibit large negative dispersion up to -474.5 ps/nm-km [25]. They used a combination of vector solver for modal properties and a scaling approach for dispersion characteristics. Guan and coworkers employed a boundary element method in rigorous vector form, formulated in terms of transverse magnetic fields, to determine the dispersion relations of guided modes in holey fibers with one or two layers of holes [26]. Cucinotta et al. utilized the vector finite element method to analyze the effects of hole geometrical variations on propagation properties of holey fibers [27]. They concluded that small perturbations result in critical variations in the polarization status of modes but change the dispersion characteristics very little.

2.3.2 Experimental Analysis

Holey fibers have also been studied experimentally [28-33]. Knight et al. made use of a vidicon camera to illustrate near- and far-field patterns of the guided modes [28]. First, they observed the near-field pattern at the output end of a holey fiber. Then, the near field was converted to the far-field pattern by means of Fourier transformation. They also performed an experiment to demonstrate how scattering properties are related to the air-filling factor (FF) of holey fibers [30]. They illuminated a holey fiber at visible wavelengths under the first-order Bragg condition. What they found was that, as FF becomes larger, the observed Bragg reflected signals get broader.

A fascinating property of holey fibers is that they support only one mode over a wide wavelength range. For this reason, holey fibers are sometimes referred to as endlessly single-mode fibers. In order to verify if holey fibers guide only a single mode, Ranka et al. performed measurements to examine the spatial interference fringe pattern between the collimated output mode of a holey fiber and the output of a standard single-mode fiber [19, 33]. The observation of a clear fringe pattern confirmed the single-mode nature of the holey fiber. In the same papers,

they presented the results for group velocity dispersion by measuring the wavelength-dependent group delay of a 50-cm section of the holey fiber. Similar dispersion measurements have also been performed by Knight et al. [34]. Recently, Gerard et al. conducted near-field probing of an active optical component with photonic crystal structures [35]. They used scanning near-field microscopy to detect the photoluminescence at 1.55- μm wavelength and observed the guiding of the photoluminescence by the suspended membrane and the photonic bandgap effect, which provides the inhibition of the photoluminescence inside a photonic crystal structure.

It has been reported that photonic crystal fibers are able to provide ultra low losses. Recently, Tajima et al. fabricated photonic crystal fibers with high purity silica glass using a dehydration process to reduce the OH absorption loss. They also applied a polishing process to eliminate scratches, while carefully keeping hole positions and sizes uniform along the fiber axis [36-37]. Their holey fibers were measured to have optical losses of 1 dB/km at 1.55- μm wavelength and 2 dB/km at 1.3- μm wavelength. The loss was further reduced to 0.37 dB/km at 1.55- μm wavelength for a 10-km length holey fiber. This loss is much closer to 0.2 dB/km at 1.55- μm wavelength, which is nowadays a typical loss for conventional single-mode fibers. Speaking of loss, Birks et al. studied the bending loss of a photonic crystal fiber by measuring the transmission spectrum in terms of radii of a single-turn bend [8]. Most recently, Zsigri et al. have performed experiment for penalty-free transmission of a 10 Gbit/s non-return-to-zero pulse code modulated signal at 1.55 μm over two 5.6-km photonic crystal fibers with 1.7-dB/km loss, 0.1 ps/km polarization-mode dispersion, and 32 ps/km-nm chromatic dispersion [38].

2.3.3 Applications

Motivated by the insights gained from the experimental and theoretical analyses of holey fibers, researchers have envisioned numerous novel applications for these fibers. For example, it has now been established that holey fibers with effective areas orders of magnitude larger or smaller than the conventional single-mode fibers can be designed. Large effective-area holey fibers are expected to find applications in high power laser delivery [39]. On the other hand, strong nonlinear effects take place in fibers with small effective areas. Potential applications of holey fibers in nonlinear optics include soliton generation and four-wave mixing [12], multimode phase matching [19], generation of ultra-broadband supercontinuum, and pulse compression [33].

A number of researchers have demonstrated the generation of supercontinuum. Among them are: Wadsworth et al. who produced broadband continua extending from 400 nm to 1600 nm by launching femtosecond pulses into a holey fiber [40], and Coen and coworkers demonstrated the generation of a spatially single-mode white-light supercontinuum with a spectral width of more than 600 nm [41]. Broadband continua, which are associated with extremely short pulses, have been used to achieve ultra high-resolution optical tomography. In a case example, 1.3- μm longitudinal resolution in a biological tissue at a center wavelength of 1.1 μm was achieved [42].

Another important application of nonlinear holey fibers is in generation of solitons. Petropoulos et al. developed a single-mode lead silicate glass holey fiber with anomalous dispersion and a high nonlinearity of $\gamma = 640 \text{ W}^{-1}\text{km}^{-1}$ [43]. Using this nonlinear fiber, they achieved a 10-fold pulse compression and Raman solitons at 1.55- μm wavelength. They also demonstrated the operation of a 2R-generative optical switch using only 3.3 meters of a holey fiber which has nonlinear figure of merit 30 times larger than that of a conventional dispersion-shifted silica fiber [44]. The generation of tunable femtosecond soliton pulses by means of photonic crystal fibers in a wavelength range from 780 nm to 900 nm has been reported by Nishizawa et al. [45]. The temporal width of these soliton pulses is as short as 55 fs. They found out that the center wavelength of the soliton pulses can be shifted continuously above 1.1 μm by using much higher power and longer photonic crystal fibers. The delivery of femtosecond pulses by large-core holey fibers, with core diameters of 15 to 25 μm , has been investigated [46]. Although such large-core fibers are multimode, it has been observed that the excitation of fundamental mode is readily achieved and coupling to higher-order modes is weak.

In order to achieve polarization-preserving capability, a holey fiber with elliptical air holes has been proposed [18]. Because of the geometrical uniqueness, this type of holey fibers is reported to provide high birefringence. Hansen et al. evaluated the birefringence of a holey fiber by measuring the fringe envelope as a function of delay for the interference between two polarizations of the fundamental mode [16]. Kergabe et al. developed a method for dynamically tuning the birefringence [47]. They intentionally introduced asymmetry in the holey fiber by selectively filling the air holes with an index-tunable polymer. By changing the temperature around the fiber, the birefringence can be tuned. To enhance the interaction between the core mode and the tunable cladding, the polymer-infused holey optical fiber is tapered to a small

diameter. They report that the polarization beat length varies from 3.6 mm for the minimally tuned case to about 2.2 mm for the maximally birefringent case.

There have been attempts to incorporate Bragg gratings or long-period grating (LPG) into holey fibers. Long-period gratings in holey fibers have been fabricated by micro-collapsing the air holes with heat using a CO₂ laser [48]. To make such optical devices as tunable filters, attenuators, and switches, Kerbage et al. applied fluids along micro-capillary channels inside a holey fiber with long-period gratings in the core [49]. Tunability was achieved by means of dynamic temperature variation [50].

Tapered holey fibers can be used as high efficiency coupling devices. Youk et al. fabricated tapered holey fibers using a fusion splicer and measured the near-field image from the tapered end face with a CCD camera [51]. Tapered holey fibers may also be used for scaling and reshaping of guided mode-field distributions. The numerical analysis of tapered holey fibers has been carried out using the finite-difference time-domain method [52].

Photonic crystal fibers have been successfully applied to active components too. Hougaard et al. designed low pump-power optical amplifiers using photonic crystal fibers [53]. They demonstrated that such amplifiers can provide gains of more than 15 dB at 1.55 μm with optical pump power of less than 0.7 mW. Photonic crystal fiber lasers have received considerable attention in the past few years. Lee et al. demonstrated room-temperature operation of such a laser, which is optically pumped by a vertical-cavity surface-emitting laser at 860 nm [54]. By the use of the photonic crystal membrane, a very small threshold pump power (2.4 mW) was required for the operation of the photonic crystal laser at 1609 nm.

Holey fibers may also be used as sensors. For example, allowing the interaction of light with a gas in the air holes of a holey fiber, one can make gas sensor [28]. Villa et al. developed a one-dimensional photonic crystal sensor based on optical surface waves [55]. They found that a small optical thickness variation of the last layer may change strongly both the frequency and the intensity of the propagating wave.

Chapter 3

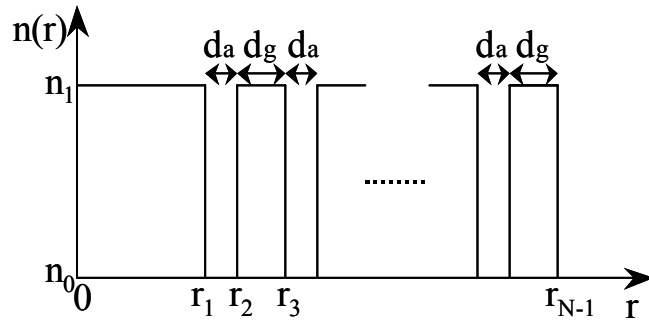
Analysis of One-Dimensional Cylindrical Photonic Crystal Waveguides

3.1 Introduction

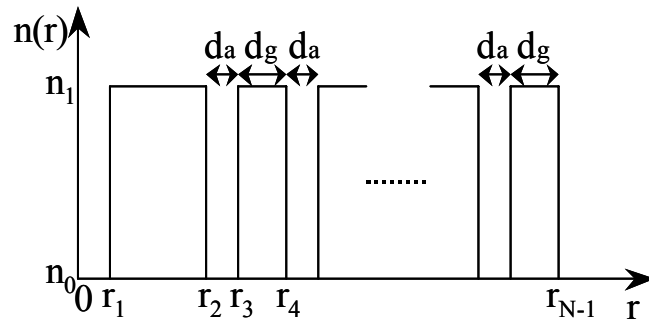
One-dimensional cylindrical photonic crystal waveguides have periodic index variations in the radial direction only. These waveguides consist of a central core surrounded by a cladding composed of alternating-index and equal-thickness rings. Two cases corresponding to high-index core and low-index core are considered. The refractive index profiles for these two geometries are shown in Figure 3.1. An advantage of one-dimensional photonic crystal waveguides with index profiles as in Figure 3.1 is that exact analytical solutions exist for them. This allows more accurate simulations of transmission properties of such fibers. Furthermore, the index profile of Figure 3.1 (a) can serve as an approximate model for holey fibers whose cladding is formed by assembling a large number of thin glass tubes around a solid core. The analysis presented in this chapter will be later extended in Chapter 5 to the case where the cladding has random index variations. The analysis of one-dimensional photonic crystal waveguides with random cladding index variations, in fact, constitutes the first step toward the investigation of holey fibers with random hole distributions.

In the following sections, first exact solutions for the electromagnetic fields of guided modes are derived. Then, the eigenvalue equation, from which propagation constants of different modes can be calculated, is determined by imposing the boundary conditions. A matrix approach is used

in the derivation of eigenvalue equation. Important transmission properties of the fundamental mode such as normalized propagation constant, chromatic dispersion, field distributions, and effective area are examined for example cases.



(a)



(b)

Figure 3.1 Refractive index profiles of one-dimensional cylindrical photonic crystal waveguides, (a) high-index core, (b) low-index core

3.2 Field Solutions

Since the refractive index difference between the alternating-index layers of the cladding can be large, it is necessary to employ a full vector-wave approach instead of a scalar-wave approximation to analyze a cylindrical photonic crystal waveguide. Let us consider one such optical waveguide consisting of N homogeneous, isotropic, linear, and circularly cylindrical

dielectric regions as indicated in Figure 3.1. The i -th region; $i = 1, 2, \dots, N$, is characterized by a refractive index n_i , an inner radius r_{i-1} , and an outer radius r_i . Since the index profile is periodic, n_i can assume two values; either a high index (silica glass) or a low index (air) value.

Electromagnetic fields are solutions of the vector wave equation in a cylindrical coordinate system. For these waveguides exact analytical solutions for guided modes exist. The approach to obtaining field solutions involves the following steps: (a) A cylindrical coordinate system (r, φ, z) with the z -axis coinciding the axis of the waveguide is chosen, then the solutions for axial field components E_z and H_z are determined using the method of separation of variables. (b) Transverse field components E_φ , H_φ , E_r , and H_r are calculated from the axial components. (c) Boundary conditions at $N-1$ boundaries are imposed. This step yield two sets of results, (1) an eigenvalue or characteristic equation from which modal propagation constants are obtained, (2) all field amplitude coefficients are expressed in terms of one chosen as an independent coefficient.

It is well established that for circularly cylindrical waveguides the radial dependence of electromagnetic fields is governed by the Bessel differential equation, hence the solutions are described in terms of the Bessel and the modified Bessel functions [56]. On the other hand, the dependence of the fields on the azimuthal coordinate φ is described in terms of sinusoidal functions $\cos(n\varphi)$ and $\sin(n\varphi)$ where n is an integer constant. For propagation in the positive z -direction, the dependence of fields on the axial coordinate z is as $\exp(-j\beta z)$, where β is the axial propagation constant. This term is common to all field components and, for brevity, is dropped from field expressions. In fact, the attributes of field solutions are the same as those in multiple-clad fibers with such large effective-area and dispersion-flattened fibers [57-58]. Accordingly, the solutions for the axial field components in the i -th region are summarized as

$$\left. \begin{aligned} E_z^i &= \left[A_i Z_{n,i}(k_i r) + B_i \bar{Z}_{n,i}(k_i r) \right] \cos(n\varphi + \varphi_0) \\ H_z^i &= \left[C_i Z_{n,i}(k_i r) + D_i \bar{Z}_{n,i}(k_i r) \right] \sin(n\varphi + \varphi_0) \end{aligned} \right\}, r_{i-1} < r < r_i, \quad (3-1a)$$

where

$$Z_{n,i}(k_i r) = \begin{cases} J_n(k_i r), & n_i = n_1, \\ I_n(k_i r), & n_i = n_0, \end{cases} \quad (3-1b)$$

$$\bar{Z}_{n,i}(k_i r) = \begin{cases} Y_n(k_i r), & n_i = n_1, \\ K_n(k_i r), & n_i = n_0, \end{cases} \quad (3-1c)$$

$$k_i = k_0 \sqrt{|n_i^2 - \bar{\beta}^2|}, \quad (3-1d)$$

and $k_0 = 2\pi/\lambda$ is the free-space wave number, J_n and Y_n are the Bessel functions of the first and the second kinds, respectively, I_n and K_n are the modified Bessel functions of the first and the second kinds, respectively, φ_0 is a constant which may be set equal to 0 or $\pi/2$ to yield $\cos(n\varphi)$ or $\sin(n\varphi)$, and A_i , B_i , C_i , and D_i are constant amplitude coefficients.

The solutions for the transverse field components (E_r , E_φ , H_r , and H_φ) are readily determined using the relationships that describe transverse components in terms of axial components. The results are as summarized below:

$$E_r^i = \frac{-jk_0}{q_i^2} \left\{ \bar{\beta}k_i \left[A_i Z_{n,i}'(k_i r) + B_i \bar{Z}_{n,i}'(k_i r) \right] + \frac{Z_0 n}{r} \left[C_i Z_{n,i}(k_i r) + D_i \bar{Z}_{n,i}(k_i r) \right] \right\} \cos(n\varphi + \varphi_0) \quad (3-2)$$

$$E_\varphi^i = \frac{jk_0}{q_i^2} \left\{ \frac{\bar{\beta}n}{r} \left[A_i Z_{n,i}(k_i r) + B_i \bar{Z}_{n,i}(k_i r) \right] + k_i Z_0 \left[C_i Z_{n,i}'(k_i r) + D_i \bar{Z}_{n,i}'(k_i r) \right] \right\} \sin(n\varphi + \varphi_0) \quad (3-3)$$

$$H_r^i = \frac{-jk_0}{q_i^2} \left\{ \frac{n_i^2 n}{Z_0 r} \left[A_i Z_{n,i}(k_i r) + B_i \bar{Z}_{n,i}(k_i r) \right] + \bar{\beta}k_i \left[C_i Z_{n,i}'(k_i r) + D_i \bar{Z}_{n,i}'(k_i r) \right] \right\} \sin(n\varphi + \varphi_0) \quad (3-4)$$

$$H_{\varphi}^i = \frac{-jk_0}{q_i^2} \left\{ \frac{k_i n_i^2}{Z_0} \left[A_i Z_{n,i}'(k_i r) + B_i \bar{Z}_{n,i}'(k_i r) \right] + \frac{\bar{\beta} n}{r} \left[C_i Z_{n,i}(k_i r) + D_i \bar{Z}_{n,i}(k_i r) \right] \right\} \cos(n\varphi + \varphi_0) \quad (3-5)$$

where $Z_0 = 120\pi$ (Ω) and $q_i^2 = k_i^2 v_i$ with $v_i = \begin{cases} +1, & \text{for } n_i > \bar{\beta} \\ -1, & \text{for } n_i < \bar{\beta} \end{cases}$.

In the central core region that includes the waveguide axis ($r = 0$), Y_n and K_n functions must be excluded from the solution, because they are undefined when their arguments become zero. Also, in the outer cladding layer; i.e. when $i=N$, the solutions include only K_n functions to ensure that fields remain bounded as r approaches infinity.

3.3 Boundary Conditions and Characteristic Equation

Once complete field solutions for both electric and magnetic fields are obtained, boundary conditions are applied. Boundary conditions in this problem amount to the continuity of tangential components of electric and magnetic fields at $N-1$ boundaries; namely, at $r = r_i$; $i = 1, 2, \dots, N-1$. In each layer, there are 4 tangential field components, E_z , H_z , E_{φ} , and H_{φ} , thus the imposition of boundary conditions results in $4(N-1)$ equations. These equations may be viewed as a homogeneous system of $4N-4$ equations in terms of $4N$ amplitude coefficients. The boundary condition for the axial component E_z at $r = r_i$ yields,

$$A_i Z_{n,i}(U_i) + B_i \bar{Z}_{n,i}(U_i) = A_{i+1} Z_{n,i+1}(W_i) + B_{i+1} \bar{Z}_{n,i+1}(W_i) \quad (3-6)$$

where $U_i = k_i r_i$ and $W_i = k_{i+1} r_i$. Similarly, the boundary condition for H_z at $r = r_i$ results in

$$C_i Z_{n,i}(U_i) + D_i \bar{Z}_{n,i}(U_i) = C_{i+1} Z_{n,i+1}(W_i) + D_{i+1} \bar{Z}_{n,i+1}(W_i) \quad (3-7)$$

The corresponding boundary conditions for E_ϕ and H_ϕ at $r = r_i$ lead to

$$\begin{aligned} & \frac{1}{k_i v_i} \left\{ \frac{\bar{\beta} n}{U_i} [A_i Z_{n,i}(U_i) + B_i \bar{Z}_{n,i}(U_i)] + Z_0 [C_i Z_{n,i}'(U_i) + D_i \bar{Z}_{n,i}'(U_i)] \right\} \\ &= \frac{1}{k_{i+1} v_{i+1}} \left\{ \frac{\bar{\beta} n}{W_i} [A_{i+1} Z_{n,i+1}(W_i) + B_{i+1} \bar{Z}_{n,i+1}(W_i)] + Z_0 [C_{i+1} Z_{n,i+1}'(W_i) + D_{i+1} \bar{Z}_{n,i+1}'(W_i)] \right\} \end{aligned} \quad (3-8)$$

$$\begin{aligned} & \frac{1}{k_i v_i} \left\{ \frac{n_i^2}{Z_0} [A_i Z_{n,i}'(U_i) + B_i \bar{Z}_{n,i}'(U_i)] + \frac{\bar{\beta} n}{U_i} [C_i Z_{n,i}(U_i) + D_i \bar{Z}_{n,i}(U_i)] \right\} \\ &= \frac{1}{k_{i+1} v_{i+1}} \left\{ \frac{n_{i+1}^2}{Z_0} [A_{i+1} Z_{n,i+1}'(W_i) + B_{i+1} \bar{Z}_{n,i+1}'(W_i)] + \frac{\bar{\beta} n}{W_i} [C_{i+1} Z_{n,i+1}(W_i) + D_{i+1} \bar{Z}_{n,i+1}(W_i)] \right\} \end{aligned} \quad (3-9)$$

Equations (3-6) to (3-9) can be viewed as a system of four equation and four unknowns. Considering the coefficients A_{i+1} , B_{i+1} , C_{i+1} , and D_{i+1} as unknowns, the solutions in terms of A_i , B_i , C_i , and D_i can be expressed in a matrix form as follows:

$$\begin{bmatrix} A_{i+1} \\ B_{i+1} \\ C_{i+1} \\ D_{i+1} \end{bmatrix} = \begin{bmatrix} a_{11}^i & a_{12}^i & a_{13}^i & a_{14}^i \\ a_{21}^i & a_{22}^i & a_{23}^i & a_{24}^i \\ a_{31}^i & a_{32}^i & a_{33}^i & a_{34}^i \\ a_{41}^i & a_{42}^i & a_{43}^i & a_{44}^i \end{bmatrix} \begin{bmatrix} A_i \\ B_i \\ C_i \\ D_i \end{bmatrix} \quad (3-10)$$

where

$$a_{11}^i = \left(\frac{1}{\eta_{2i} - \bar{\eta}_{2i}} \right) \left[\left(\frac{v_{i+1}}{v_i} \right) \left(\frac{n_i}{n_{i+1}} \right)^2 \eta_{1i} - \bar{\eta}_{2i} \right] \left[\frac{Z_{n,i}(U_i)}{Z_{n,i+1}(W_i)} \right] \quad (3-11a)$$

$$a_{12}^i = \left(\frac{1}{\eta_{2i} - \bar{\eta}_{2i}} \right) \left[\left(\frac{v_{i+1}}{v_i} \right) \left(\frac{n_i}{n_{i+1}} \right)^2 \bar{\eta}_{1i} - \bar{\eta}_{2i} \right] \left[\frac{\bar{Z}_{n,i}(U_i)}{Z_{n,i+1}(W_i)} \right] \quad (3-11b)$$

$$a_{13}^i = \left(\frac{1}{\eta_{2i} - \bar{\eta}_{2i}} \right) \left[\frac{Z_0 \bar{\beta} n \xi}{n_{i+1}^2} \right] \left[\frac{Z_{n,i}(U_i)}{Z_{n,i+1}(W_i)} \right] \quad (3-11c)$$

$$a_{14}^i = \left(\frac{1}{\eta_{2i} - \bar{\eta}_{2i}} \right) \left[\frac{Z_0 \bar{\beta} n \xi}{n_{i+1}^2} \right] \left[\frac{\bar{Z}_{n,i}(U_i)}{Z_{n,i+1}(W_i)} \right] \quad (3-11d)$$

$$a_{21}^i = - \left(\frac{1}{\eta_{2i} - \bar{\eta}_{2i}} \right) \left[\left(\frac{v_{i+1}}{v_i} \right) \left(\frac{n_i}{n_{i+1}} \right)^2 \eta_{1i} - \eta_{2i} \right] \left[\frac{Z_{n,i}(U_i)}{\bar{Z}_{n,i+1}(W_i)} \right] \quad (3-11e)$$

$$a_{22}^i = - \left(\frac{1}{\eta_{2i} - \bar{\eta}_{2i}} \right) \left[\left(\frac{v_{i+1}}{v_i} \right) \left(\frac{n_i}{n_{i+1}} \right)^2 \bar{\eta}_{1i} - \eta_{2i} \right] \left[\frac{\bar{Z}_{n,i}(U_i)}{\bar{Z}_{n,i+1}(W_i)} \right] \quad (3-11f)$$

$$a_{23}^i = - \left(\frac{1}{\eta_{2i} - \bar{\eta}_{2i}} \right) \left[\frac{Z_0 \bar{\beta} n \xi}{n_{i+1}^2} \right] \left[\frac{Z_{n,i}(U_i)}{\bar{Z}_{n,i+1}(W_i)} \right] \quad (3-11g)$$

$$a_{24}^i = - \left(\frac{1}{\eta_{2i} - \bar{\eta}_{2i}} \right) \left[\frac{Z_0 \bar{\beta} n \xi}{n_{i+1}^2} \right] \left[\frac{\bar{Z}_{n,i}(U_i)}{\bar{Z}_{n,i+1}(W_i)} \right] \quad (3-11h)$$

$$a_{31}^i = \left(\frac{1}{\eta_{2i} - \bar{\eta}_{2i}} \right) \left[\frac{\bar{\beta} n \xi}{Z_0} \right] \left[\frac{Z_{n,i}(U_i)}{Z_{n,i+1}(W_i)} \right] \quad (3-11i)$$

$$a_{32}^i = \left(\frac{1}{\eta_{2i} - \bar{\eta}_{2i}} \right) \left[\frac{\bar{\beta} n \xi}{Z_0} \right] \left[\frac{\bar{Z}_{n,i}(U_i)}{Z_{n,i+1}(W_i)} \right] \quad (3-11j)$$

$$a_{33}^i = \left(\frac{1}{\eta_{2i} - \bar{\eta}_{2i}} \right) \left[\left(\frac{v_{i+1}}{v_i} \right) \eta_{1i} - \bar{\eta}_{2i} \right] \left[\frac{Z_{n,i}(U_i)}{Z_{n,i+1}(W_i)} \right] \quad (3-11k)$$

$$a_{34}^i = \left(\frac{1}{\eta_{2i} - \bar{\eta}_{2i}} \right) \left[\left(\frac{v_{i+1}}{v_i} \right) \bar{\eta}_{1i} - \bar{\eta}_{2i} \right] \left[\frac{\bar{Z}_{n,i}(U_i)}{Z_{n,i+1}(W_i)} \right] \quad (3-11l)$$

$$a_{41}^i = - \left(\frac{1}{\eta_{2i} - \bar{\eta}_{2i}} \right) \left[\frac{\bar{\beta} n \xi}{Z_0} \right] \left[\frac{Z_{n,i}(U_i)}{\bar{Z}_{n,i+1}(W_i)} \right] \quad (3-11m)$$

$$a_{42}^i = - \left(\frac{1}{\eta_{2i} - \bar{\eta}_{2i}} \right) \left[\frac{\bar{\beta} n \xi}{Z_0} \right] \left[\frac{\bar{Z}_{n,i}(U_i)}{\bar{Z}_{n,i+1}(W_i)} \right] \quad (3-11n)$$

$$a_{43}^i = - \left(\frac{1}{\eta_{2i} - \bar{\eta}_{2i}} \right) \left[\left(\frac{v_{i+1}}{v_i} \right) \eta_{1i} - \eta_{2i} \right] \left[\frac{Z_{n,i}(U_i)}{\bar{Z}_{n,i+1}(W_i)} \right] \quad (3-11o)$$

$$a_{44}^i = -\left(\frac{1}{\eta_{2i} - \bar{\eta}_{2i}}\right) \left[\left(\frac{v_{i+1}}{v_i}\right) \bar{\eta}_{1i} - \eta_{2i} \right] \left[\frac{\bar{Z}_{n,i}(U_i)}{\bar{Z}_{n,i+1}(W_i)} \right] \quad (3-11p)$$

where

$$\xi = \left(\frac{v_{i+1}}{v_i}\right) \left(\frac{1}{U_i^2}\right) - \left(\frac{1}{W_i^2}\right) \quad (3-12a)$$

$$\eta_{1i} = \frac{Z_{n,i}'(U_i)}{U_i \cdot Z_{n,i}(U_i)} \quad (3-12b)$$

$$\bar{\eta}_{1i} = \frac{\bar{Z}_{n,i}'(U_i)}{U_i \cdot \bar{Z}_{n,i}(U_i)} \quad (3-12c)$$

$$\eta_{2i} = \frac{Z_{n,i+1}'(W_i)}{W_i \cdot Z_{n,i+1}(W_i)} \quad (3-12d)$$

$$\bar{\eta}_{2i} = \frac{\bar{Z}_{n,i+1}'(W_i)}{W_i \cdot \bar{Z}_{n,i+1}(W_i)} \quad (3-12e)$$

Successive application of (3-10) to boundaries at r_i ; $i = 1, 2, \dots, N-1$, leads to the following expression which relates the amplitude coefficients for the outer cladding region to those for the central core,

$$\begin{aligned} \begin{bmatrix} A_N \\ B_N \\ C_N \\ D_N \end{bmatrix} &= \prod_{i=1}^{N-1} \begin{bmatrix} a_{11}^i & a_{12}^i & a_{13}^i & a_{14}^i \\ a_{21}^i & a_{22}^i & a_{23}^i & a_{24}^i \\ a_{31}^i & a_{32}^i & a_{33}^i & a_{34}^i \\ a_{41}^i & a_{42}^i & a_{43}^i & a_{44}^i \end{bmatrix} \begin{bmatrix} A_1 \\ B_1 \\ C_1 \\ D_1 \end{bmatrix} \\ &= \begin{bmatrix} b_{11} & b_{12} & b_{13} & b_{14} \\ b_{21} & b_{22} & b_{23} & b_{24} \\ b_{31} & b_{32} & b_{33} & b_{34} \\ b_{41} & b_{42} & b_{43} & b_{44} \end{bmatrix} \begin{bmatrix} A_1 \\ B_1 \\ C_1 \\ D_1 \end{bmatrix} \end{aligned} \quad (3-13)$$

However, in the outer cladding region $A_N = C_N = 0$ in order to prevent fields to increase exponentially, and in the central core $B_1 = D_1 = 0$ in order to ensure that the fields remain finite at $r=0$. Thus, only the following terms remain not to be zero:

$$b_{11}A_1 + b_{13}C_1 = 0 \quad (3-14a)$$

$$b_{31}A_1 + b_{33}C_1 = 0 \quad (3-14b)$$

For the above homogeneous system of equations to have nontrivial solutions, the determinant of coefficients must be zero. That is,

$$b_{11}b_{33} - b_{31}b_{13} = 0 \quad (3-15)$$

Equation (3-15) is indeed the characteristic (or eigenvalue) equation from which the axial propagation constant β can be determined. This equation may be expressed as a function of waveguide parameters (radii and indices of various regions), wavelength λ , the azimuthal number n and the propagation constant as given below:

$$f(\lambda, \bar{\beta}, n, n_1, n_0, r_i; i = 1, 2, \dots, N-1) = 0 \quad (3-16)$$

where $\bar{\beta}$ is the normalized propagation constant defined as

$$\bar{\beta} = \beta / k_0 = \beta \lambda / 2\pi \quad (3-17)$$

For a given light source powering the waveguide the wavelength of operation λ is known. Also, for a given waveguide the dimensions $r_i; i = 1, 2, \dots, N-1$ and refractive indices n_1 and n_0 are known. Thus, upon selecting an integer value for the azimuthal number n (for example $n = 1$ for the fundamental HE_{11} mode), (3-16) becomes an equation in which only $\bar{\beta}$ is unknown. Solving this equation the normalized propagation constant for a desired mode is obtained.

Finally, the above analysis allows all field coefficients to be expressed in terms of one amplitude coefficient chosen as independent variable. For example, if A_1 is chosen as the independent coefficient from (3-14a), we will obtain $C_1 = -b_{11}A_1 / b_{13}$. Then, with successive applications of (3-10) amplitude coefficients for a particular mode in all layers of the waveguide can be calculated in terms of A_1 .

3.4 Numerical Results

Using the field solutions and the characteristic equation derived in the previous sections, electromagnetic properties of one-dimensional cylindrical photonic crystal waveguides are examined for some example cases. First, modal characteristics are investigated, which enable us to directly calculate chromatic dispersion for the fundamental mode. Next, the electric field components, particularly their radial distributions, are studied. Using the field solutions, the effective area that is a key parameter in nonlinear fiber optics is evaluated.

3.4.1 Propagation Constant and Chromatic Dispersion

The normalized propagation constant $\bar{\beta}$ is calculated by solving the characteristic equation given in (3-15) numerically. An example waveguide with dimensions $r_1 = 1.0 \mu\text{m}$, $d_a = 0.2 \mu\text{m}$, and $d_g = 0.3 \mu\text{m}$ is considered for the numerical analysis. This set of parameters, as will be noted later, provides desirable results for chromatic dispersion and cutoff wavelength pertaining to the fundamental mode. It is assumed that the high-index material of this waveguide is pure fused silica (100 m/o SiO_2) with refractive index n_1 , while the low-index region is air. To account for the material dispersion effect of the glass, its refractive index is expressed as a function of wavelength according to the Sellmeier's equation [59],

$$n_1(\lambda) = \left[1 + \sum_{j=1}^3 \frac{A_j \lambda^2}{\lambda^2 - \lambda_j^2} \right]^{1/2} \quad (3-18)$$

where A_j and λ_j are material constants, which for pure fused silica assume the following values:

$$A_1 = 0.6961663, \lambda_1 = 0.0684043$$

$$A_2 = 0.4079426, \lambda_2 = 0.1162414$$

$$A_3 = 0.8974794, \lambda_3 = 9.8961610$$

Figure 3.2 illustrates variations of the normalized propagation constant versus wavelength for the fundamental HE_{11} mode in the example photonic crystal waveguide. The total number of layers, N , varies from 4 to 20. It is noted that the normalized propagation constant changes from about 1.32 to 1.41 over a wavelength range between 1.0 μm and 2.0 μm . Furthermore, it is observed that the normalized propagation constant when $N = 8$ is nearly the same as those when $N = 10, 14,$ and 20 . In other words, it seems that once the number of cladding layers is large enough, adding more cladding layers does not affect the propagation constant significantly. This behavior is attributed to the fact that fields decay exponentially in the cladding layers, and the layers beyond where the fields become sufficiently small have little influence on propagation properties.

In order to examine the wavelength range for single-mode operation, the normalized propagation constant of TE_{01} mode, which is the second propagating mode, is calculated. It is emphasized that for this mode the azimuthal number (n) is zero. Figure 3.3 shows variations of normalized propagation constant versus wavelength for the second mode of the example waveguide. It is observed that $\bar{\beta}$ values of the second mode are much lower than those of the first mode. The convergence of mode characteristics occurs more slowly for the same number of layers. This is expected, because for higher-order modes fields in the cladding region decay more slowly. However, for any mode beyond a certain number of layers propagation properties remain essentially unchanged. This ‘saturation’ number of layers (N_{sat}) is generally larger for higher-order modes.

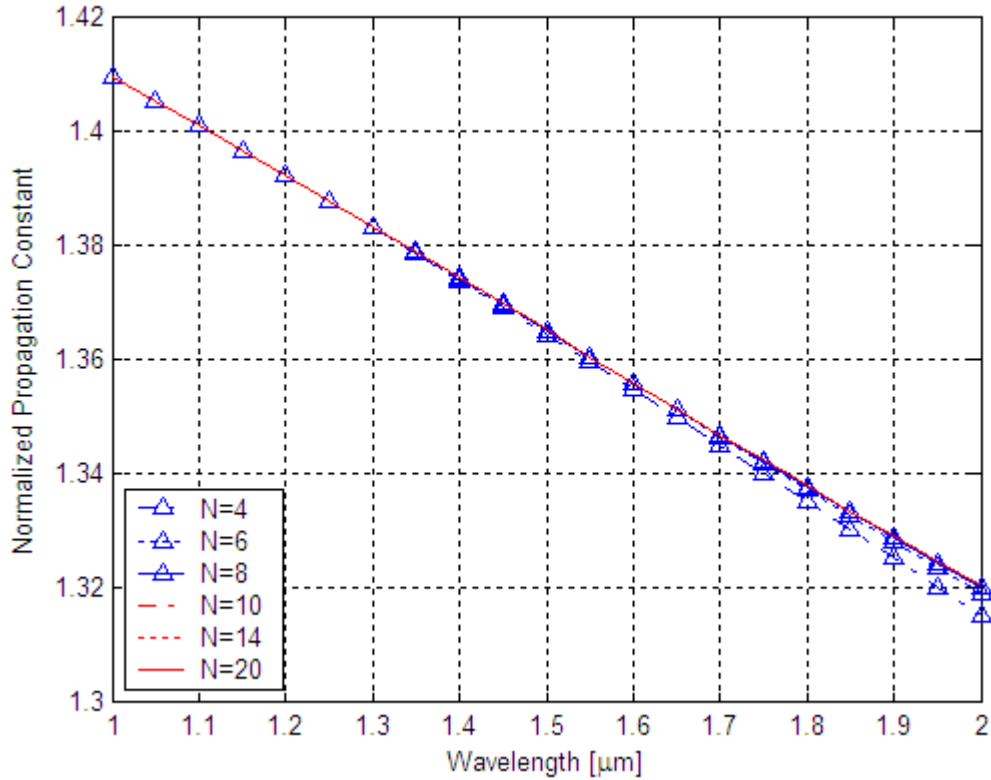


Figure 3.2 Normalized propagation constant ($\bar{\beta}$) versus wavelength (λ) of the mode for the fundamental mode of a one-dimensional cylindrical photonic crystal waveguide with high-index core and parameters $r_1 = 1.0 \mu\text{m}$, $d_a = 0.2 \mu\text{m}$, $d_g = 0.3 \mu\text{m}$.

Another interesting observation from Figures 3.2 and 3.3 is that deviations of the normalized propagation constants with respect to the total number of layers, when the operating wavelength is shorter around $1 \mu\text{m}$, are smaller than these of the normalized propagation constants, when the operating wavelength is longer around $2 \mu\text{m}$. The reason is that when the operating wavelength is shorter, electromagnetic fields are more confined to the core region as discussed in the next section and only the core region has major impact on the propagation properties. On the other hand, when the operating wavelength is longer, fields spread more to the cladding region and the index profile of the cladding region has more influence on the normalized propagation constant.

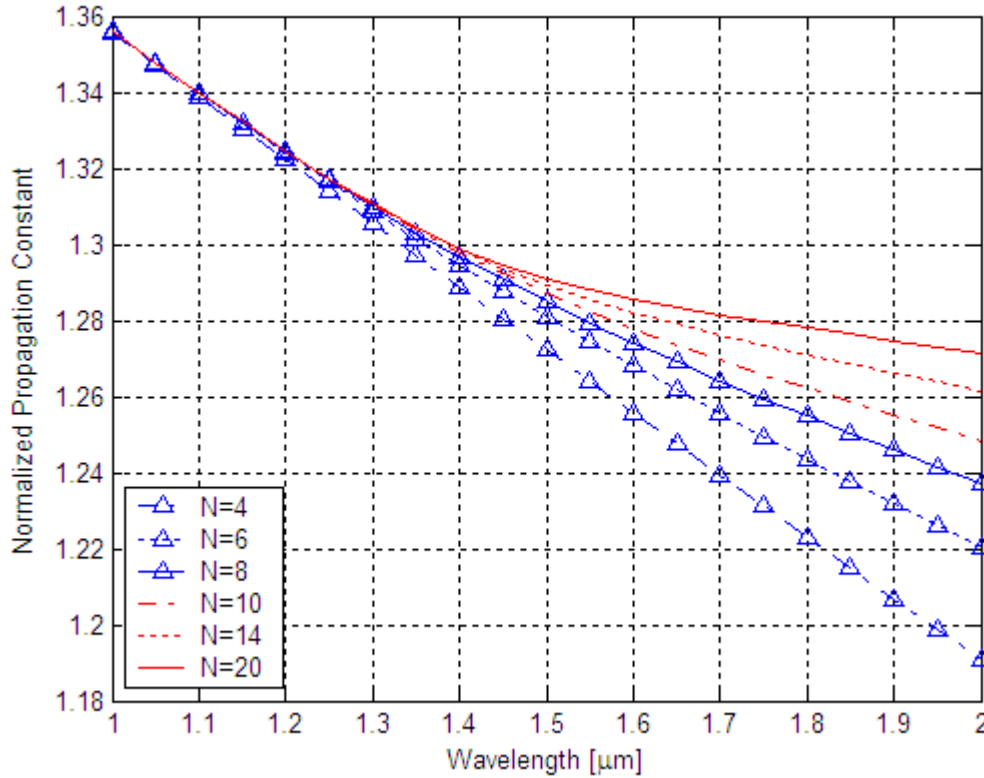


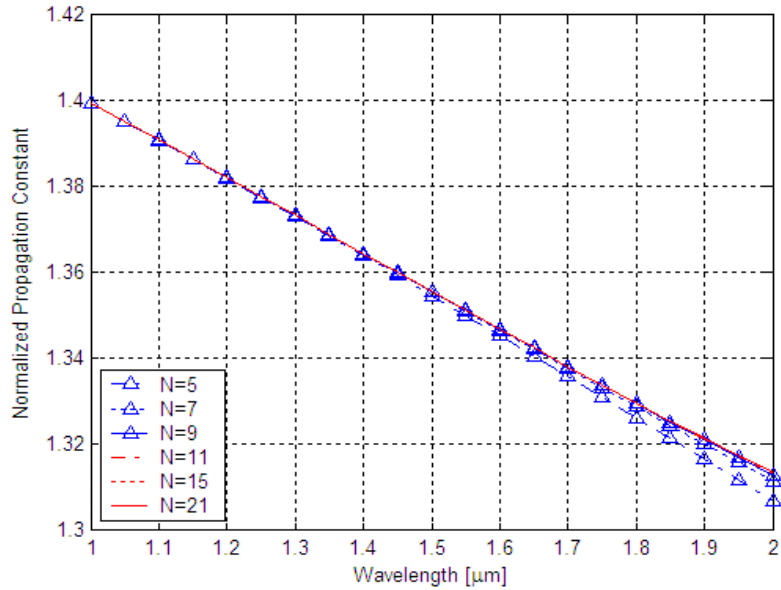
Figure 3.3 Normalized propagation constant versus wavelength of the mode for the second mode in waveguides with 4 to 20 layers. The geometry and parameters of the waveguide are the same as those in Figure 3.2.

Comparison of Figures 3.2 and 3.3 indicates that all the propagation characteristics curves for the fundamental mode are above the value 1.32, while all the characteristic curves for the second mode are located below this value in the wavelength range from 1.23 μm to 2.0 μm . Therefore, it may be said that the example photonic crystal waveguide under consideration here behaves as a single-mode waveguide in the wavelength range mentioned above. This wavelength range includes 1.3 μm and 1.55 μm , which are two widely utilized wavelengths in optical communications.

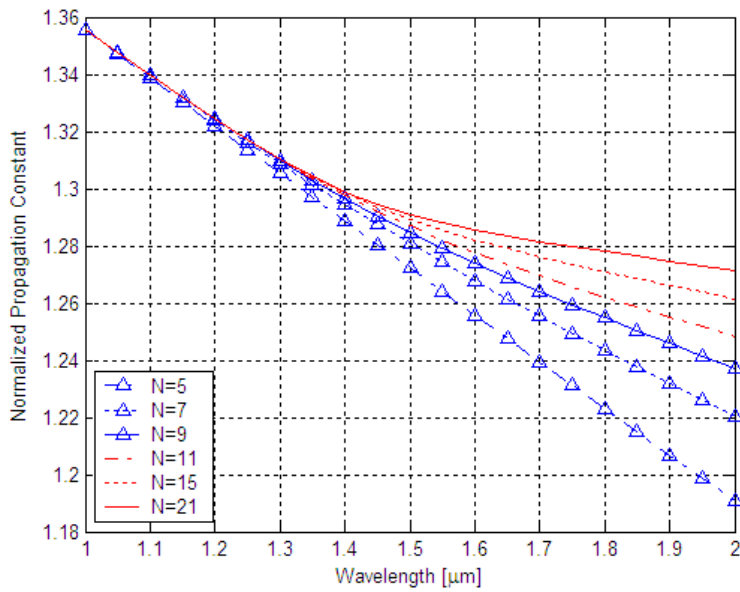
Next, we examine one-dimensional photonic crystal waveguides with a low-index core as in Figure 3.1 (b). The fields in the central core region of such waveguides is described by the modified Bessel function $I_n(k_1 r)$, whereas the corresponding fields in the high-index core

waveguides are expressed in terms of the Bessel function $J_n(k_1 r)$. Let us consider an example of this type of waveguides with parameters $r_1 = 0.1 \mu\text{m}$, $r_2 = 1.0 \mu\text{m}$, $d_a = 0.2 \mu\text{m}$, and $d_g = 0.3 \mu\text{m}$. Figures 3.4 (a) and (b) show the normalized propagation constants versus wavelength for the first mode and the second mode, respectively. It should be noted that the number of layers is odd instead of even because of structural nature of the waveguide. Comparison of Figures 3.4 (a) and 3.2 shows that the normalized propagation constant of the fundamental mode at $\lambda = 1.0 \mu\text{m}$ for the low-index core case is 0.01 below that for the high-index core waveguide. However, there is almost no difference between the characteristic curves of the second modes in both cases.

To examine the impact of the low-index core on propagation characteristics, r_1 is increased to $0.3 \mu\text{m}$, while keeping the rest of the parameters unchanged (i.e., the same as those in Figure 3.4). The normalized propagation constants for the first two modes in the waveguide with $r_1 = 0.3 \mu\text{m}$ are shown in Figures 3.5 (a) and (b). As seen from Figure 3.5 (a), the characteristic curves for the first mode are noticeably lowered, while those of the second mode have remained nearly unchanged. Therefore, it can be concluded that the fundamental mode is strongly affected by the core region, while the second mode is influenced negligibly.

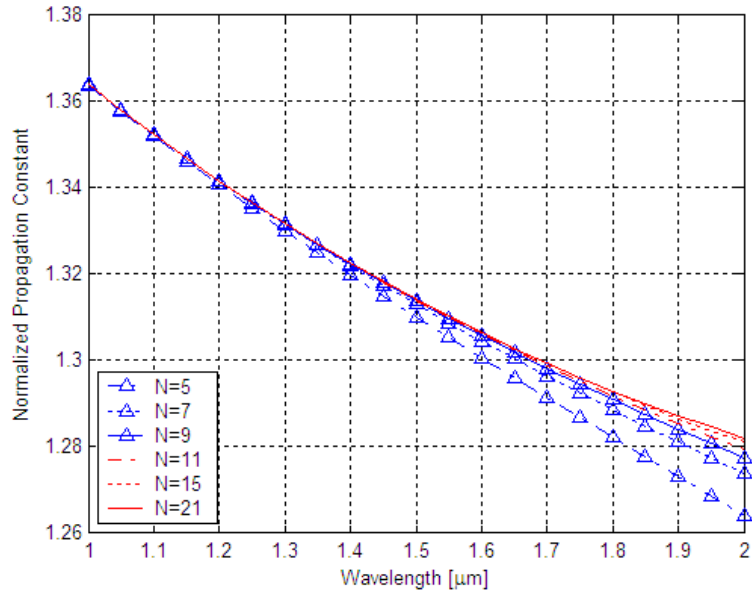


(a)

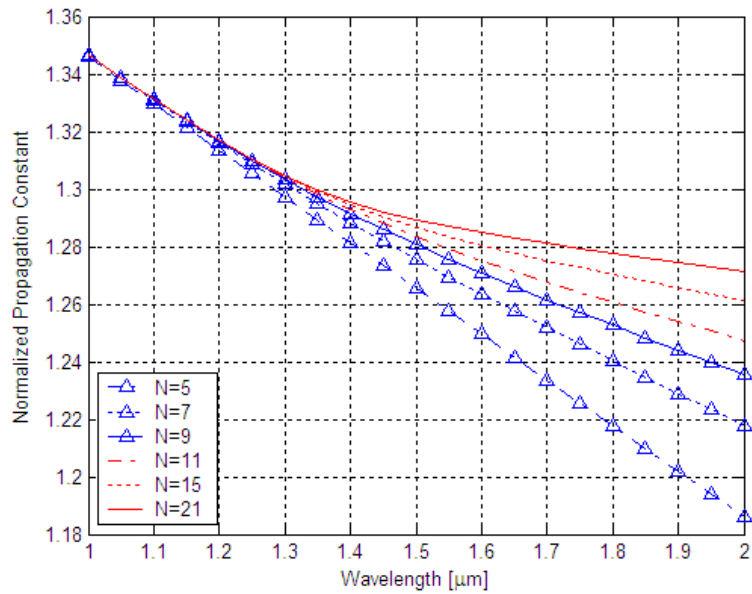


(b)

Figure 3.4 Normalized propagation constant ($\bar{\beta}$) versus wavelength (λ) for (a) the fundamental mode and (b) the second mode in a one-dimensional cylindrical photonic crystal waveguide with low-index core and parameters $r_1 = 0.1 \mu\text{m}$, $r_2 = 1.0 \mu\text{m}$, $d_a = 0.2 \mu\text{m}$, $d_g = 0.3 \mu\text{m}$.



(a)



(b)

Figure 3.5 Normalized propagation constant ($\bar{\beta}$) versus wavelength (λ) for (a) fundamental mode and (b) the second mode in a one-dimensional cylindrical photonic crystal waveguide with low-index core and parameters $r_1 = 0.3 \mu\text{m}$, $r_2 = 1.0 \mu\text{m}$, $d_a = 0.2 \mu\text{m}$, $d_g = 0.3 \mu\text{m}$.

Dispersion:

Differentiating the normalized propagation constant of the fundamental mode with respect to wavelength, the chromatic dispersion is calculated using the following relationship,

$$D = -\frac{\lambda}{c} \frac{d^2 \bar{\beta}}{d\lambda^2} \quad (3-19)$$

where c is the speed of light in free space. It is emphasized that with the wavelength dependence of the glass refractive index already built in the eigenvalue equation through the Sellmeier relationship, the dispersion expression in (3-19) accounts for both waveguide and material dispersion effects.

Figure 3.6 shows variations of dispersion versus wavelength for the photonic crystal waveguide of Figure 3.2. Similar to the propagation characteristics in Figure 3.2, the dispersion curves also tend to change very little when N becomes larger than 8. In other words, adding more layers to the cladding beyond a certain point will not affect the propagation constant, dispersion, and, in fact, all transmission properties of the waveguide. It is also worth noting that in the 1.55- μm window the dispersion is small. To be more specific, the dispersion for $N = 8$ is -3.8248 ps/nm·km. Having a small dispersion around this wavelength is highly desirable in long-haul fiber-optic communication systems, because the minimum attenuation of glass also occurs at the same wavelength.

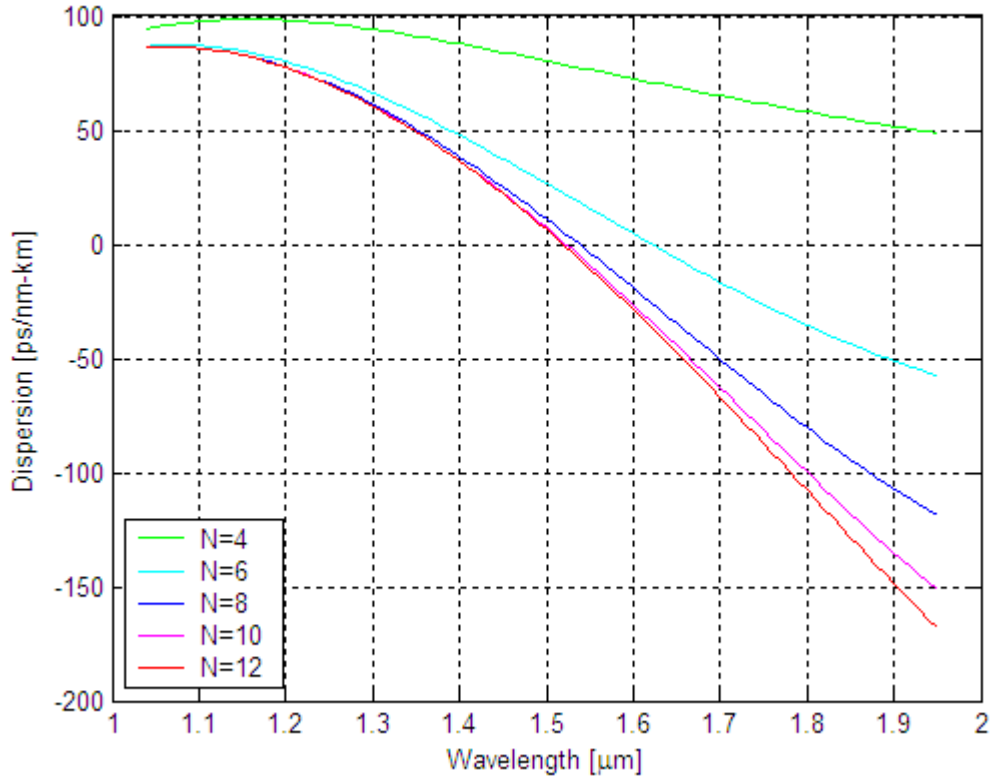


Figure 3.6 Variations of chromatic dispersion versus wavelength for the photonic crystal waveguide of Figure 3.2

3.4.2 Field Distributions

Figure 3.7 shows representative field profiles for the fundamental mode of the example photonic crystal waveguide with $N=10$ layers at $\lambda = 1.55 \mu\text{m}$. The parameters of the waveguide are the same as those in Figure 3.2. As noted, the transverse components, E_r and E_ϕ , have their maxima on the waveguide axis ($r=0$), thus the power flow density is largest in the central core region. This should be expected from a high-index core photonic crystal waveguide. Figure 3.8 illustrates field profiles for the E_ϕ component of the same waveguide but with the different number of layers. Again, the field distributions remain essentially unchanged for N larger than a certain value, say $N=8$ in this example.

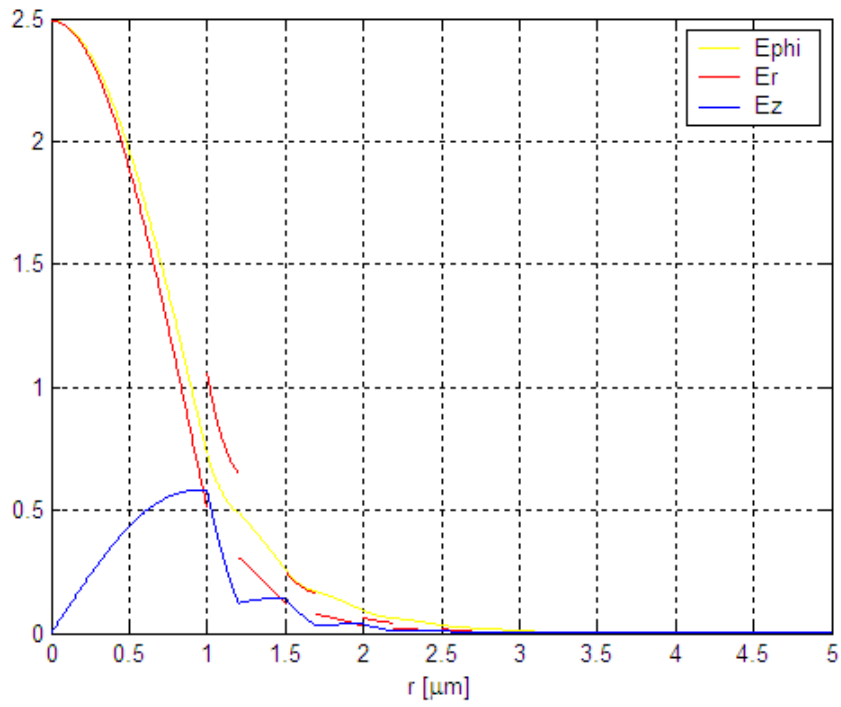


Figure 3.7 Plots of electric field components E_r , E_{ϕ} , and E_z versus radial coordinate r at $\lambda = 1.55 \mu\text{m}$ for the fundamental mode of a photonic crystal waveguide with $N=10$ and parameters the same as those in Figure 3.2

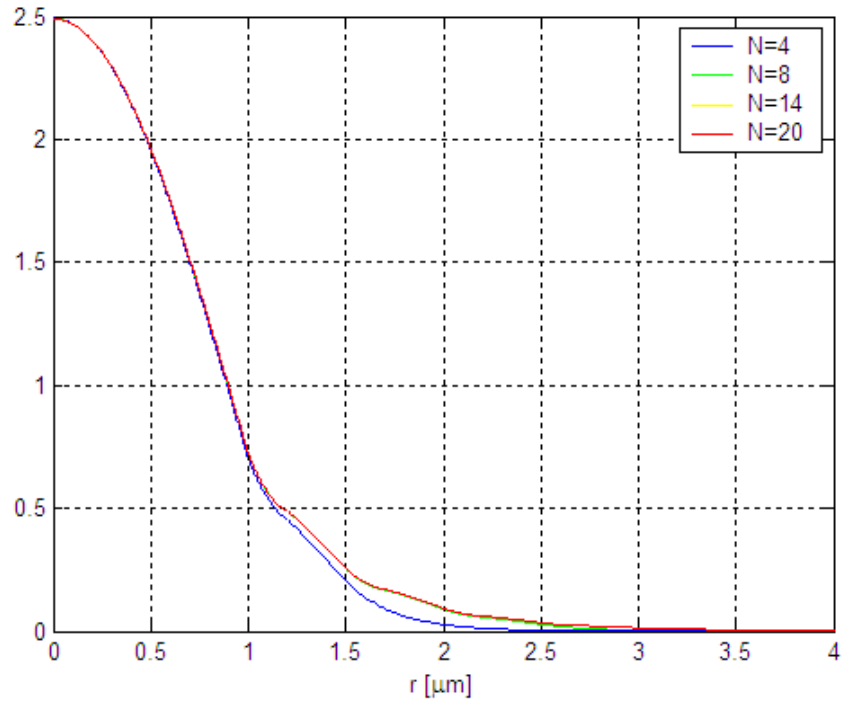
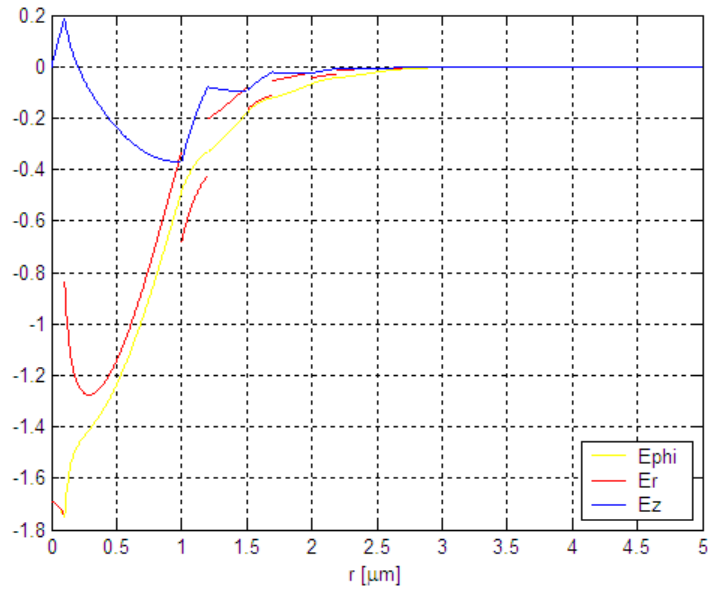
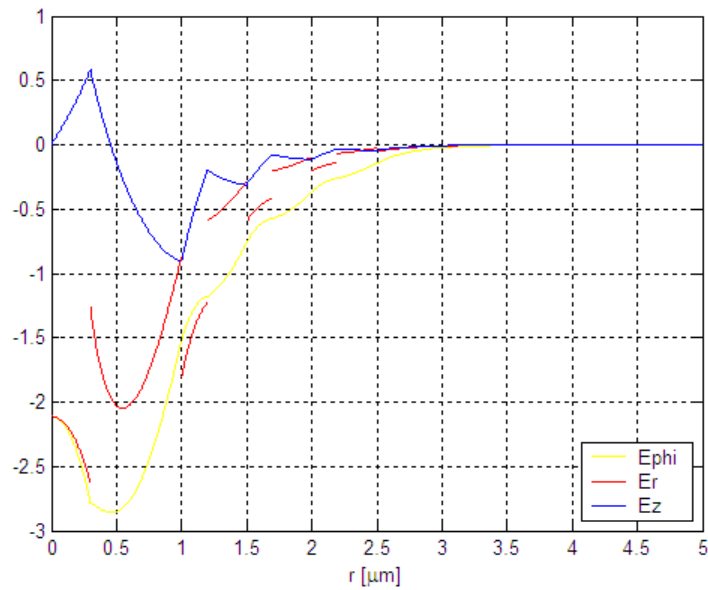


Figure 3.8 Plots of the electric field component E_ϕ versus radial coordinate at $\lambda = 1.55 \mu\text{m}$ for the fundamental mode of the high-index core photonic crystal waveguide. Waveguide parameters are the same as those in Figure 3.2.

For the low-index core photonic crystal waveguides, we expect dips at the center. Figures 3.9 (a) and (b) show field profiles for the fundamental mode of the waveguides in Figure 3.4 (a) ($r_1 = 0.1 \mu\text{m}$) and Figure 3.5 (a) ($r_1 = 0.3 \mu\text{m}$), respectively. For both waveguides, $N=9$ and the wavelength of operation is at $\lambda = 1.55 \mu\text{m}$. For larger r_1 , the dip at the center becomes more pronounced.



(a)



(b)

Figure 3.9 Plots of electric field components E_r , E_{ϕ} , and E_z versus radial coordinate at $\lambda = 1.55$ μm for the fundamental mode of a low-index core photonic crystal waveguide with $N=9$ and parameters the same as those in (a) Figure 3.4 (a), and (b) Figure 3.5 (a)

3.4.3 Effective Area

Apart from a linear term (n_L), the refractive index of glass has a nonlinear term (n_{NL}) due to the weak dependence of the dielectric constant of silica on guided light intensity. Since the nonlinearity is proportional to the light intensity, it can be described as

$$n_{NL} = \frac{n_2 P}{A_{eff}} \quad (3-20)$$

where n_2 is a material property of glass, P is the power of optical signal propagating in the fiber, and A_{eff} is the effective area [58]. In order to achieve low nonlinearity, as in long-haul and high capacity optical fiber links, the fiber should have as large an effective area as possible. On the other hand, in order to achieve high nonlinearity, for example in switching applications, the effective area of the fiber should be as small as possible. Photonic crystal and holey fibers can be designed to achieve either extreme of effective areas. Holey fibers with effective areas as small as $2.8 \mu\text{m}^2$ have been reported [60].

The effective area can be calculated from the electric field vector using the following relation,

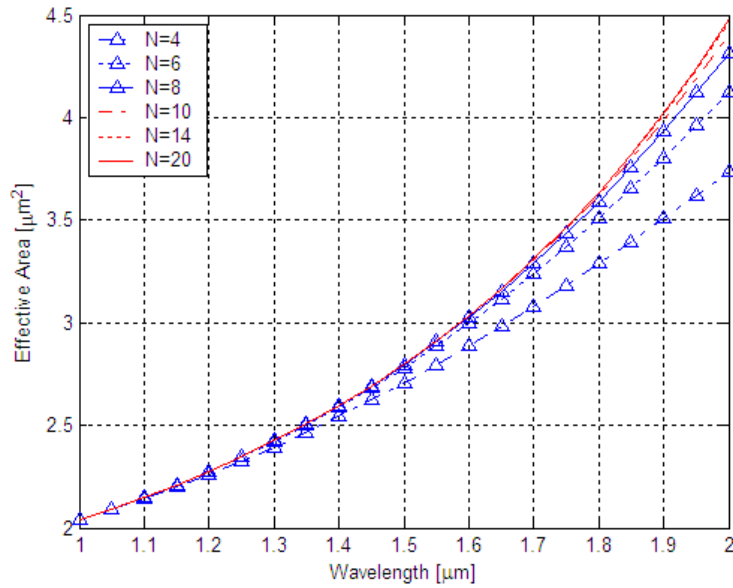
$$A_{eff} = \frac{\left(\int_0^{2\pi} \int_0^\infty |\mathbf{E}(r, \varphi)|^2 r dr d\varphi \right)^2}{\int_0^{2\pi} \int_0^\infty |\mathbf{E}(r, \varphi)|^4 r dr d\varphi} = 4\pi \frac{Num}{Den} \quad (3-21)$$

where

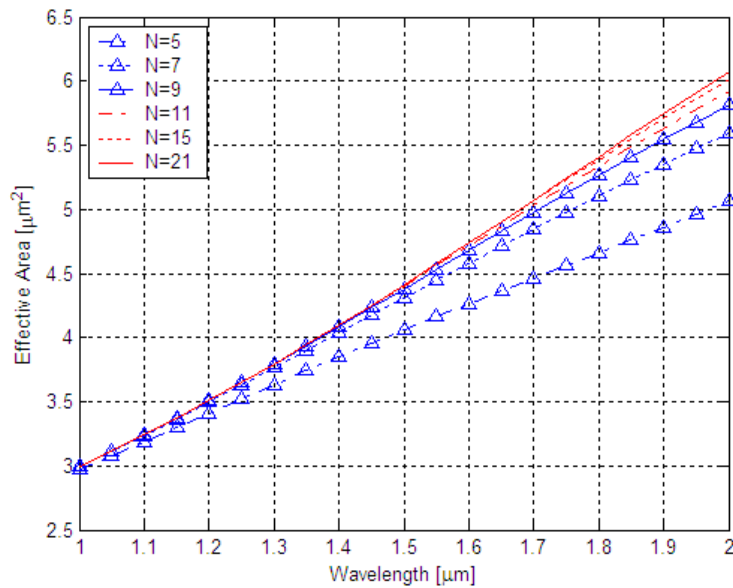
$$\begin{aligned} Num &= \left[\int_0^\infty \left\{ |E_r(r)|^2 + |E_\varphi(r)|^2 + |E_z(r)|^2 \right\} r dr \right]^2 \\ Den &= \int_0^\infty \left\{ 3 \left[\left(|E_r(r)|^2 + |E_z(r)|^2 \right)^2 + |E_\varphi(r)|^4 \right] + 2 |E_\varphi(r)|^2 \left[|E_r(r)|^2 + |E_z(r)|^2 \right] \right\} r dr \end{aligned} \quad (3-22)$$

Based on Eq. (3.20), effective areas for the 1D high-index core PCF when $r_1 = 1.0 \mu\text{m}$, $d_a = 0.2 \mu\text{m}$, and $d_g = 0.3 \mu\text{m}$ and the 1D low-index core PCF when $r_1 = 0.3 \mu\text{m}$, $r_2 = 1.0 \mu\text{m}$, $d_a = 0.2 \mu\text{m}$, and $d_g = 0.3 \mu\text{m}$ are evaluated by changing the total number of layers. Figure 3.10 (a) shows effective areas for the 1D high-index core PCF and Figure 3.10 (b) shows effective areas for the 1D low-index core PCF. As noticed, generally when the operating wavelength is longer, effective area tends to be larger. This is as expected because the electromagnetic fields spread further with longer wavelengths. Another interesting feature is that effective areas for the 1D high-index core PCF are smaller than those for the 1D low-index core PCF. This can be understood from the fact that the fields for 1D high-index core PCF as shown in Figure 3.8 are more tightly confined to its central core region than those for 1D low-index core PCF as shown in Figure 3.9. And it is also noticed that as the number of layers is increasing, the effective area is getting larger. But since there is enough number of layers, the effective areas remain about the same regardless of increasing any more.

Compared with effective areas of $50 - 100 \mu\text{m}^2$ that conventional optical fibers or dispersion-shifted fibers have, 1D PCFs here have much smaller effective areas ranging from $2.45 \mu\text{m}^2$ for the 1D high-index core PCF at $1.3\text{-}\mu\text{m}$ wavelength to $5.25 \mu\text{m}^2$ for the 1D low-index core PCF at $1.55\text{-}\mu\text{m}$ wavelength. Better nonlinearity with this smaller effective area may make it easier to invent devices using nonlinear optical fiber effects such as the generation of self-phase modulation (SPM), four-wave mixing, Raman scattering, and soliton generation.



(a)



(b)

Figure 3.10 Effective area versus wavelength for the fundamental mode of 1D cylindrical photonic crystal waveguide with (a) high-index core and parameters, $r_1 = 1.0 \mu\text{m}$, $d_a = 0.2 \mu\text{m}$, and $d_g = 0.3 \mu\text{m}$ and (b) low-index core and parameters, $r_1 = 0.3 \mu\text{m}$, $r_2 = 1.0 \mu\text{m}$, $d_a = 0.2 \mu\text{m}$, and $d_g = 0.3 \mu\text{m}$ with respect to the total number of layers

Chapter 4

Analysis of Two-Dimensional Photonic Crystal and Holey Fibers

4.1 Introduction

Two-dimensional photonic crystal fibers, often referred to as holey fibers, have complicated structures and thus cannot be analyzed easily using analytical techniques. A variety of numerical methods have been developed for the electromagnetic analysis of structures with complicated geometries. Among these methods the finite-difference time-domain method (FDTD) has gained considerable popularity in recent years, because this method provides robust solutions for Maxwell's equations and can readily accommodate complex-valued material properties. Using the FDTD method, the continuous electromagnetic field in a finite volume of space is sampled at distinct points in a space lattice and at equally spaced sampling points in time. The sampled points are used for numerical calculations of allowed modes in a given waveguide.

Based on a FDTD algorithm, a computer code is developed to analyze the propagation characteristics of holey fibers. The FDTD formulation of Maxwell's equations is presented in section 4.2. Despite being an effective technique for calculation of propagation constants of guided modes, the FDTD method is not well suited for the evaluation of individual mode field distributions. This is because the source is an impulse function in the time domain covering an infinite spectrum, thus field solutions are superposition of all possible modes. To alleviate this problem, individual mode field solutions are obtained using the finite difference method (FDM), which, with propagation constants available from FDTD, can quickly and conveniently provide

individual mode field solutions. A brief discussion of FDM is presented in section 4.3. In section 4.4, test and comparison of FDTD and FDM techniques are addressed. Numerical results for example cases of holey fibers are presented in section 4.5.

4.2 Finite-Difference Time-Domain (FDTD) Formulation of Maxwell's Equations

The FDTD method was first introduced by Yee in 1966 [61]. Yee visualized the positions of the electric and magnetic field components in a unit cell of the FDTD lattice in Cartesian coordinates as shown in Figure 4.1. It is noted that each electric field component is surrounded by four circulating magnetic field components and vice versa. The adjacent field components are needed to generate another field component as time is marching. An arbitrary material object can be approximated by building up unit cells for which field component positions are disposed with the desired values of permittivity and permeability. Also, the arbitrary object may consist of different kinds of materials. Once the geometry of the object is specified in the calculation region, source condition is modeled somewhere in the region. Initially, it is assumed that all fields within the numerical simulation region are identically zero. Then, an incident wave is enforced to enter the simulation region.

Let us first consider a region of space which is source-free and lossless [62]. Using the MKS system of units, Maxwell's curl equations are expressed as

$$\nabla \times \mathbf{E} = -\mu \frac{d\mathbf{H}}{dt} \quad (4-1)$$

$$\nabla \times \mathbf{H} = \epsilon \frac{d\mathbf{E}}{dt} \quad (4-2)$$

where ϵ is the electrical permittivity constant in farads/meter and μ is the magnetic permeability constant in henrys/meter. Assuming that ϵ and μ are scalar quantities (that is, the medium is assumed to be isotropic), expanding the curl expressions in (4-1) and (4-2), and equating the like components yields the following system of equations,

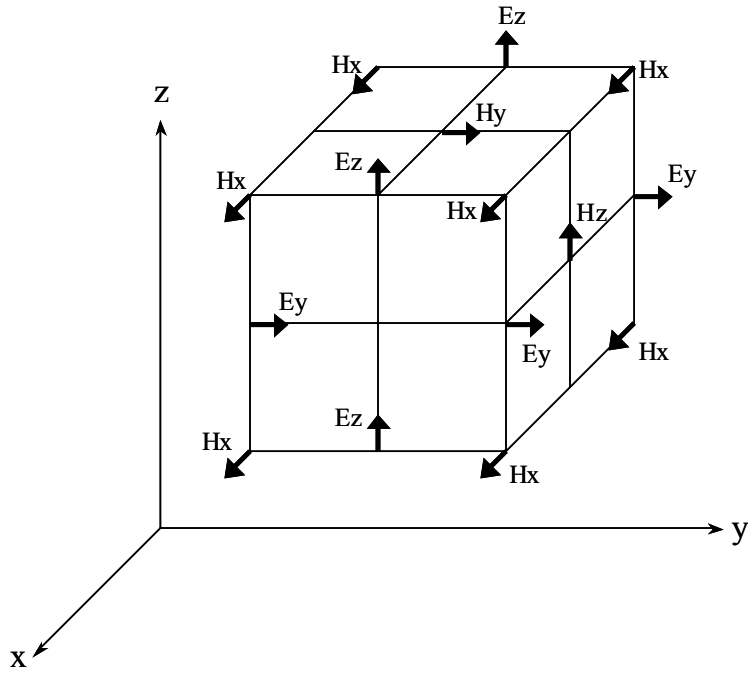


Figure 4.1 A unit cell of the FDTD lattice in Cartesian coordinates

$$\frac{\partial E_z}{\partial y} - \frac{\partial E_y}{\partial z} = -\mu \frac{\partial H_x}{\partial t} \quad (4-3a)$$

$$\frac{\partial E_x}{\partial z} - \frac{\partial E_z}{\partial x} = -\mu \frac{\partial H_y}{\partial t} \quad (4-3b)$$

$$\frac{\partial E_y}{\partial x} - \frac{\partial E_x}{\partial y} = -\mu \frac{\partial H_z}{\partial t} \quad (4-3c)$$

$$\frac{\partial H_z}{\partial y} - \frac{\partial H_y}{\partial z} = \epsilon \frac{\partial E_x}{\partial t} \quad (4-4a)$$

$$\frac{\partial H_x}{\partial z} - \frac{\partial H_z}{\partial x} = \epsilon \frac{\partial E_y}{\partial t} \quad (4-4b)$$

$$\frac{\partial H_y}{\partial x} - \frac{\partial H_x}{\partial y} = \epsilon \frac{\partial E_z}{\partial t} \quad (4-4c)$$

The system of six coupled partial differential equations in (4-3) and (4-4) forms the basis for the FDTD analysis of electromagnetic wave interactions with general three-dimensional objects. It should be noted that the electric and magnetic field components (E_x , E_y , E_z , H_x , H_y , and H_z) are inter-related. Since these equations are functions of space and time, they can be discretized in the space and time domains and used to find field solutions numerically. Referring to Figure 4.1, we denote a grid point in the rectangular lattice as

$$(i, j, k) = (i\Delta x, j\Delta y, k\Delta z) \quad (4-5a)$$

and any function of space and time as

$$F^n(i, j, k) = F(i\Delta x, j\Delta y, k\Delta z, n\Delta t) \quad (4-5b)$$

where Δx , Δy , and Δz are, respectively, the lattice space increments in the x, y, and z coordinate directions and Δt is the time increment, while i, j, k, and n are integers [63]. Using central finite difference approximation for space and time derivatives that are accurate to second order, the partial derivatives are expressed as

$$\frac{\partial F^n(i, j, k)}{\partial x} = \frac{F^n(i + \frac{1}{2}, j, k) - F^n(i - \frac{1}{2}, j, k)}{\Delta x} + O(\Delta x^2) \quad (4-6a)$$

$$\frac{\partial F^n(i, j, k)}{\partial t} = \frac{F^{n+1/2}(i, j, k) - F^{n-1/2}(i, j, k)}{\Delta t} + O(\Delta t^2) \quad (4-6b)$$

Applying (4-6) to the space and time derivatives in (4-3a), (4-3b), and (4-4c), we obtain the following FDTD approximation as representative relations in a three-dimensional FDTD formulation

$$H_x^{n+1/2}(i, j + \frac{1}{2}, k + \frac{1}{2}) = H_x^{n-1/2}(i, j + \frac{1}{2}, k + \frac{1}{2}) + \frac{\Delta t}{\mu} \left\{ \left[\frac{E_y^n(i, j + \frac{1}{2}, k + 1) - E_y^n(i, j + \frac{1}{2}, k)}{\Delta z} \right] - \left[\frac{E_z^n(i, j + 1, k + \frac{1}{2}) - E_z^n(i, j, k + \frac{1}{2})}{\Delta y} \right] \right\} \quad (4-7a)$$

$$\begin{aligned}
 H_y^{n+\frac{1}{2}}(i+\frac{1}{2}, j, k+\frac{1}{2}) &= H_y^{n-\frac{1}{2}}(i+\frac{1}{2}, j, k+\frac{1}{2}) \\
 &+ \frac{\Delta t}{\mu} \left\{ \left[\frac{E_z^n(i+1, j, k+\frac{1}{2}) - E_z^n(i, j, k+\frac{1}{2})}{\Delta x} \right] - \left[\frac{E_x^n(i+\frac{1}{2}, j, k+1) - E_x^n(i+\frac{1}{2}, j, k)}{\Delta z} \right] \right\}
 \end{aligned} \tag{4-7b}$$

$$\begin{aligned}
 E_z^{n+1}(i, j, k+\frac{1}{2}) &= E_z^n(i, j, k+\frac{1}{2}) + \frac{\Delta t}{\epsilon_0 \epsilon_r(i, j, k+\frac{1}{2})} \left\{ \left[\frac{H_y^{n+\frac{1}{2}}(i+\frac{1}{2}, j, k+\frac{1}{2}) - H_y^{n+\frac{1}{2}}(i-\frac{1}{2}, j, k+\frac{1}{2})}{\Delta x} \right] \right. \\
 &\quad \left. - \left[\frac{H_x^{n+\frac{1}{2}}(i, j+\frac{1}{2}, k+\frac{1}{2}) - H_x^{n+\frac{1}{2}}(i, j-\frac{1}{2}, k+\frac{1}{2})}{\Delta y} \right] \right\}
 \end{aligned} \tag{4-7c}$$

It is understood from (4-7a) that H_x is located at $(i, j+\frac{1}{2}, k+\frac{1}{2})$, the H and E components are interleaved within the unit cell, and that the new value of a field vector component (H_x) at any lattice point depends only on its previous value and the previous values of the components of the other field vector at adjacent points. Then, the next computation of the field vector is continued as time is marching by a given time step.

It is generally assumed that fibers have no variations along the direction of propagation, and variations of material properties (such as refractive index) are limited to the transverse directions. Holey fibers that will be analyzed here are assumed to have geometries such that the refractive index is uniform along the z-axis. A schematic of a cross section of an example holey fiber is illustrated in Figure 4.2. Thus, instead of using a full-wave analysis based on (4-3) and (4-4) to numerically model the waveguide structures, we can take advantage of properties of the propagating modes to simplify the formulation. The components of electric and magnetic fields in waveguides with no variations along the direction of propagation (z-axis) can be expressed as

$$F(x, y, z) = F(x, y)e^{-j\beta z} \tag{4-8}$$

where β is the axial propagation constant. Using (4-8) and employing the notations of space and time in FDTD, the adjacent electric and magnetic fields in the axial propagation direction are related as

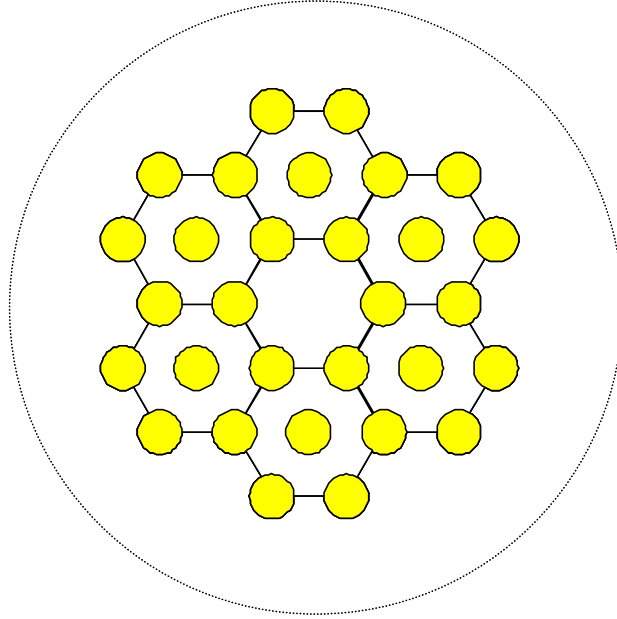


Figure 4.2 Schematic of a cross section of an example holey fiber

$$E^n(i, j, k \pm 1) = E^n(i, j, k)e^{\mp j\beta\Delta z} \quad (4-9a)$$

$$H^n(i, j, k \pm 1) = H^n(i, j, k)e^{\mp j\beta\Delta z} \quad (4-9b)$$

Now, the electric and magnetic fields become complex quantities based on phasor notations. The first-order partial derivatives with respect to z in the discretized space domain require two adjacent fields. The two adjacent fields can be represented by a field at the mid point between them. Furthermore, the first-order partial derivatives with respect to z in (4-3) and (4-4) are replaced with $-j\beta$, because the z -dependence of fields is as $\exp(-j\beta z)$. Based on these two facts, the following expressions are obtained [64],

$$\left\{ \frac{E^n(i, j, k+1) - E^n(i, j, k)}{\Delta z} \right\} = -j\beta E^n(i, j, k + \frac{1}{2}) \quad (4-10a)$$

$$= -j\beta E^n(i, j, k) e^{-j\beta \frac{\Delta z}{2}}$$

$$\left\{ \frac{H^n(i, j, k+1) - H^n(i, j, k)}{\Delta z} \right\} = -j\beta H^n(i, j, k + \frac{1}{2}) \quad (4-10b)$$

$$= -j\beta H^n(i, j, k) e^{-j\beta \frac{\Delta z}{2}}$$

Substituting the electric and magnetic field components from (4-10) into (4-7), the following two-dimensional FDTD expressions are obtained,

$$H_x^{n+\frac{1}{2}}(i, j + \frac{1}{2}) = H_x^{n-\frac{1}{2}}(i, j + \frac{1}{2}) + \frac{\Delta t}{\mu} \left\{ -j\beta \cdot E_y^n(i, j + \frac{1}{2}) - \left[\frac{E_z^n(i, j+1) - E_z^n(i, j)}{\Delta y} \right] \right\} \quad (4-11a)$$

$$H_y^{n+\frac{1}{2}}(i + \frac{1}{2}, j) = H_y^{n-\frac{1}{2}}(i + \frac{1}{2}, j) + \frac{\Delta t}{\mu} \left\{ \left[\frac{E_z^n(i+1, j) - E_z^n(i, j)}{\Delta x} \right] + j\beta \cdot E_x^n(i + \frac{1}{2}, j) \right\} \quad (4-11b)$$

$$E_z^{n+1}(i, j) = E_z^n(i, j) + \frac{\Delta t}{\epsilon_0 \epsilon_r(i, j)} \left\{ \left[\frac{H_y^{n+\frac{1}{2}}(i + \frac{1}{2}, j) - H_y^{n+\frac{1}{2}}(i - \frac{1}{2}, j)}{\Delta x} \right] - \left[\frac{H_x^{n+\frac{1}{2}}(i, j + \frac{1}{2}) - H_x^{n+\frac{1}{2}}(i, j - \frac{1}{2})}{\Delta y} \right] \right\} \quad (4-11c)$$

Note that every term in the longitudinal direction is canceled out in (4-11). For example, $k + \frac{1}{2}$ is no longer required in (4-11a), because there are no variations along the z-direction during the time marching. Hence, the basic equations for FDTD algorithm are set up in the two-dimensional space. Comparing the full-wave analysis based on (4-7) that requires complete modeling coverage along the longitudinal direction for at least several wavelengths with the compact two-dimensional FDTD algorithm, significant reduction in the required computer memory allocation and running time can be achieved. Thus, for simulation of arbitrary waveguides that are uniform along the direction of wave propagation, only modeling of the cross sections of waveguides is sufficient.

4.2.1 Perfectly Matched Layer (PML)

When an arbitrary electromagnetic object is analyzed numerically using FDTD, regions extending to infinity need to be modeled carefully. For example, in antenna analysis using FDTD, the antenna is surrounded by an infinite medium (usually air). Modeling infinite media, whether

they are modeled in one-, two-, or three-dimensional space, is practically impossible because of computer memory limitation even with the advanced current technology. This fact spells out the need for a special method to simulate regions extending to infinity. One way to model an infinite medium is to introduce an absorbing boundary condition (ABC) at the outer lattice boundary. Somehow, the outer boundary should be matched to an absorbing material medium. This is analogous to the physical treatment of the walls of an anechoic chamber. Ideally, the absorbing medium is only as thick as a few lattice cells, reflectionless to all impinging waves over their full frequency spectrum, highly absorbing, and effective in the near field of a source or a scatterer.

In 1994, Berenger introduced a highly effective ABC, which is designated as perfectly matched layer (PML) [65]. The innovation of Berenger's PML is that plane waves of arbitrary incidence, polarization, and frequency are matched at the boundary. For this, Berenger derived a novel split-field formulation of Maxwell's equations where each vector field component is split into two orthogonal components. Each of the 12 resulting components is then expressed as satisfying a coupled set of first-order partial differential equations. By choosing loss parameters consistent with a dispersionless medium, a perfectly matched planar interface is established.

In a continuous space, the PML absorber and the host medium are perfectly matched. However, in the discrete FDTD lattice, the electric and magnetic material parameters are represented in a piecewise-constant manner and are spatially staggered. This can result in discretization errors. Berenger proposed spatial scaling of the PML parameters to reduce the discretization errors at material interfaces. He also proposed means to reduce the discretization errors for the second-order FDTD scheme and to reduce the required PML thickness.

In order to show how to accommodate the PML, let us consider the E_z component. After transforming (4-4c) into the Fourier (phasor) domain, we have

$$j\omega \cdot \left(1 + \frac{\sigma_D(x)}{j\omega\epsilon_0}\right) \left(1 + \frac{\sigma_D(y)}{j\omega\epsilon_0}\right) E_z = \frac{1}{\epsilon_0\epsilon_r} \left\{ \frac{\partial H_y}{\partial x} - \frac{\partial H_x}{\partial y} \right\} \quad (4-12)$$

where σ_D is the loss factor that increases gradually as it goes into the PML to cause E_z to be attenuated. Then, the left-hand-side (LHS) of (4-12) in the FDTD form becomes,

$$\begin{aligned}
 LHS &= \frac{\partial E_z}{\partial t} + \frac{\sigma_D(i)}{\varepsilon_0} E_z + \frac{\sigma_D(j)}{\varepsilon_0} E_z + \frac{\sigma_D(i)\sigma_D(j)}{\varepsilon_0^2} \frac{1}{j\omega} E_z \\
 &\approx \frac{E_z^{n+\frac{1}{2}}(i, j) - E_z^{n-\frac{1}{2}}(i, j)}{\Delta t} + \frac{\sigma_D(i)}{\varepsilon_0} \left[\frac{E_z^{n+\frac{1}{2}}(i, j) + E_z^{n-\frac{1}{2}}(i, j)}{2} \right] + \frac{\sigma_D(j)}{\varepsilon_0} \left[\frac{E_z^{n+\frac{1}{2}}(i, j) + E_z^{n-\frac{1}{2}}(i, j)}{2} \right] \\
 &= E_z^{n+\frac{1}{2}}(i, j) \frac{1}{\Delta t} \left[1 + \frac{\sigma_D(i)\Delta t}{2\varepsilon_0} + \frac{\sigma_D(j)\Delta t}{2\varepsilon_0} \right] - E_z^{n-\frac{1}{2}}(i, j) \frac{1}{\Delta t} \left[1 - \frac{\sigma_D(i)\Delta t}{2\varepsilon_0} - \frac{\sigma_D(j)\Delta t}{2\varepsilon_0} \right]
 \end{aligned} \tag{4-13a}$$

There is an approximation by omitting $\frac{\sigma_D(i)\sigma_D(j)}{\varepsilon_0^2} \frac{1}{j\omega} E_z$, because it is attenuated by twice multiplication of the loss coefficient. On the other hand, referring to (4-11c), the right-hand-side (RHS) of (4-12) in the FDTD form becomes,

$$RHS = \frac{\Delta t}{\varepsilon_0 \varepsilon_r(i, j) \Delta x} \left\{ H_y^n(i + \frac{1}{2}, j) - H_y^n(i - \frac{1}{2}, j) - H_x^n(i, j + \frac{1}{2}) + H_x^n(i, j - \frac{1}{2}) \right\} \tag{4-13b}$$

Putting the LHS and RHS together, the following FDTD equation for the compact two-dimensional algorithm with the PML incorporated is obtained,

$$\begin{aligned}
 E_z^{n+\frac{1}{2}}(i, j) &= \frac{1 - \frac{\sigma_D(i)\Delta t}{2\varepsilon_0} - \frac{\sigma_D(j)\Delta t}{2\varepsilon_0}}{1 + \frac{\sigma_D(i)\Delta t}{2\varepsilon_0} + \frac{\sigma_D(j)\Delta t}{2\varepsilon_0}} \cdot E_z^{n-\frac{1}{2}}(i, j) + \frac{1}{1 + \frac{\sigma_D(i)\Delta t}{2\varepsilon_0} + \frac{\sigma_D(j)\Delta t}{2\varepsilon_0}} \cdot \frac{\Delta t}{\varepsilon_0 \varepsilon_r(i, j) \Delta x} \\
 &\quad \left\{ H_y^n(i + \frac{1}{2}, j) - H_y^n(i - \frac{1}{2}, j) - H_x^n(i, j + \frac{1}{2}) + H_x^n(i, j - \frac{1}{2}) \right\} \\
 &= gi3(i)gj3(j) \cdot E_z^{n-\frac{1}{2}}(i, j) + gi2(i)gj2(j) \cdot \frac{\Delta t}{\varepsilon_0 \varepsilon_r(i, j) \Delta x} \\
 &\quad \left\{ H_y^n(i + \frac{1}{2}, j) - H_y^n(i - \frac{1}{2}, j) - H_x^n(i, j + \frac{1}{2}) + H_x^n(i, j - \frac{1}{2}) \right\}
 \end{aligned} \tag{4-14}$$

where gi2 and gi3 (analogous to gj2 and gj3, respectively) are given by [66]

$$\begin{aligned}
 gi2(i) &= \frac{1}{1 + \sigma_D(i)\Delta t/2\epsilon_0} \\
 gi3(i) &= \frac{1 - \sigma_D(i)\Delta t/2\epsilon_0}{1 + \sigma_D(i)\Delta t/2\epsilon_0}
 \end{aligned} \tag{4-15}$$

By a similar treatment, (4-3b) can be transformed to

$$j\omega \cdot \left(1 + \frac{\sigma_D(x)}{j\omega\epsilon_0}\right) H_y = \left(1 + \frac{\sigma_D(y)}{j\omega\epsilon_0}\right) \cdot \frac{1}{\mu_0} \left\{ \frac{\partial E_z}{\partial x} - \frac{\partial E_x}{\partial z} \right\} \tag{4-16}$$

Then, the LHS of (4-16) is rewritten as

$$\begin{aligned}
 LHS &= j\omega H_y + \frac{\sigma_D(x)}{\epsilon_0} H_y \\
 &= \frac{H_y^{n+1}(i + \frac{1}{2}, j) - H_y^n(i + \frac{1}{2}, j)}{\Delta t} + \frac{\sigma_D(x)}{\epsilon_0} \frac{H_y^{n+1}(i + \frac{1}{2}, j) + H_y^n(i + \frac{1}{2}, j)}{2} \\
 &= H_y^{n+1}(i + \frac{1}{2}, j) \frac{1}{\Delta t} \left[1 + \frac{\sigma_D(i + \frac{1}{2})\Delta t}{2\epsilon_0}\right] - H_y^n(i + \frac{1}{2}, j) \frac{1}{\Delta t} \left[1 - \frac{\sigma_D(i + \frac{1}{2})\Delta t}{2\epsilon_0}\right]
 \end{aligned} \tag{4-17}$$

And the RHS becomes,

$$\begin{aligned}
 RHS &= \frac{1}{\mu_0} \left[\frac{\partial E_z}{\partial x} + \frac{\sigma_D(y)}{j\omega\epsilon_0} \frac{\partial E_z}{\partial x} \right] - \frac{1}{\mu_0} \left(1 + \frac{\sigma_D(y)}{j\omega\epsilon_0}\right) \frac{\partial E_x}{\partial z} \\
 &\approx \frac{1}{\mu_0} \left[\frac{curl_e}{\Delta x} + \frac{\sigma_D(j)}{\epsilon_0} \Delta t \sum_{n=0}^T \frac{curl_e}{\Delta x} \right] + \frac{1}{\mu_0} j\beta \cdot E_x^n(i + \frac{1}{2}, j)
 \end{aligned} \tag{4-18}$$

where $curl_e = [E_z^n(i+1, j) - E_z^n(i, j)]$. It is noted that $(1/j\omega)$ is regarded as an integration operation over time. Since there is no need of PML in the direction of wave propagation, PML term in the z direction is ignored.

Putting together the LHS and RHS expressions, another FDTD equation with the PML incorporated for the compact two-dimensional algorithm is obtained,

$$\begin{aligned}
 H_y^{n+1}(i+\frac{1}{2}, j) &= \frac{\left[1 - \frac{\sigma_D(i+\frac{1}{2})\Delta t}{2\varepsilon_0}\right]}{\left[1 + \frac{\sigma_D(i+\frac{1}{2})\Delta t}{2\varepsilon_0}\right]} H_y^n(i+\frac{1}{2}, j) \\
 &+ \frac{1}{\left[1 + \frac{\sigma_D(i+\frac{1}{2})\Delta t}{2\varepsilon_0}\right]} \frac{\Delta t}{\mu_0 \Delta x} \left\{ \left[\text{curl}_- e + \frac{\sigma_D(j)}{\varepsilon_0} \Delta t \sum_{n=0}^T \text{curl}_- e \right] + j\beta \cdot \Delta x \cdot E_x^n(i+\frac{1}{2}, j) \right\} \\
 &= \text{fi3}(i+\frac{1}{2}) \cdot H_y^n(i+\frac{1}{2}, j) + \text{fi2}(i+\frac{1}{2}) \cdot \frac{\Delta t}{\mu_0 \Delta x} \cdot \text{curl}_- e + \text{fi2}(i+\frac{1}{2}) \text{fi1}(j) \cdot I_{H_y}^{n+\frac{1}{2}}(i+\frac{1}{2}, j) \\
 &+ \text{fi2}(i+\frac{1}{2}) \cdot \frac{\Delta t}{\mu_0 \Delta x} \cdot j\beta \cdot \Delta x \cdot E_x^n(i+\frac{1}{2}, j)
 \end{aligned} \tag{4-19}$$

where fj1, fi2, and fi3 are given by

$$\begin{aligned}
 \text{fi1}(j) &= \frac{\Delta t}{\mu_0 \Delta x} \cdot 2 \cdot \frac{\sigma_D(j)}{2\varepsilon_0} \Delta t \\
 \text{fi2}(i+\frac{1}{2}) &= \frac{1}{1 + \sigma_D(i+\frac{1}{2})\Delta t/2\varepsilon_0} \\
 \text{fi3}(i+\frac{1}{2}) &= \frac{1 - \sigma_D(i+\frac{1}{2})\Delta t/2\varepsilon_0}{1 + \sigma_D(i+\frac{1}{2})\Delta t/2\varepsilon_0}
 \end{aligned} \tag{4-20}$$

In programming the f and g expressions in the computer simulation, it is not necessary to actually vary the loss factor (σ_D). Instead, an auxiliary parameter, x_n , is introduced so as to increase as it goes into the PML. The x_n parameter can be calculated from [66]

$$x_n(i) = \frac{\sigma_D(j)\Delta t}{2\varepsilon_0} = 0.333 \left(\frac{i}{\text{length_pml}} \right)^3, \quad i = \text{length_pml}, \dots, 2, 1, 0. \tag{4-21}$$

It is worth noting that f_{i2} and f_{i3} are different from g_{i2} and g_{i3} only in that they are computed at the half intervals, $i+1/2$. Similarly, the only difference between f_{j2} (f_{j3}) and g_{j2} (g_{j3}) comes from the fact that calculation points are offset by the half intervals, $j+1/2$. Notice that the PML has no effect in the main calculation region of the problem space when f_{i1} and f_{j1} are equal to 0 and f_{i2} , g_{i2} , f_{i3} , g_{i3} , f_{j2} , g_{j2} , f_{j3} , and g_{j3} are all equal to one.

4.2.2 Parameters and Stability

There are several parameters to choose for FDTD computer simulation of dielectric waveguides. First, appropriate computer memory size for calculation needs to be prepared. Basically, larger calculation matrix size will produce better accuracy. But if the matrix is too large, the required time for simulation will be unnecessarily too long. With proper size of the simulation region, size of PML should be considered. We need to make sure that the cell size is adequate for perfectly matching to the outer boundary. Then, parameters that define geometry and material properties of a waveguide need to be considered. They can be the core radius or refractive index of a step-index fiber, the cladding refractive index, or the side length if a fiber to be simulated has square core. Using the parameters to define the cross section, one can create any type of optical fiber. Finally, we need to choose a reasonable value for $\beta = \bar{\beta} \cdot k = 2\pi\bar{\beta} / \lambda$. In other words, what we are trying to find in the FDTD simulation is the wavelength associated with the β value of the desired mode.

We also need to choose a parameter τ in defining a Gaussian pulse source, which excites the waveguide at one end. The expression describing the source is given as

$$S_{Ga} = e^{-(x^2+y^2)/2\tau^2} . \quad (4-22)$$

Also, the number of time steps for sampling data need to be given. Since it is related to the fast Fourier transformation, we need to make sure enough number of data are sampled for good accuracy in the frequency domain. After choosing all appropriate parameters, the computer simulation proceeds by following the steps outlined in the flow chart in Figure 4.3.

To ensure stability of the FDTD algorithm, so that numerical divergence can be avoided, an appropriate time constant (Δt) needs to be selected to satisfy the following stability condition [67],

$$\Delta t \leq \frac{1}{c_{\max} \left[\frac{1}{\Delta x^2} + \frac{1}{\Delta y^2} + \frac{1}{\Delta z^2} \right]^{1/2}} \quad (4.23)$$

where c_{\max} is the maximum wave phase velocity within a given model.

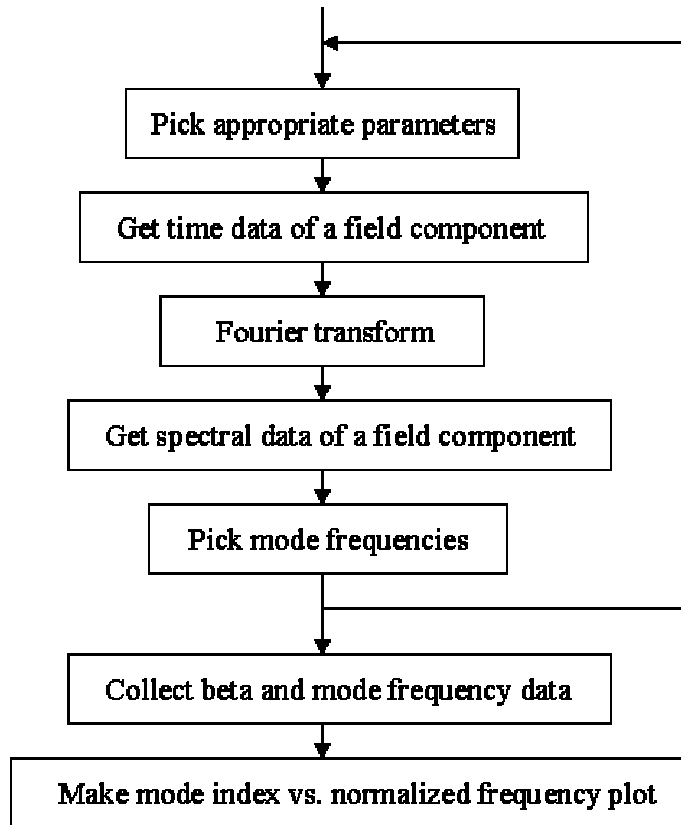


Figure 4.3 FDTD simulation flow chart

4.3 Finite Difference Method (FDM)

The FDTD algorithm works well for finding out the propagation constants of modes as a function of wavelength or normalized frequency for any arbitrary optical waveguide that is uniform along the direction of propagation. In order to plot mode field distributions, however, FDTD seems not to be suitable. As mentioned earlier, a field component with Gaussian spatial distribution is used as the source of excitation. In the time domain, however, the source is an impulse function with a spectrum of constant amplitude in the frequency domain. This source is often referred to as white source.

Basically, the implementation of FDTD requires that light be launched at one fiber end and the data that we are interested in be collected at the other end. Since the source is white, the field distribution from the collected data is a composition of all the mode fields that are allowed in the given optical waveguide. After digital filtering of the data at a discrete point on the waveguide cross section, the amplitude of a mode allowed by the digital filter can be calculated. Repeating this process for every grid point results in total mode field distribution. This process is quite tedious and time consuming, because of the digital filtering and the repetition of filtering process over the entire grid points in the calculation lattice.

There is another method; namely, the finite difference method (FDM) that can be used to produce mode field distributions more easily and quickly. FDM is believed to be first developed by Thom [68] in 1920s for solving nonlinear hydrodynamic equations. Later, this technique was applied to electromagnetic field problems.

The functions used in FDM analyses may have several kinds of variables such as time, space, and temperature. The FDM used here, however, involves only functions of spatial variables, thus it can be implemented by replacing spatial derivatives with finite difference approximations. Starting with Maxwell's equations, the following vector wave equation for the transverse portion of electric field is obtained [69-70],

$$\nabla_t^2 \mathbf{E}_t + (n^2 k^2 - \beta^2) \mathbf{E}_t = \nabla_t \left[\nabla_t \cdot \mathbf{E}_t - \frac{1}{n^2} \nabla_t \cdot (n^2 \mathbf{E}_t) \right] \quad (4-24)$$

By rearranging the terms (4-24), one can write the above equation in a matrix form as

$$\mathbf{P}\mathbf{E}_t = \beta^2\mathbf{E}_t \quad (4-25)$$

where

$$\mathbf{E}_t = \begin{pmatrix} E_x \\ E_y \end{pmatrix} \quad (4-26)$$

and

$$\mathbf{P} = \begin{pmatrix} P_{xx} & P_{xy} \\ P_{yx} & P_{yy} \end{pmatrix} \quad (4-27)$$

The differential operators are defined as

$$P_{xx}E_x = \frac{\partial}{\partial x} \left[\frac{1}{n^2} \frac{\partial(n^2 E_x)}{\partial x} \right] + \frac{\partial^2 E_x}{\partial y^2} + n^2 k^2 E_x \quad (4-28a)$$

$$P_{yy}E_y = \frac{\partial^2 E_y}{\partial x^2} + \frac{\partial}{\partial y} \left[\frac{1}{n^2} \frac{\partial(n^2 E_y)}{\partial y} \right] + n^2 k^2 E_y \quad (4-28b)$$

$$P_{xy}E_y = \frac{\partial}{\partial x} \left[\frac{1}{n^2} \frac{\partial(n^2 E_y)}{\partial y} \right] - \frac{\partial^2 E_y}{\partial x \partial y} \quad (4-28c)$$

$$P_{yx}E_x = \frac{\partial}{\partial y} \left[\frac{1}{n^2} \frac{\partial(n^2 E_x)}{\partial x} \right] - \frac{\partial^2 E_x}{\partial y \partial x} \quad (4-28d)$$

Let $E_x(i,j)$, $E_y(i,j)$, and $n(i,j)$ represent the electric fields and the refractive index at the mesh (i, j) with mesh size Δx and Δy . The finite-difference expressions of (4-28a) and (4-28b) are:

$$\begin{aligned}
 P_{xx}E_x &= \frac{T_x(i+1, j)E_x(i+1, j) - T_x(i, j)E_x(i, j) + T_x(i-1, j)E_x(i-1, j)}{(\Delta x)^2} \\
 &+ \frac{E_x(i, j+1) - 2E_x(i, j) + E_x(i, j-1)}{(\Delta y)^2} + n^2(i, j)k^2E_x(i, j)
 \end{aligned} \tag{4.29a}$$

where

$$\begin{aligned}
 T_x(i \pm 1, j) &= \frac{n^2(i \pm 1, j) + n^2(i, j)}{2n^2(i, j)} \\
 T_x(i, j) &= \frac{n^2(i-1, j) + n^2(i, j)}{2n^2(i-1, j)} + \frac{n^2(i+1, j) + n^2(i, j)}{2n^2(i+1, j)}
 \end{aligned}$$

and

$$\begin{aligned}
 P_{yy}E_y &= \frac{T_y(i, j+1)E_y(i, j+1) - T_y(i, j)E_y(i, j) + T_y(i, j-1)E_y(i, j-1)}{(\Delta y)^2} \\
 &+ \frac{E_y(i+1, j) - 2E_y(i, j) + E_y(i-1, j)}{(\Delta x)^2} + n^2(i, j)k^2E_y(i, j)
 \end{aligned} \tag{4-29b}$$

where

$$\begin{aligned}
 T_x(i, j \pm 1) &= \frac{n^2(i, j \pm 1) + n^2(i, j)}{2n^2(i, j)} \\
 T_x(i, j) &= \frac{n^2(i, j-1) + n^2(i, j)}{2n^2(i, j-1)} + \frac{n^2(i, j+1) + n^2(i, j)}{2n^2(i, j+1)}
 \end{aligned}$$

Similarly, P_{xy} and P_{yx} are expressed as

$$\begin{aligned}
 P_{xy}E_y &= \frac{1}{4\Delta x \Delta y} \left\{ \left[\frac{n^2(i+1, j+1)}{n^2(i+1, j)} - 1 \right] E_y(i+1, j+1) - \left[\frac{n^2(i+1, j-1)}{n^2(i+1, j)} - 1 \right] E_y(i+1, j-1) \right. \\
 &\quad \left. - \left[\frac{n^2(i-1, j+1)}{n^2(i-1, j)} - 1 \right] E_y(i-1, j+1) + \left[\frac{n^2(i-1, j-1)}{n^2(i-1, j)} - 1 \right] E_y(i-1, j-1) \right\}
 \end{aligned} \tag{4-29c}$$

$$P_{yx}E_x = \frac{1}{4\Delta y\Delta x} \left\{ \left[\frac{n^2(i+1, j+1)}{n^2(i, j+1)} - 1 \right] E_x(i+1, j+1) - \left[\frac{n^2(i-1, j+1)}{n^2(i, j+1)} - 1 \right] E_x(i-1, j+1) \right. \\
 \left. - \left[\frac{n^2(i+1, j-1)}{n^2(i, j-1)} - 1 \right] E_x(i+1, j-1) + \left[\frac{n^2(i-1, j-1)}{n^2(i, j-1)} - 1 \right] E_x(i-1, j-1) \right\} \quad (4-29d)$$

Since (4-29a) to (4-29d) are described only in terms of a given refractive index profile and an operating wavelength, the E_x and E_y field distributions can be found by matrix calculation after substituting (4-29) into (4-25).

4.4 Test and Comparison of Methods

A test simulation of a conventional step-index dielectric waveguide is performed to see how well the FDTD and FDM algorithms work and agree with each other. The test waveguide has a core radius of 1 μm , core refractive index (n_1) of 1.45, and cladding refractive index of 1.0. Figure 4.4 compares the normalized propagation constant of the fundamental mode obtained from the exact analytical solution, FDTD, and FDM numerical techniques.

By using the finite difference technique, transverse electric field distributions, E_x and E_y , can be obtained. Figure 4.5 shows the field distributions of the first two modes for the test waveguide at a wavelength of 1.3 μm . It should be mentioned that FDM solutions produce many numerical spurious modes [71]. Thus, we need somehow to differentiate between the true modes and the spurious ones. This can be done by examining the results obtained by FDTD or by looking at mode field distributions and noting that the magnitudes of true modes are much higher than those of spurious modes. The field plots in Figures 4.5 (a) and (b) resemble those of the HE_{11} and TE_{01} modes, respectively [56]. For the operating wavelength of 1.3 μm , the normalized frequency is calculated as

$$V = \frac{2\pi a \sqrt{(n_1^2 - n_2^2)}}{\lambda} = \frac{2\pi \times 1.0e^{-6} \times \sqrt{(1.45^2 - 1.0^2)}}{1.3e^{-6}} = 5.0749$$

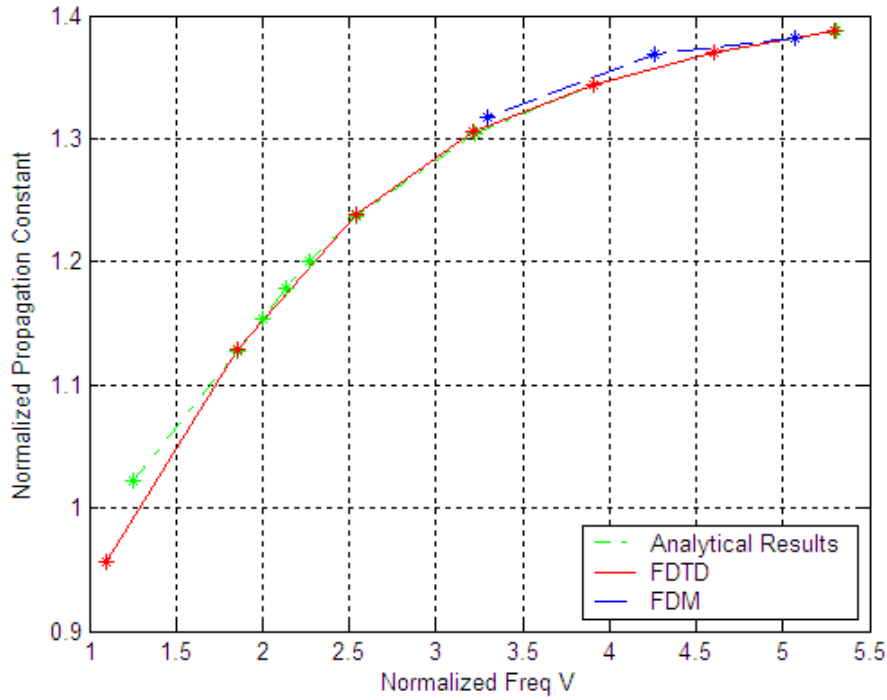
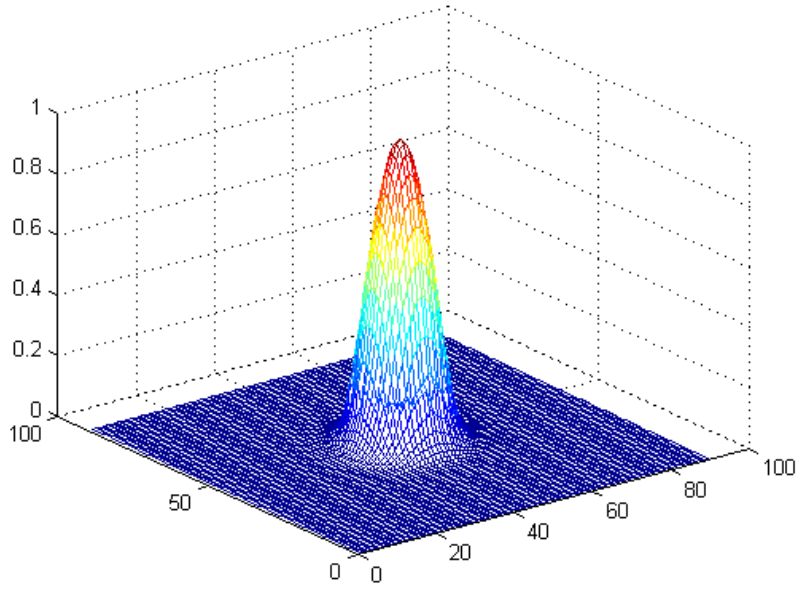
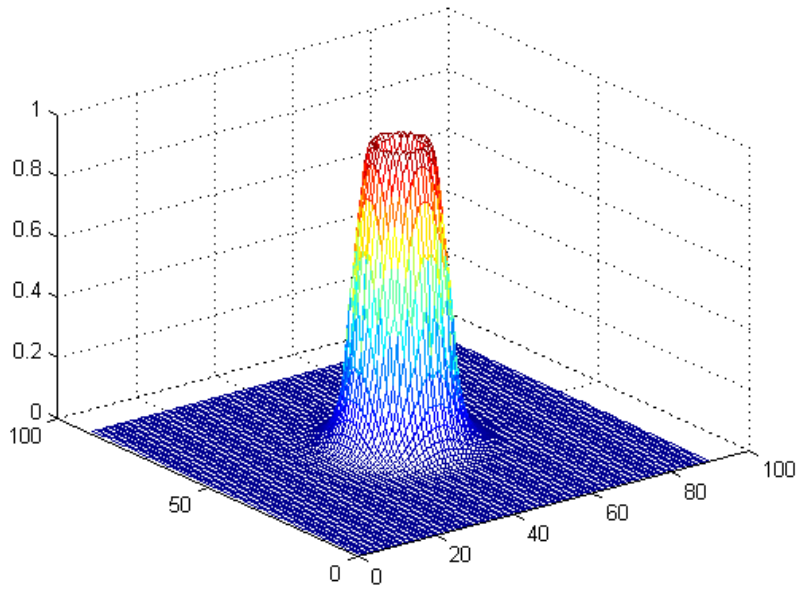


Figure 4.4 Comparison of normalized propagation constants of the fundamental mode in a test waveguide calculated from exact analytical method, FDTD, and FDM

Therefore, it is reasonable to assume that at $\lambda = 1.3 \mu\text{m}$ the test dielectric rod waveguide supports the first four modes below $V = 5.0749$, as can be seen from the well-known mode chart for this waveguide [72].



(a)



(b)

Figure 4.5 Field distributions of the first two modes of the test waveguide

Once the electric field has been determined, the effective area for the fundamental mode can be obtained using the following expression:

$$A_{eff} = \frac{\left(\int_{-\infty}^{\infty} \int_{-\infty}^{\infty} |\vec{E}(x, y)|^2 dx dy \right)^2}{\int_{-\infty}^{\infty} \int_{-\infty}^{\infty} |\vec{E}(x, y)|^4 dx dy} \quad (4-30)$$

where $\vec{E}(x, y)$ is the electric field on a transverse plane. Table 4.1 summarizes the results for effective area at different wavelengths for the test waveguide.

Table 4.1 Effective area for the test dielectric waveguide

Operating wavelength [μm]	Effective area [μm^2]
0.8	1.7925
1.3	2.0624
1.55	2.2148
2.0	2.7066

4.5 Numerical Results for Holey Fibers

So far, two numerical techniques, FDTD and FDM methods, have been formulated and tested for the analysis of axially uniform dielectric waveguides with arbitrary cross-sectional geometry. In this section, these techniques are utilized to perform the simulation of holey fibers.

4.5.1 Propagation Constant

A holey fiber chosen for preliminary investigations has the following specifications. Each air hole has a radius of 0.7 microns. At first, only one ring of holes is considered around the central core region. This ring consists of six air holes and has a radius of 0.85 microns. The outer diameter of the holey fiber is assumed to be 20 microns. The glass portion of the holey fiber has a

refractive index of 1.45. Figure 4.6 illustrates the cross sectional view of the holey fiber. The yellow regions in Figure 4.6 are the air holes. Also, the outside region of the holey fiber is assumed to be air.

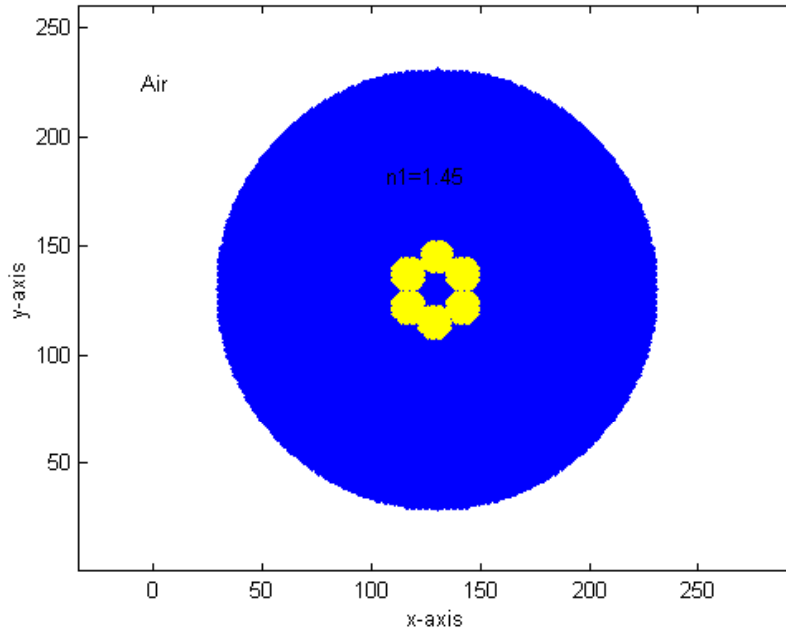


Figure 4.6 Geometry of a holey fiber with one layer of air holes

Figure 4.7 shows the characteristic curves for several lower-order modes of the holey fiber. The red curve illustrates the normalized propagation constant for the first mode versus wavelength, while the blue and green curves show the normalized propagation constants for the second and the third modes, respectively. We now consider holey fibers with more air hole layers. The air holes are arranged in a hexagonal configuration as illustrated in Figure 4.8. With this arrangement of holes, the holey fiber geometry can be described with two parameters only, pitch length (Λ) and diameter (d). The pitch length is the distance between centers of two closest air holes. Since we can identify three layers of air holes in the structure shown in Figure 4.8, it is referred to as three-layer holey fiber. A small air hole at the center can be added or omitted to achieve some desired characteristics. Changing the parameters, Λ and d , a variety of performances can be obtained from the holey fiber.

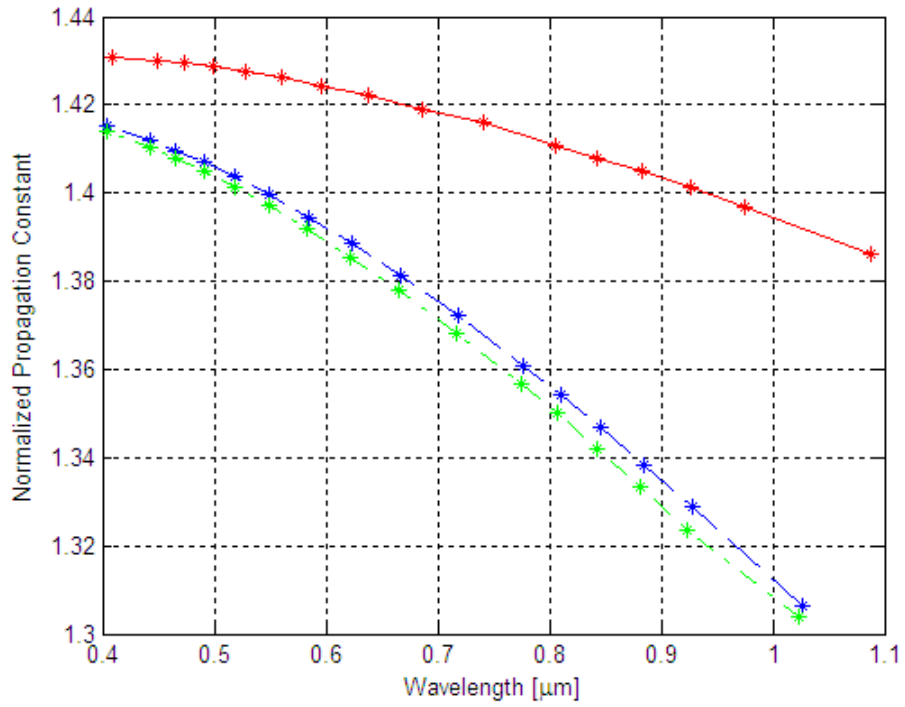


Figure 4.7 Normalized propagation constant versus wavelength for the first three modes in a holey fiber with one layer of air holes

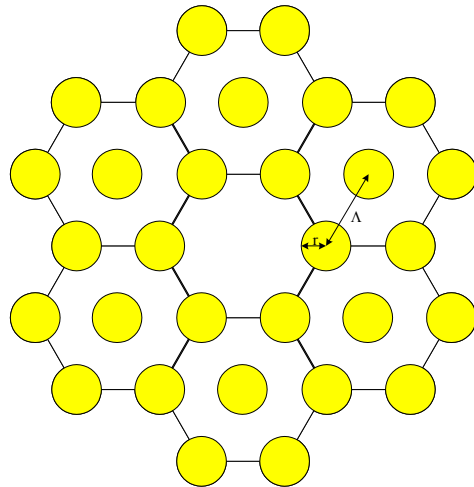


Figure 4.8 Structure of a holey fiber with three layers of air holes in a hexagonal arrangement

As another example, we analyze a holey fiber with a triangular air-hole lattice cladding structure, reported by Bjarklev et al. [73]. The fiber is defined by parameters $\Lambda = 2.0 \mu\text{m}$ and $d = 1.2 \mu\text{m}$. In the abscissa, the normalized frequency is defined the ratio of pitch length over the operating wavelength (Λ/λ). The core index, which is the same as the surrounding medium of the small air holes, is 1.45. The blue curve in Figure 4.9 represents the normalized propagation constant for the fundamental mode reported in [73].

To see how closely the results obtained from FDM and FDTD techniques agree with that in Figure 4.9, a five-layer holey fiber is modeled and analyzed. The difference between the Bjarklev's holey fiber and the five-layer holey fiber analyzed here is that the air-hole cladding structure in our model does not extend to infinity. The air-hole cladding in the five-layer model is surrounded by a dielectric material layer with an outer radius of $12 \mu\text{m}$. The dielectric material everywhere in the five-layer model is assumed to have a refractive index of 1.45. Figure 4.9 also shows the results for the normalized propagation constant of the fundamental mode obtained from FDM and FDTD methods. Comparison of the three curves in Figure 4.9 shows that the results are in remarkably good agreement. In the course of calculations, it was noted that the holey fiber allows only a single mode over the entire frequency range. This fact has already been established by other researchers.

Another interesting point is that decreasing the number of layers of small air holes doesn't affect the propagation constant significantly. This means that the layers close to the center of the holey fiber play a more significant role on its performance. This is demonstrated in Figure 4.10, which compares the results for 3-layer and 5-layer holey fibers with the same ($12 \mu\text{m}$) overall radius. When the normalized frequency is less than 1, which corresponds to operating wavelengths longer than $2.0 \mu\text{m}$, the propagation constant for the 3-layer holey fiber is slightly larger than that for the 5-layer holey fiber. The reason is that the field at longer wavelengths actually sees more of the small air holes.

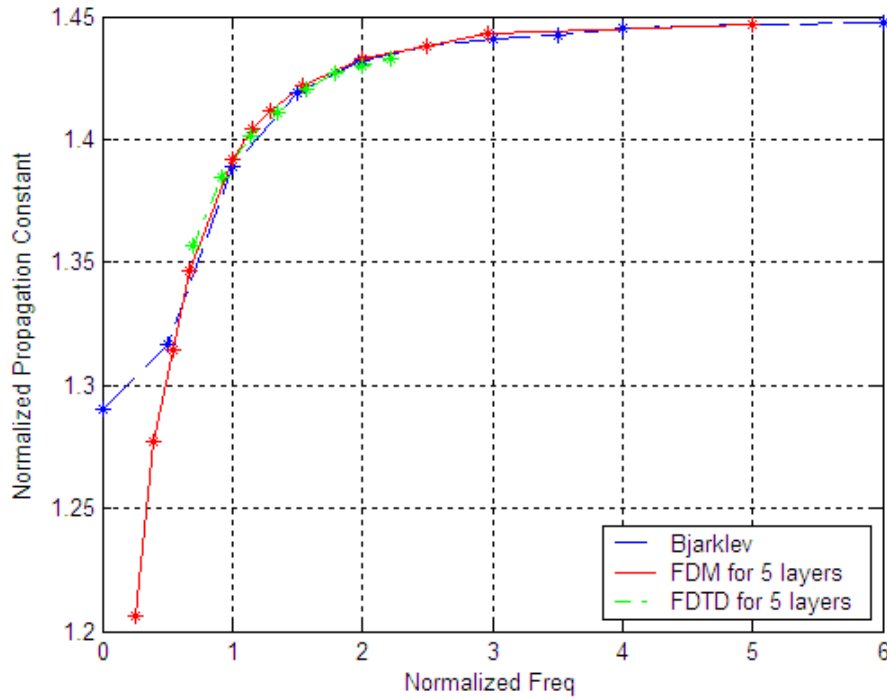


Figure 4.9 Normalized propagation constant of the fundamental mode in a holey fiber with a triangular air-hole lattice cladding structure

Next, the effect of the thickness of the dielectric layer surrounding the air holes is examined. When the outer radius of the holey fiber is reduced from $12\ \mu\text{m}$ to $9\ \mu\text{m}$, no significant change on the propagation constant occurs as shown in Figure 4.11. The propagation constants for the $12\ \mu\text{m}$ and $9\ \mu\text{m}$ radius holey fibers calculated by the FDTD method are almost the same except for the longest wavelength. This is expected because the field of the fundamental mode is nearly entirely confined to a region of $9\ \mu\text{m}$ radius over the wavelength range used in Figure 4.11. Another computer simulation is performed for a 3-layer holey fiber with an air hole at the center. Again the fiber radius is $12\ \mu\text{m}$. Figure 4.12 compares the results for propagation constants of holey fibers with and without the central air hole. The central air hole has a radius of $0.3\ \mu\text{m}$. As expected, the propagation constant for the fiber with central air hole is smaller than that without it.

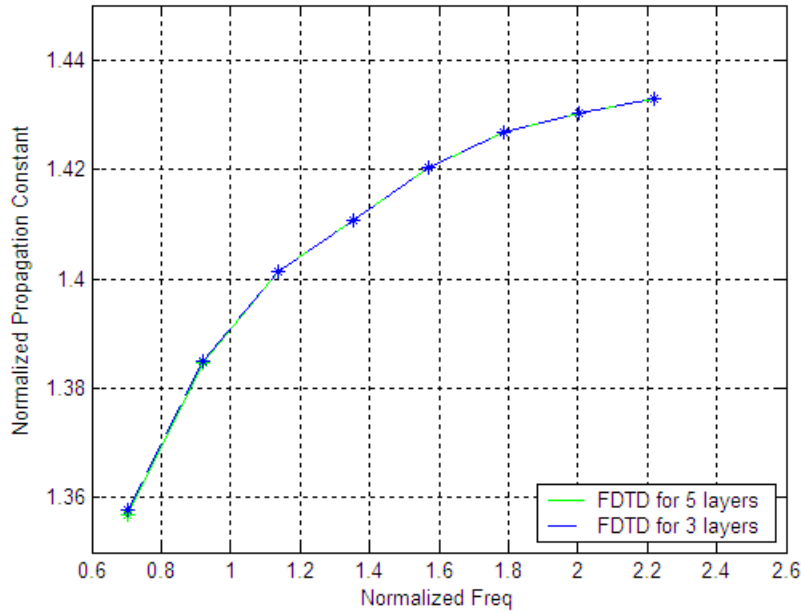


Figure 4.10 Comparison of normalized propagation constants of the fundamental mode in holey fibers with 3- and 5-layer air holes

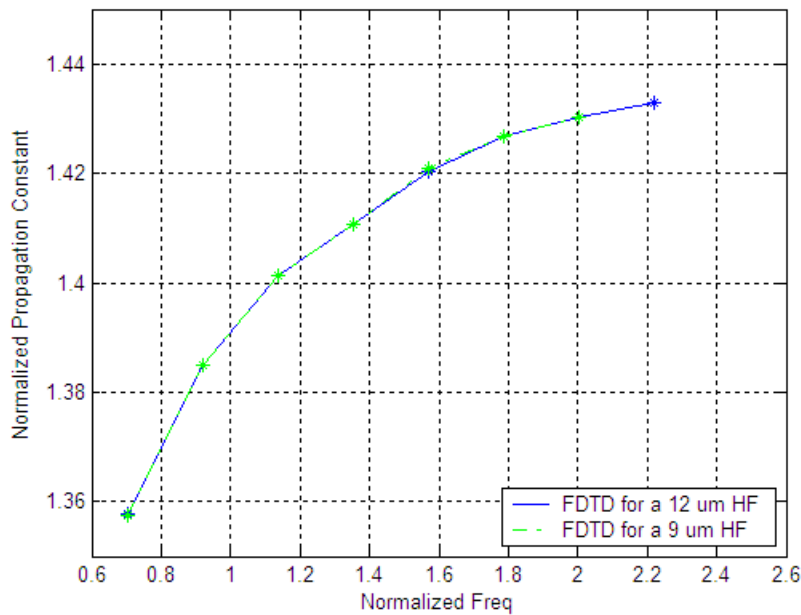


Figure 4.11 Normalized propagation constants of 3-layer holey fibers with different radii

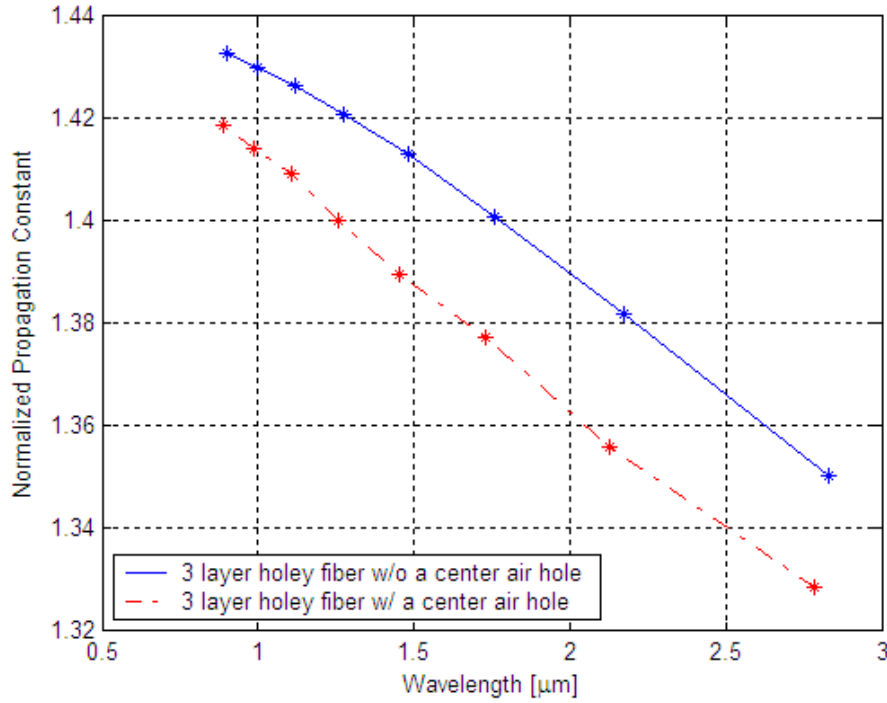
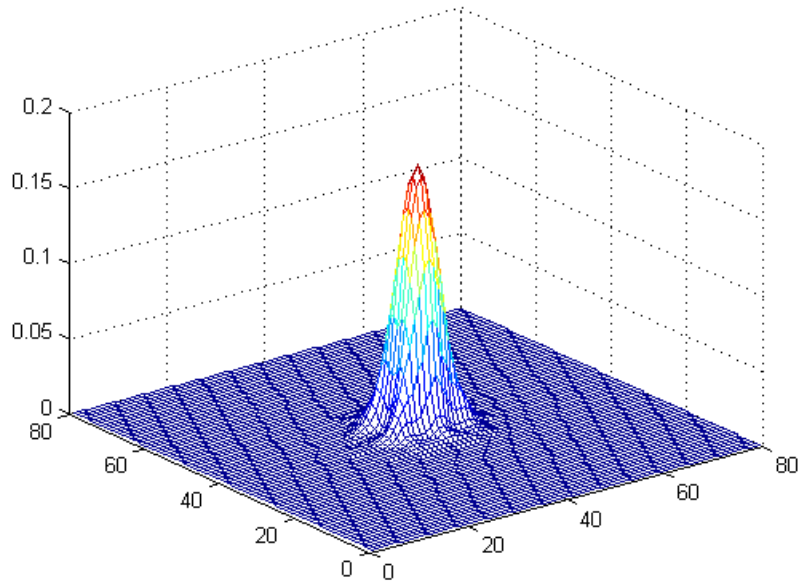


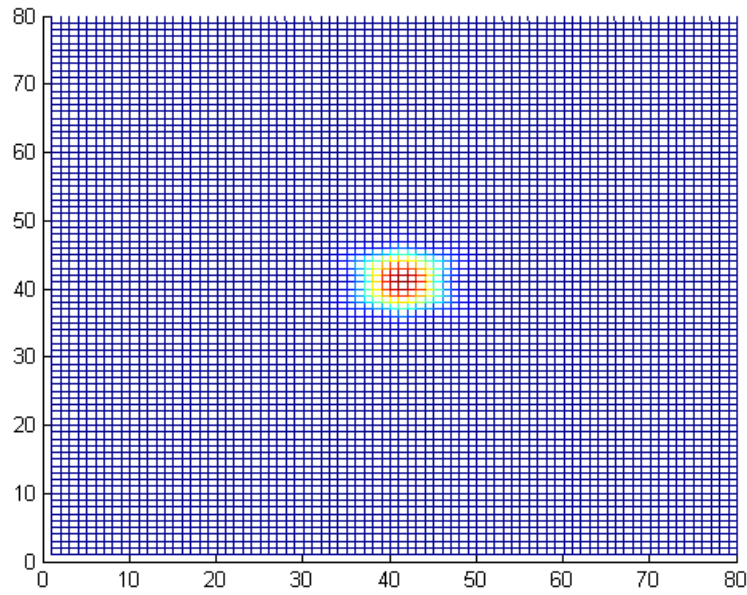
Figure 4.12 Normalized propagation constants for 3-layer holey fibers with and without center air hole

4.5.2 Mode Field Distributions

As mentioned before, the normalized propagation constant of the fundamental modes in 3-layer and 5-layer holey fibers with $9\ \mu\text{m}$ or $12\ \mu\text{m}$ radius are very close because the mode field is largely confined to the central region. To appreciate the confinement of mode to the central region, mode field distributions are calculated using the FDM technique. For this purpose, the 3-layer holey fiber with $9\ \mu\text{m}$ radius is selected. Figure 4.13 shows the field distribution for the E_x component of the fundamental mode at $1.55\ \mu\text{m}$ wavelength. Figure 4.6 (a) is the 3-dimensional view and Figure 4.13 (b) is the top view. Figures 4.14 (a) and (b) show two-dimensional profiles of the field on $x=40$ and $y=40$ planes, respectively. Here, each pixel has an area of $0.3 \times 0.3\ \mu\text{m}^2$. It is noticed that the field distribution appears to be largely Gaussian. However, when the operating wavelength becomes longer, the field assumes a distribution different from the usual Gaussian



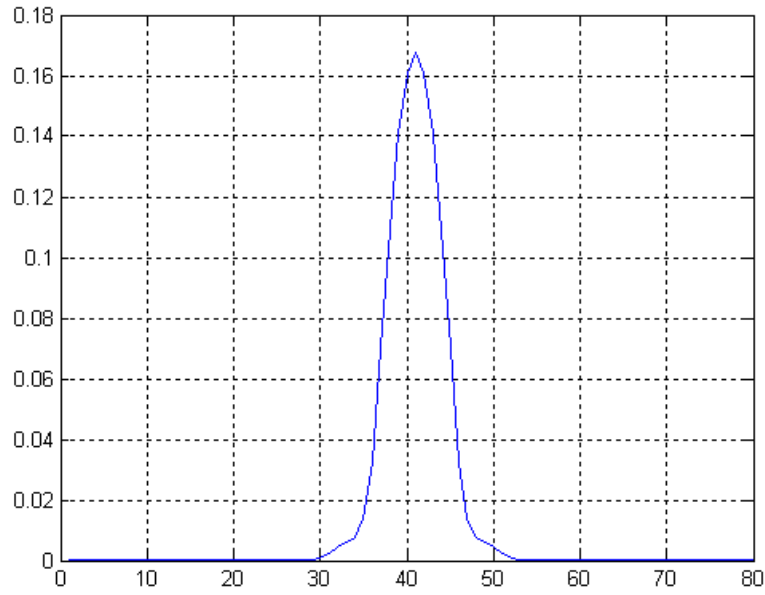
(a)



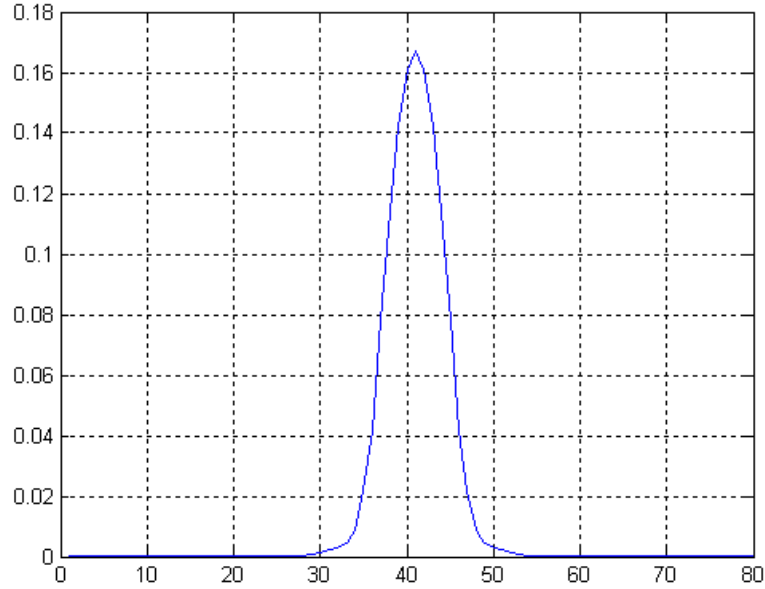
(b)

Figure 4.13 Field distribution for the E_x component of the fundamental mode at $\lambda=1.55 \mu\text{m}$ in a holey fiber with parameters $\Lambda=2.0 \mu\text{m}$ and $d=1.2 \mu\text{m}$ and 3 layers of air holes.

(a) 3-D view, (b) top view



(a)



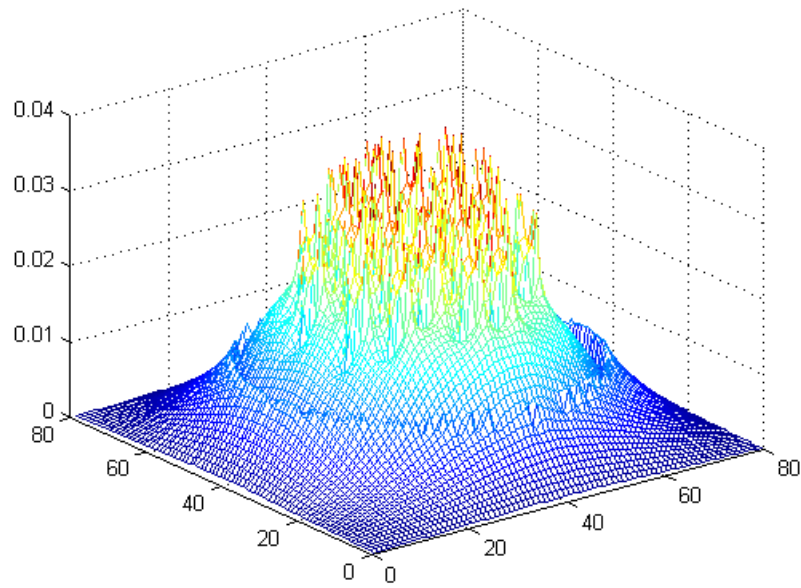
(b)

Figure 4.14 2-D field profiles at $\lambda=1.55 \mu\text{m}$ on planes (a) $x=40$ and (b) $y=40$.

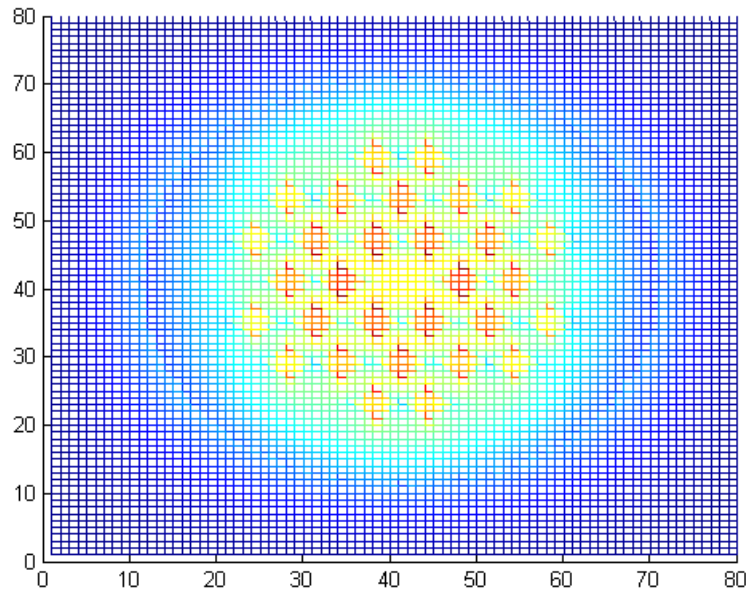
Fiber parameters are the same as those in Figure 4.13.

shape. This can be seen in Figure 4.15, which depicts the distribution of E_x for the fundamental mode at $15.0 \mu\text{m}$ wavelength. It is noted that there are many peaks in the distribution. These peaks occur at the places where small air holes exist.

Next, we examine the field distribution of a holey fiber with a central air hole. Figure 4.16 shows the field distribution for the E_x component of the fundamental mode in a holey fiber with a central air hole of $0.3 \mu\text{m}$ radius. It is observed that there is a dip at the center (on the fiber axis). This is due to the fact that fields tend to have larger concentrations in regions of higher refractive index.

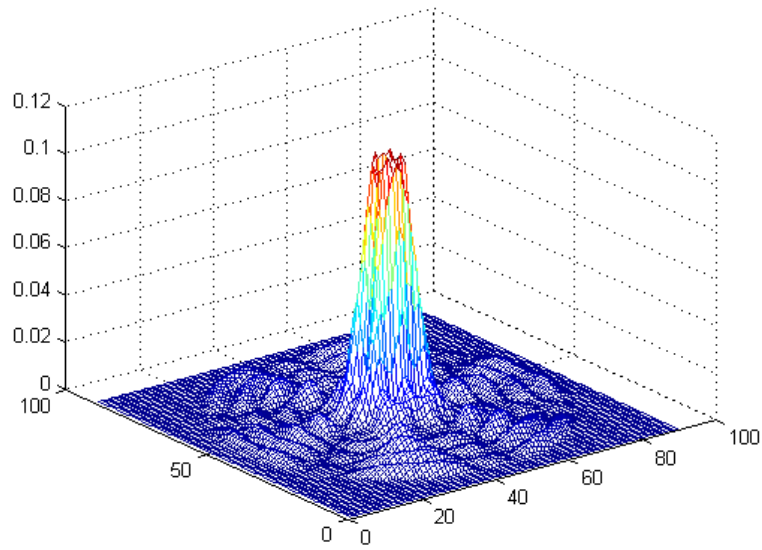


(a)

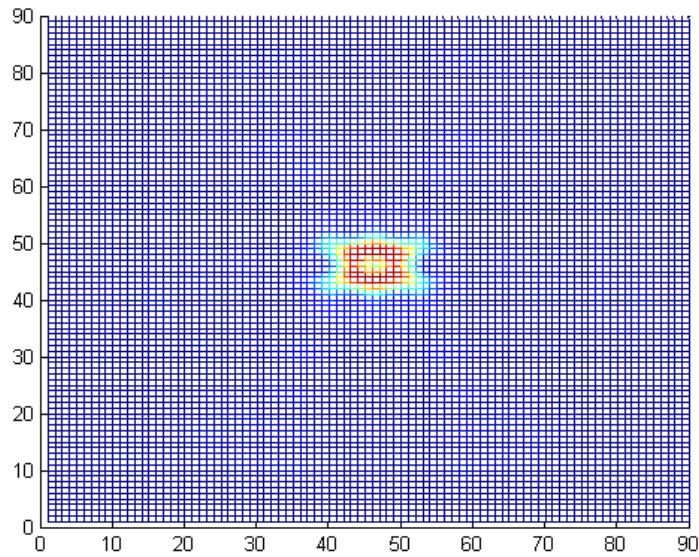


(b)

Figure 4.15 Field distribution for the E_x component of the fundamental mode at $\lambda=15.0$ μm . Fiber parameters are the same as those in Figure 4.13.



(a)



(b)

Figure 4.16 Field distribution for the E_x component of the fundamental mode in a holey fiber with a central air hole of $0.3 \mu\text{m}$ radius. Other parameters of the fiber are the same as those in Figure 4.13.

4.5.3 Effective Area

For the calculation of the effective area, (4-30) is once again utilized for a 3-layer holey fiber with $\Lambda = 2.0 \mu\text{m}$, $d = 1.2 \mu\text{m}$, and $R = 9.0 \mu\text{m}$. The results for the effective area of this fiber are summarized in Table 4.2. It is noted that the effective area tends to increase with the wavelength. This behavior, which was also observed in the step-index test waveguide, should be expected because at longer wavelengths fields spread more into the cladding region, resulting in larger values for the effective area. As noted from Table 4.2, the effective areas are quite small compared to those of the conventional step-index fibers ($50 - 80 \mu\text{m}^2$) in the $1.5\text{-}\mu\text{m}$ wavelength region [74], indicating that these holey fibers are suitable for nonlinear device applications.

Table 4.2 Effective area for a holey fiber with $\Lambda = 2.0 \mu\text{m}$,
 $d = 1.2 \mu\text{m}$, $R = 9.0 \mu\text{m}$ and three layers of air holes

Operating wavelength [μm]	Effective area [μm^2]
0.8	4.5325
1.3	5.1019
1.55	5.5042
2.0	6.5031

4.5.4 Chromatic Dispersion

The normalized propagation constant can be used to evaluate the waveguide dispersion. However, the chromatic dispersion in a single-mode fiber is sum of the waveguide dispersion and material dispersion. In order to directly account for the material dispersion, the glass refractive index is used as a function of wavelength through Sellmeier's equation given in (3-18). The Sellmeier coefficients for pure fused silica have been provided in Chapter 3 (following (3-18)) and thus are not repeated here. It is mentioned that the FDTD algorithm does not easily accommodate the wavelength dependence of refractive indices, thus the FDM results for the normalized propagation constant are used in the evaluation of chromatic dispersion. Once the propagation constant is available, (3-19) can be used to calculate the chromatic dispersion.

First, chromatic dispersion for the test dielectric rod is calculated using the FDM analysis and compared with the exact analytical results. Figure 4.17 shows the chromatic dispersion for the test dielectric rod waveguide. The blue curve is from the analytical solution, while the red curve is obtained for the FDM analysis. As noted, the two results agree well. This gives us confidence that FDM analysis can accurately predict chromatic dispersion in holey fibers.

Next, the holey fiber that was investigated in the previous section is chosen for further study of chromatic dispersion. This is a fiber with 5 layers of holes and parameters $\Lambda = 2.0 \mu\text{m}$ and $d = 1.2 \mu\text{m}$. Figure 4.18 shows both the chromatic dispersion and the waveguide dispersion (material dispersion not included). Compared with the waveguide dispersion that is about 70 ps/nm-km over the wavelength range from 0.7 μm to 1.7 μm , the chromatic dispersion changes more extensively from -140 to 85 ps/nm-km over the same wavelength range. It is noticed that the chromatic dispersion is zero-crossing around 0.9- μm wavelength.

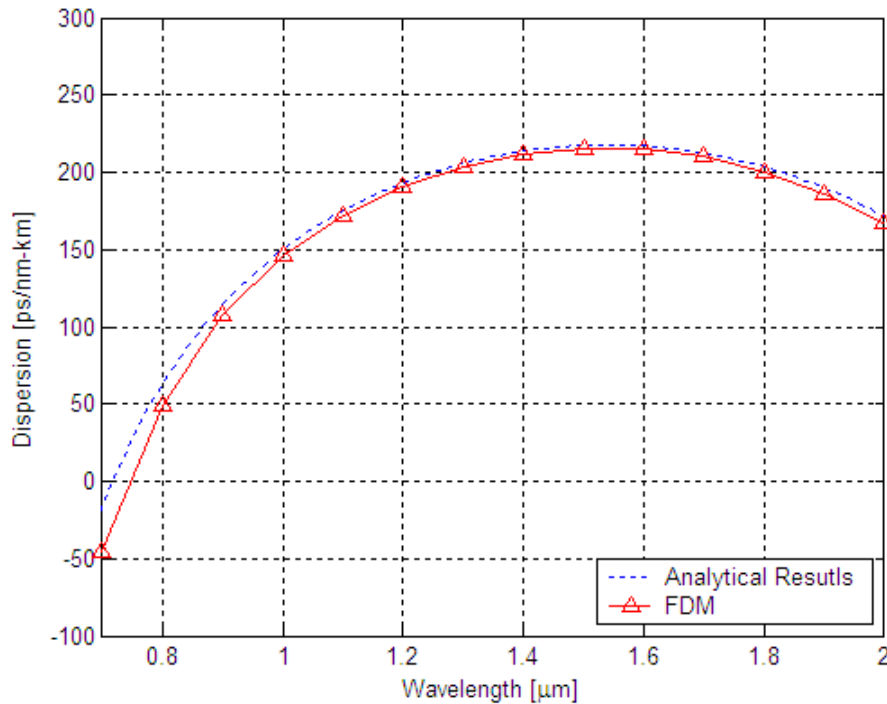


Figure 4.17 Comparison of chromatic dispersions for the test dielectric rod waveguide calculated from exact analytical solution and the FDM analysis

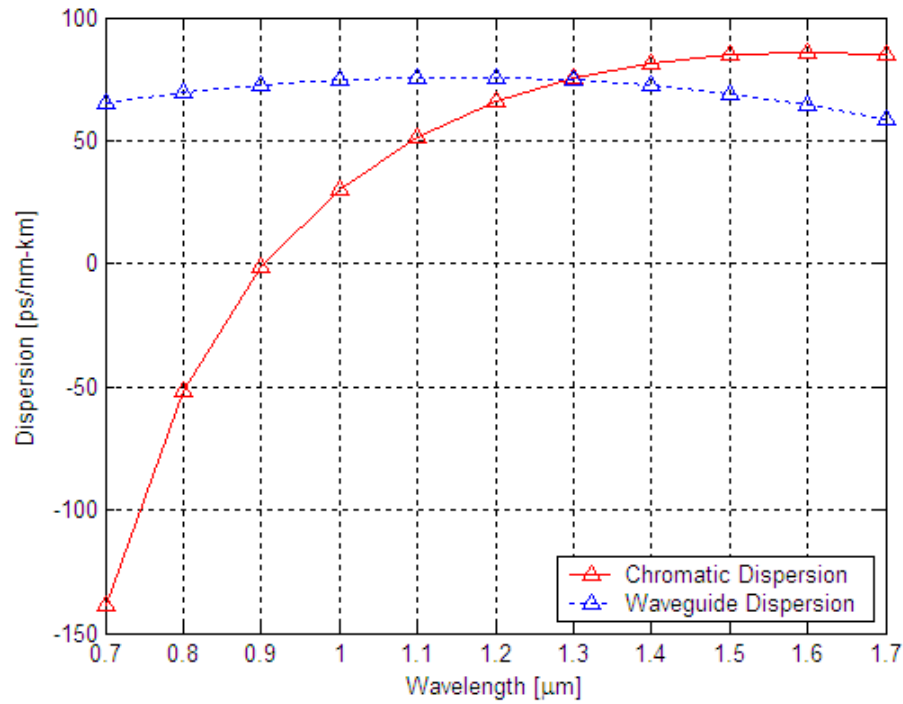


Figure 4.18 Waveguide and chromatic dispersions in a holey fiber with 5 layers of air holes and parameters $\Lambda = 2.0 \mu\text{m}$ and $d = 1.2 \mu\text{m}$

Chapter 5

Microstructure Optical Fibers with Random Cladding Index Distributions

Photonic crystal fibers with one- and two-dimensional periodic cladding index distributions were studied in chapters 3 and 4, respectively. In this chapter, the investigation is extended to cases with random cladding index distributions. Since the optical fibers under investigation here do not have periodicity, they are referred to as *microstructure optical fibers* instead of photonic crystal fibers. The goal is to find out if the microstructure optical fibers with random cladding index distributions have electromagnetic properties similar to those of photonic crystal fibers with periodic index distributions. First, microstructure optical fibers with one-dimensional random cladding index distributions in the radial direction are studied by using vector-wave analytical solutions. Then, holey optical fibers with random air-hole distributions are designed and analyzed numerically.

5.1 Microstructure Optical Fibers with One-Dimensional Random Cladding Index Distributions

In Chapter 3, transmission properties of one-dimensional cylindrical photonic crystal waveguides, including mode characteristics, chromatic dispersion, field profiles, and effective area, were calculated using a systematic 4×4 matrix approach based on vector field analytical solutions. Now, the periodic radial cladding index distribution is changed to a random index

distribution in several of such fibers considered as reference waveguides. Table 5.1 summarizes the parameters of 5 reference fibers whose cladding index distributions will be randomized and then their properties studied. All reference fibers have a high-index core with radius of $1.0 \mu\text{m}$ as defined in Figure 3.1 (a).

The first reference fiber has a thickness of $0.3 \mu\text{m}$ for each air and glass layer with a total of 12 layers (including the central core and the outer cladding region). Thus, with 10 inner cladding layers the cladding thickness (d_c) is $3.0 \mu\text{m}$, from $r = r_1$ to $r = r_{N-1}$. All other reference fibers have about the same total inner cladding thickness, but have smaller thickness for individual glass and air layers. As a result the number of layers is larger, varying from 32 for fiber 2 to 150 for fiber 5 as indicated in Table 5.1. Since the fields of the fundamental mode in all reference fibers decay to negligible values beyond $r > 3.0 \mu\text{m}$, the choice of total cladding thickness of about $3.0 \mu\text{m}$ is reasonable.

Table 5.1 Parameters of the 5 reference fibers, which are modified to assume random cladding index distributions

Fiber	d_a [μm]	d_g [μm]	Number of cladding layers	d_c [μm]
1	0.3	0.3	12	3.0
2	0.1	0.1	32	3.0
3	0.07	0.07	44	2.94
4	0.04	0.04	76	2.96
5	0.02	0.02	150	2.96

In each reference fiber, the inner cladding ($r_1 < r < r_{N-1}$) is replaced with the same number of alternating air/glass layers with random thickness such that $d_c \approx 3.0 \mu\text{m}$ is maintained and at the same time the thickness ratio of glass/air remains unchanged. In doing so, first uniform random numbers ranging from 0 to 1 and with equal probability are generated. Then, these random numbers are scaled such that their sum becomes equal to about 3.0. For example to modify fiber 1, such that its inner cladding assumes a random index distribution, 10 random numbers are first

generated. Then, since in fiber 1 the thickness ratio of glass/air is 1 and thus the sum of the total air layers should be $0.3 \times 5 = 1.5 \mu\text{m}$, the first 5 out of 10 random numbers are scaled in order to make their sum equal to 1.5. The same process is repeated for glass layers using the second set of 5 random numbers.

Using the above-described procedure to create one-dimensional cylindrical microstructure optical fibers with random cladding index distributions, 10 different random fibers corresponding to each reference fiber in Table 5.1 are generated and their transmission properties evaluated. In particular, normalized propagation constant, chromatic dispersion, and effective area are calculated, and their average, minimum and maximum values are compared with those of the reference fibers.

Figures 5.1 to 5.5 show the results for one-dimensional microstructure optical fibers with random cladding index distributions. Plot (a) in each figure shows the normalized propagation constant ($\bar{\beta}$) versus wavelength (λ) for the fundamental mode. In these figures, the red curves represent the normalized propagation constants for the reference fibers with parameters as in Table 5.1. The blue curves correspond to the average normalized propagation constants from 10 different random fibers, while the green and the cyan (sky-blue color) curves illustrate the maximum and minimum values of the normalized propagation constants, respectively.

Plot (b) in each figure shows the chromatic dispersion, which is calculated using the results for the normalized propagation constant $\bar{\beta}$ in (3-18). The color designations in these figures are identical to those used in parts (a) described above. The results for the average, minimum and maximum values of effective area are presented in part (c) in each figure. The calculation of effective areas is performed with the help of (3-20). It is noticed that deviation of the normalized propagation constants in shorter wavelength is smaller than that of the normalized propagation constants in longer wavelength as explained in section 3.4.

Comparison of results for the average values of normalized propagation constant, chromatic dispersion, and effective area with the corresponding results for the reference fibers indicates that they are generally in good agreement; however, the agreement gets better as the number of layers increases. In fact, for fiber 5 with 150 layers the average results for normalized propagation

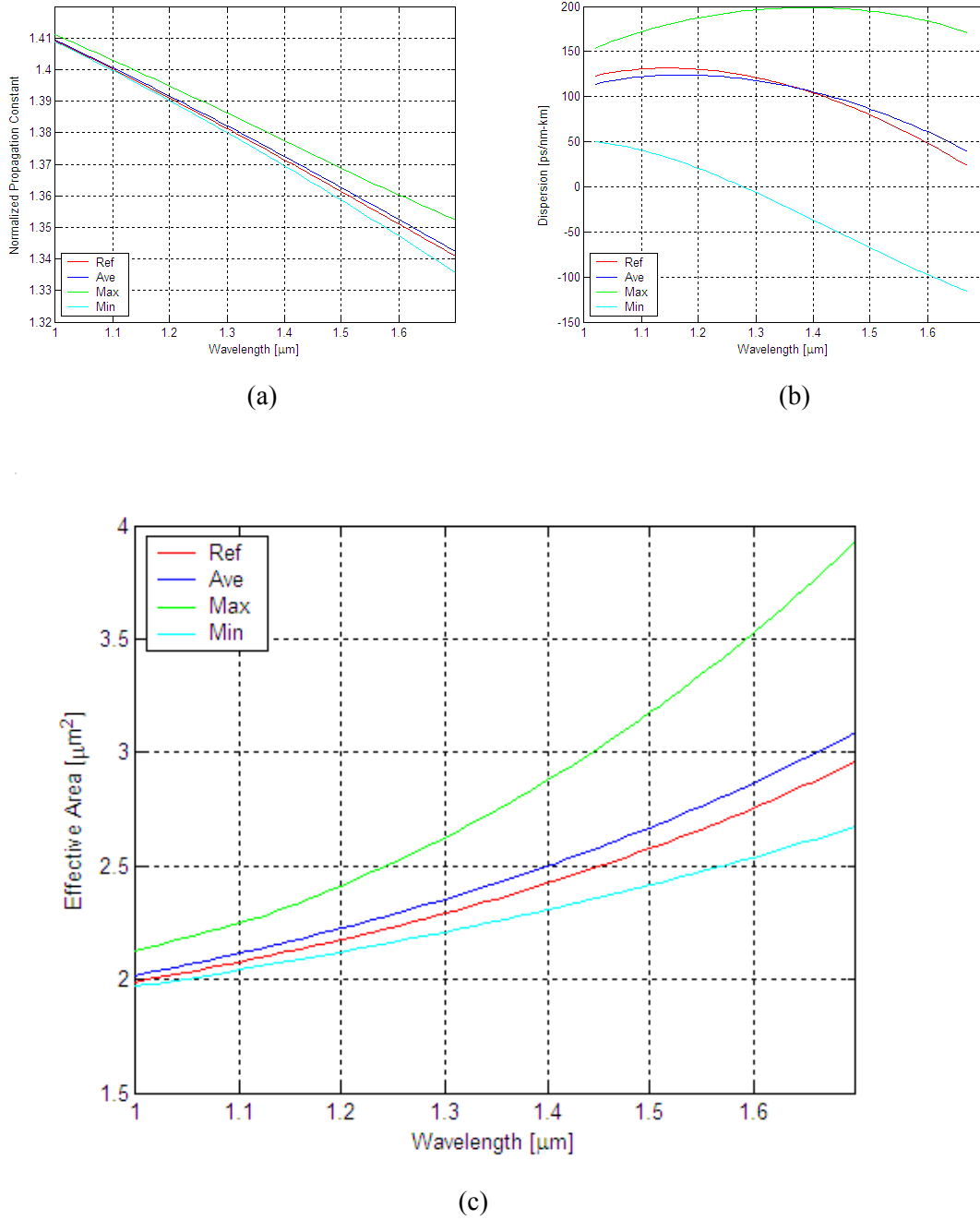


Figure 5.1 Comparison of (a) normalized propagation constants, (b) dispersions, and (c) effective areas for reference fiber 1 ($r_1 = 1.0 \mu\text{m}$, $d_a = d_g = 0.3 \mu\text{m}$, and $N = 12$) and its random variations

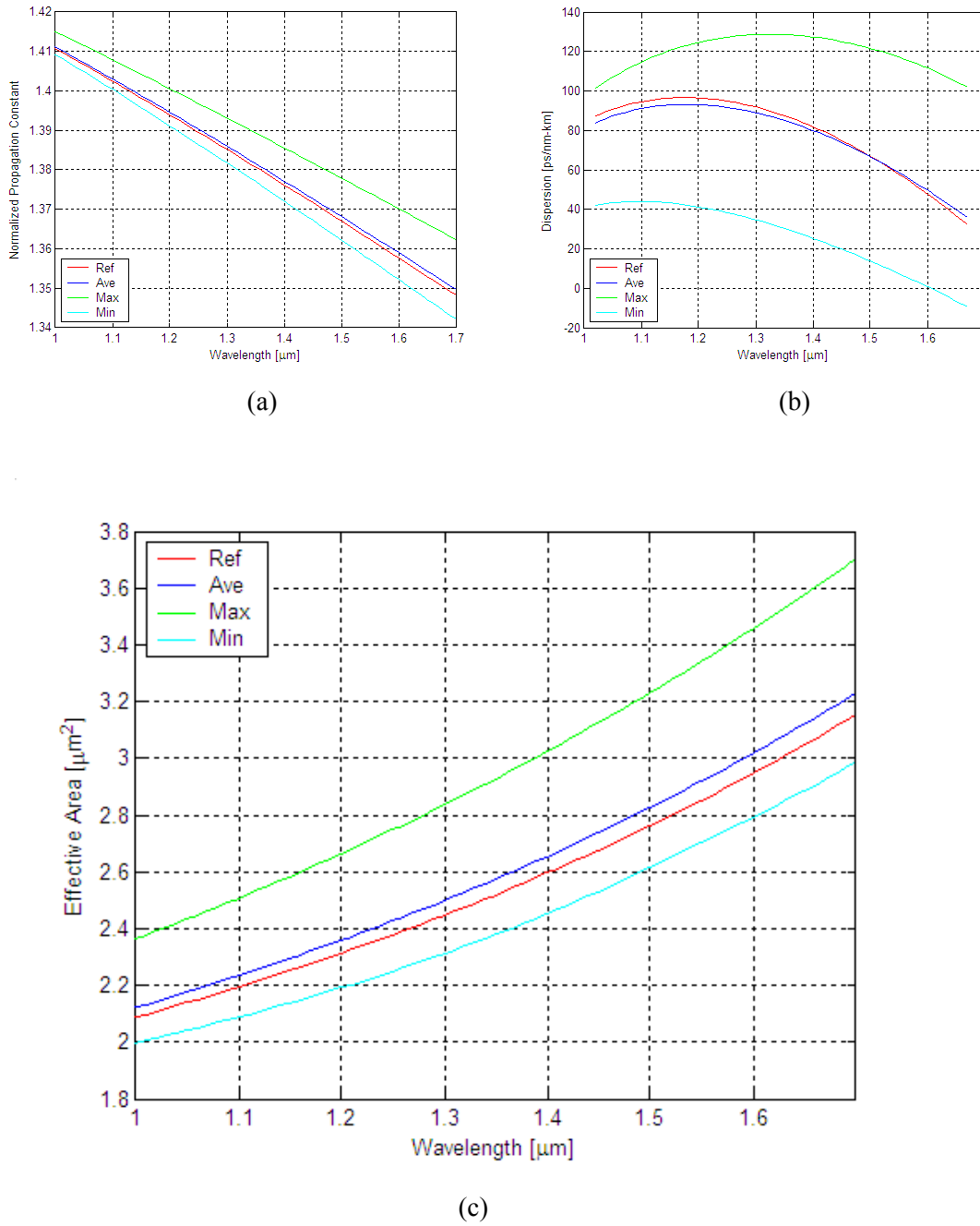


Figure 5.2 Comparison of (a) normalized propagation constants, (b) dispersions, and (c) effective areas for reference fiber 2 ($r_1 = 1.0 \mu\text{m}$, $d_a = d_g = 0.1 \mu\text{m}$, and $N = 32$) and its random variations

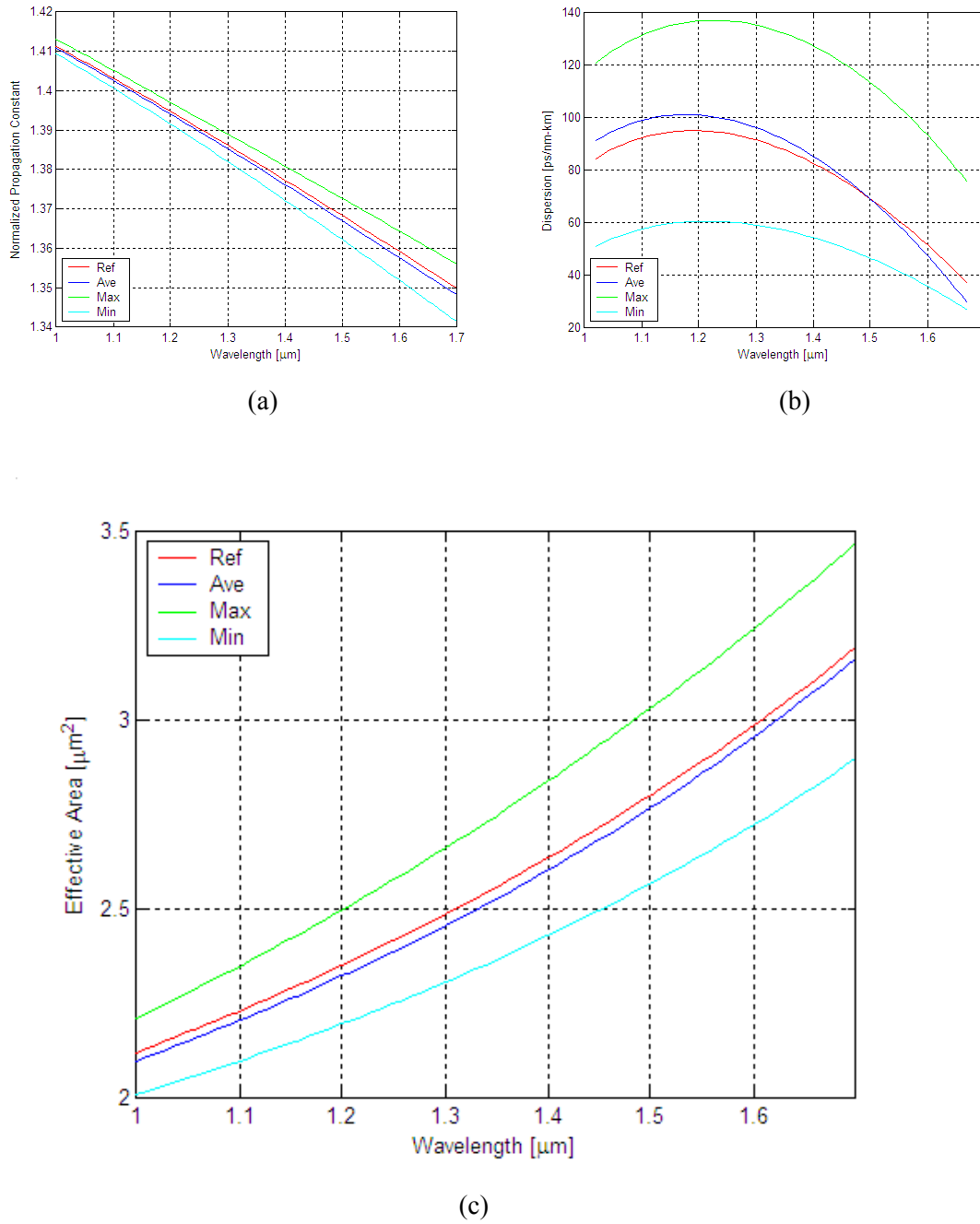


Figure 5.3 Comparison of (a) normalized propagation constants, (b) dispersions, and (c) effective areas for reference fiber 3 ($r_1 = 1.0 \mu\text{m}$, $d_a = d_g = 0.07 \mu\text{m}$, and $N = 44$) and its random variations

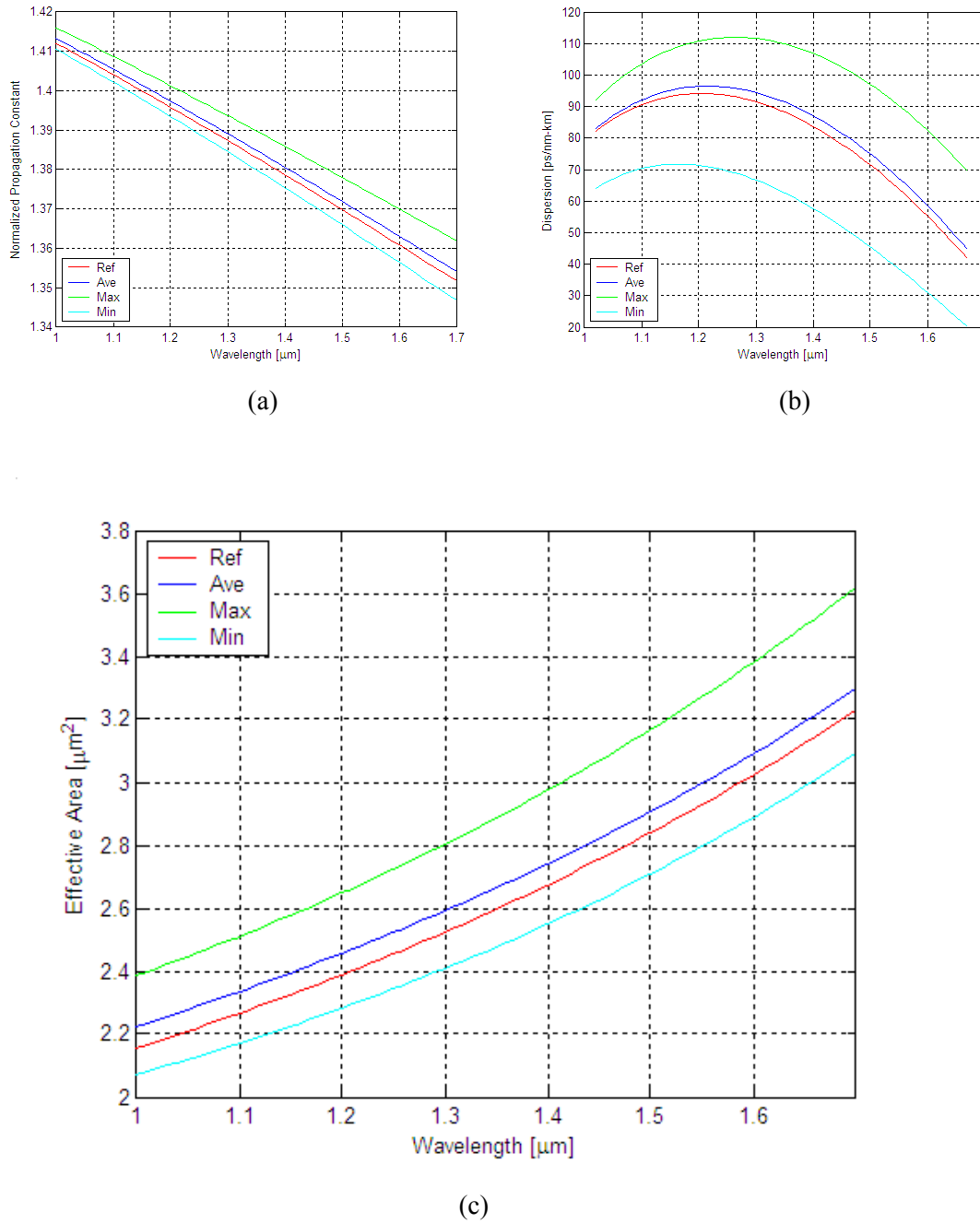


Figure 5.4 Comparison of (a) normalized propagation constants, (b) dispersions, and (c) effective areas for reference fiber 4 ($r_1 = 1.0 \mu\text{m}$, $d_a = d_g = 0.04 \mu\text{m}$, and $N = 76$) and its random variations

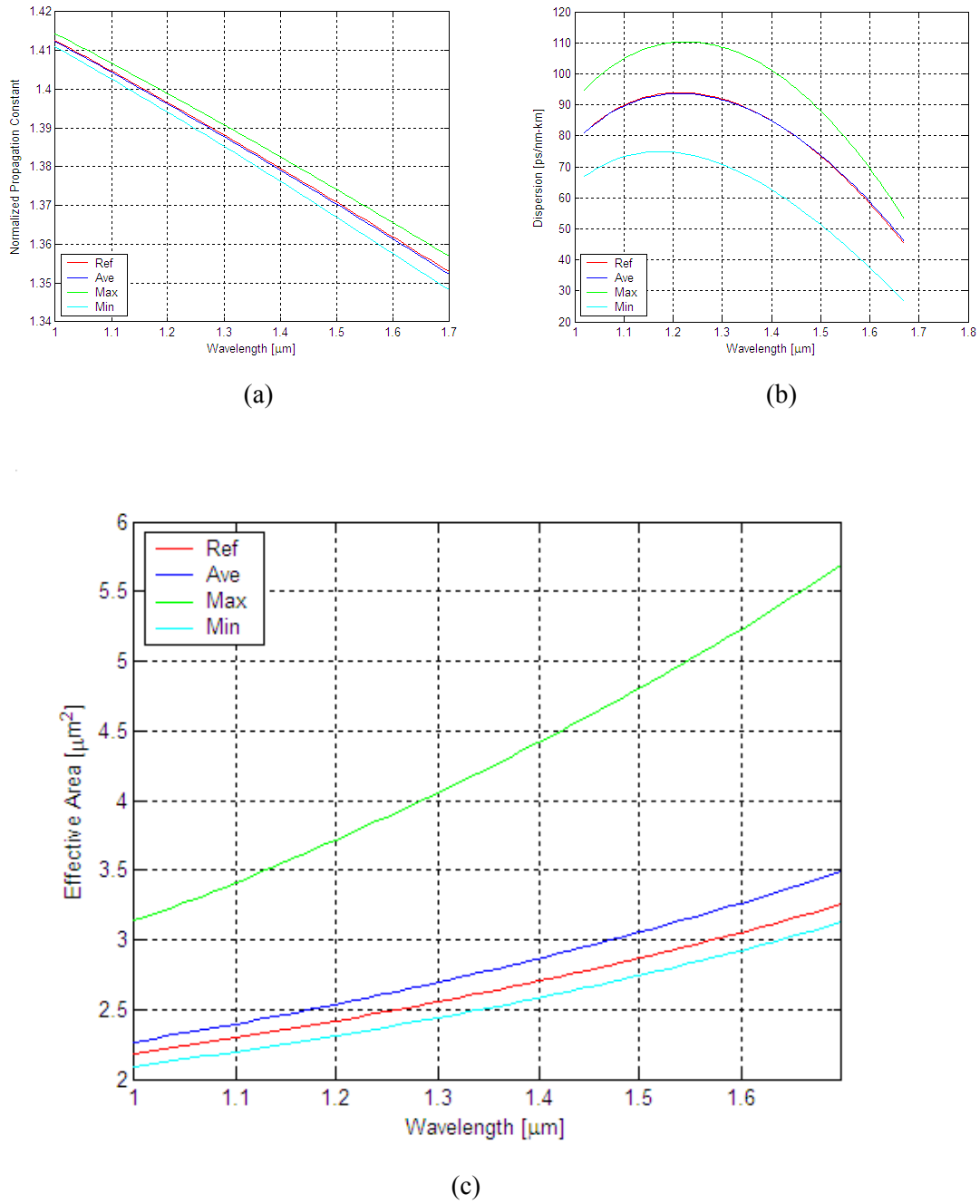


Figure 5.5 Comparison of (a) normalized propagation constants, (b) dispersions, and (c) effective areas for reference fiber 5 ($r_1 = 1.0 \mu\text{m}$, $d_a = d_g = 0.02 \mu\text{m}$, and $N = 150$) and its random variations

constant and dispersion calculated after randomizing the cladding layers are essentially indistinguishable from those of the reference fiber as seen in Figures 5.5 (a) and (b). Many simulations have also been performed with layer thicknesses larger than $0.3 \mu\text{m}$, but in these cases the differences between the average and reference values were substantial. Overall, it can be concluded that, in order to have close agreement between the average and reference results, the layer thicknesses should be about one-tenth of wavelength or smaller. The examination of minimum and maximum values in Figures 5.1 to 5.5 indicates that they are significantly different from the reference values. This, however, should not be of concern, because, first of all, the probability of occurrence for a minimum or maximum dispersion, effective area, or any other property is very small. Moreover, *in practical microstructure waveguides/fibers with random cladding index distributions in the cross sectional plane as well as along the propagation direction, these are the average values of transmission properties which matter and not the properties of specific segments of the waveguide.*

It is also interesting to note that the effective area in all fibers examined above is very small ($2 - 3 \mu\text{m}^2$), indicating that these microstructure optical fibers are well suited for nonlinear optical devices. In fact, the need for low-cost and highly nonlinear optical fibers has been the prime motivation for the development of holey fibers with random-hole distributions. And Virginia Tech has been one of the main research institutes in this area.

Next, we examine the impact of the glass/air ratio on transmission properties of microstructure optical fibers. Considering the reference fiber 5 with $N = 150$, for which the agreement between the results pertaining to periodic and random cladding index distributions was better, the glass/air ratio in the cladding region is changed from 0.5/0.5 to 0.7/0.3 or 0.3/0.7. Figure 5.6 shows (a) the normalized propagation constant, (b) chromatic dispersion, and (c) effective area for the case when the glass/air ratio is 0.7/0.3, while Figure 5.7 shows the three propagation properties when this ratio is 0.3/0.7. It is noted that there are still overall good agreements between the reference and the average results. One thing that is different from fiber 5 is that the chromatic dispersion in Figure 5.6 is zero at about $1.43 \mu\text{m}$. This is due to the increased glass portion in the cladding region.

For quantitative comparison of average and reference results of Figures 5.1 to 5.7, Table 5.2 tabulates the percentage difference in dispersion and effective area at $1.3 \mu\text{m}$ and $1.55 \mu\text{m}$.

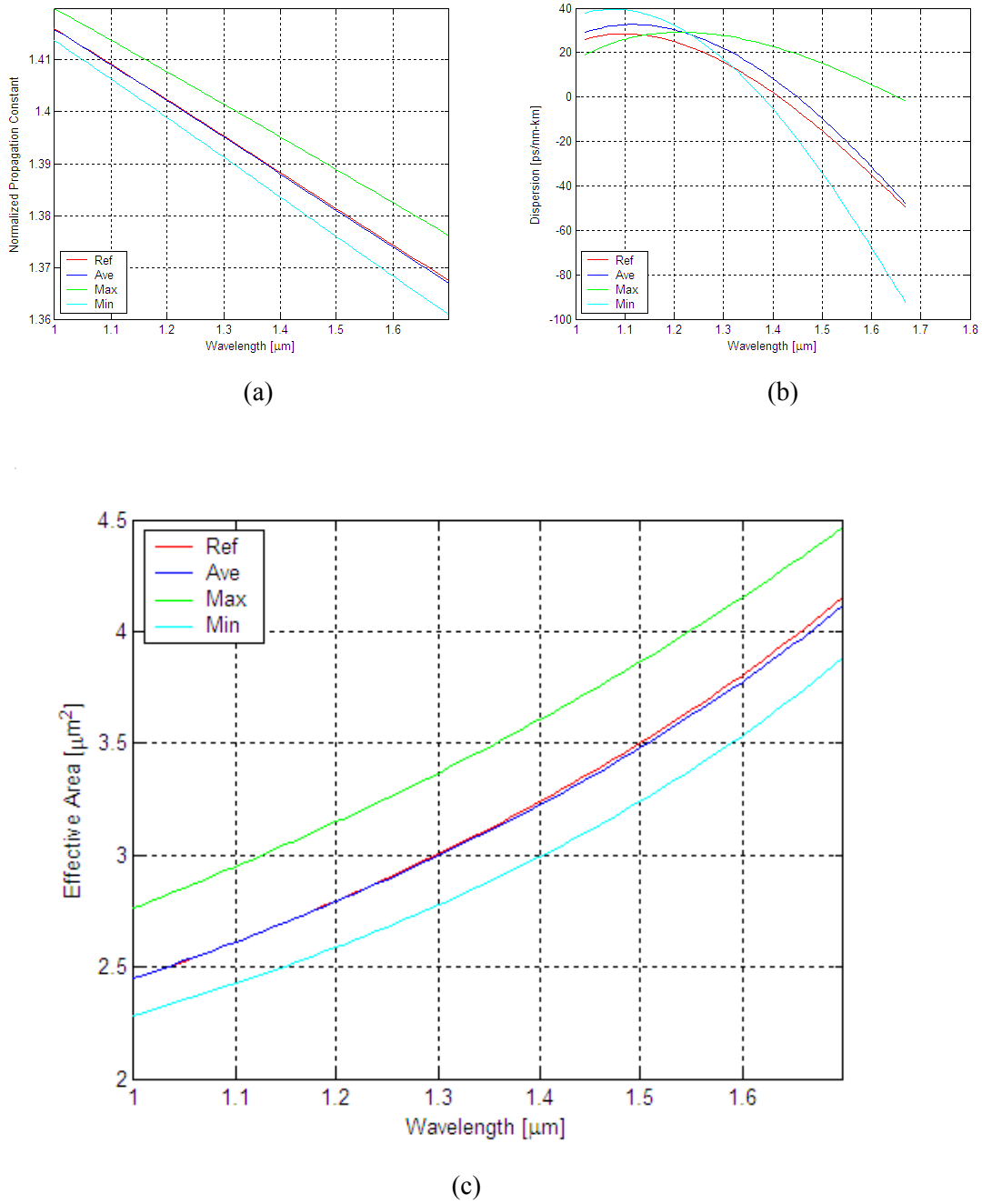


Figure 5.6 Comparison of (a) normalized propagation constants, (b) dispersions, and (c) effective areas for a microstructure fiber with glass/air ratio of 0.7/0.3 ($r_1 = 1.0 \mu\text{m}$, $d_a = 0.012 \mu\text{m}$, $d_g = 0.028 \mu\text{m}$ and $N = 150$) and its random variations

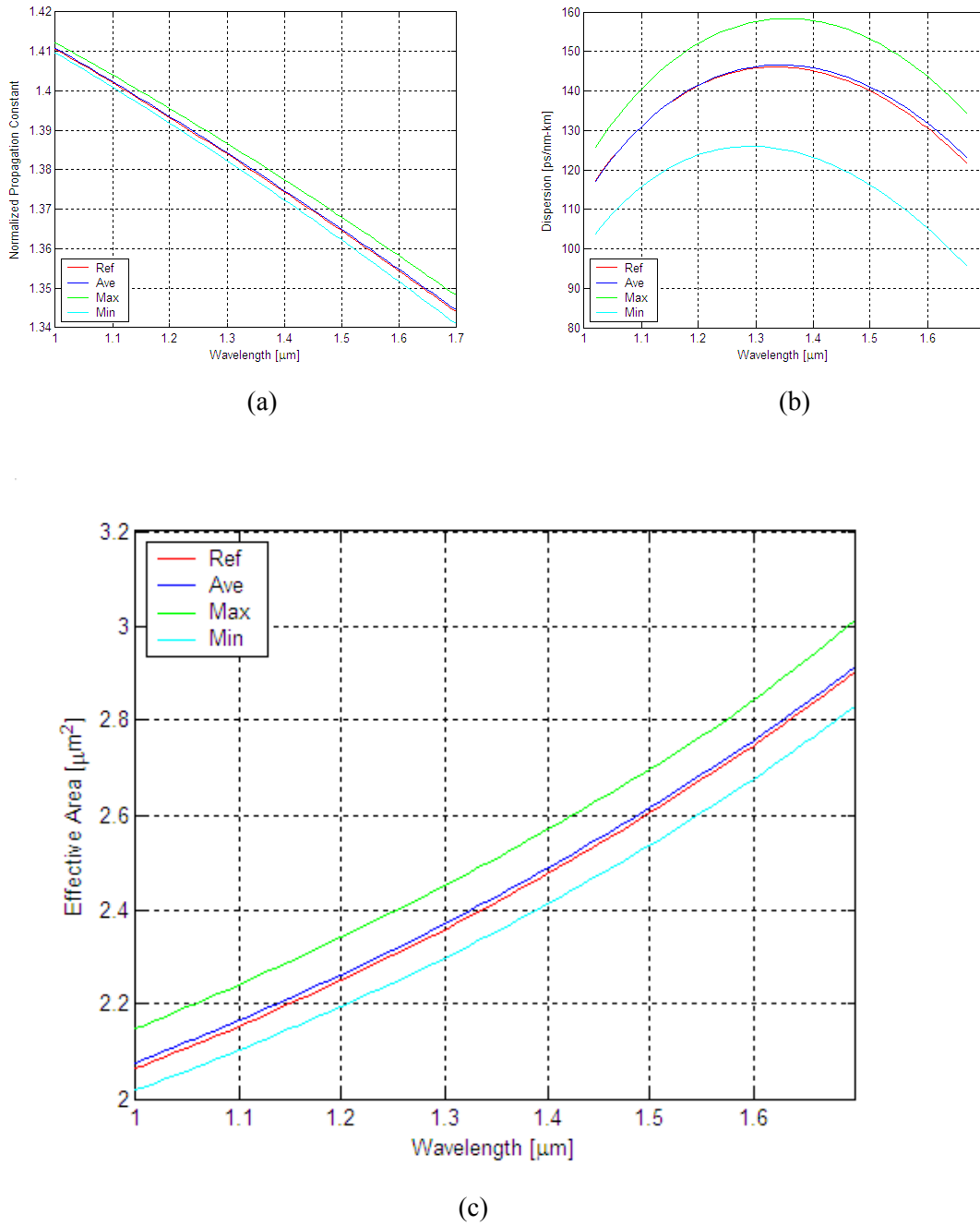


Figure 5.7 Comparison of (a) normalized propagation constants, (b) dispersions, and (c) effective areas for a microstructure fiber with glass/air ratio of 0.3/0.7 ($r_1 = 1.0 \mu\text{m}$, $d_a = 0.028 \mu\text{m}$, $d_g = 0.012 \mu\text{m}$ and $N = 150$) and its random variations

First it is noticed that results of Figure 5.2 show the percentage difference less than 5 % between the average and reference in both dispersion and effective area. Only in terms of dispersion, results of Figure 5.5 indicate – 0.3-% and 0.7-% differences at 1.3 μm and 1.55 μm , respectively, which are negligible. And effective area results of Figures 5.6 and 5.7 show there are remarkable agreement between the average and reference.

Table 5.2 Percentage difference in dispersion and effective area

Figure	Dispersion [%]		Effective area [%]	
	1.3 μm	1.55 μm	1.3 μm	1.55 μm
5.1	-2.6558	14.7933	2.7357	3.7678
5.2	-3.0961	1.2649	2.1207	2.3795
5.3	5.14887	-3.2186	-1.2341	-1.1112
5.4	3.2371	5.3564	2.6865	2.2879
5.5	-0.3136	0.6929	5.4929	6.6932
5.6	39.8875	19.2644	-0.2603	-0.7050
5.7	0.2926	0.8628	0.4987	0.4169

5.2 Holey Fibers with Random Air-Hole Distributions

In chapter 4, holey fibers with periodically arranged identical air holes in their claddings were investigated. However, the periodicity of air holes and their identical size are not necessary conditions for maintaining guided light propagation along the fiber. It is recalled that two mechanisms contribute to light guidance in photonic crystal fibers, (i) total internal reflection due to the difference between the core refractive index and the average cladding index, and (ii) constructive interference effect due to the periodic arrangement of identical air holes. When the air holes become random in size, location, or both, the second mechanism can no longer exist, but the index difference between the core and cladding can still provide light confinement and hence guidance of light along the fiber.

Randomization of air holes may be achieved by randomly varying one or more of the following three parameters,

- (1) radial coordinates of the centers of air holes,
- (2) azimuthal (ϕ) coordinates of the centers of air holes,
- (3) size (radii) of air holes.

The first two parameters describe the location of air holes. Randomization may also be achieved by varying the shape of air holes, but this type of change cannot be easily implemented in the numerical analysis and thus is not considered here. Figure 5.8 illustrates a simplified visualization for the three random parameters. In this section, holey fibers in which all the above three parameters are varied randomly are analyzed.

5.2.1 Simulation Results by FDTD Method

In order to examine transmission properties of holey fibers with random distributions of air holes, the FDTD method is utilized first. Using a random hole generator program, many holey fibers with random hole distributions were created and computer-simulated. Here several examples of holey fibers with random air hole distributions are given. Let us begin with the holey fiber with parameters $\Lambda = 2.0 \mu\text{m}$ and $d = 1.2 \mu\text{m}$ which was studied in chapter 4. If we imagine a circle formed by connecting the inner-most points to the center of the six-inner air holes, we can consider a fictitious circle as the core boundary of the holey fiber. The radius of this fictitious core is $1.4 \mu\text{m}$. The random hole generator is programmed to make sure that silica glass fills inside of the core radius.

Figure 5.9 shows examples of holey fibers that guide a single mode in the wavelength range of $1.2 \mu\text{m}$ to $1.6 \mu\text{m}$. The gray and dark regions correspond to silica glass and air holes, respectively. Figure 5.10 illustrates the spectrum of the holey fiber with 120 air holes as shown in Figure 5.9 (b). It is noticed that there is only one mode with high power spectral density at $1.4861 \mu\text{m}$. On the other hand, Figure 5.11 shows examples of holey fibers that can guide a few modes. The spectrum for the holey fiber of Figure 5.11 (b) is shown in Figure 5.12. Clearly, it is noticed that there are three modes at wavelengths $1.3716 \mu\text{m}$, $1.4112 \mu\text{m}$, and $1.4878 \mu\text{m}$.

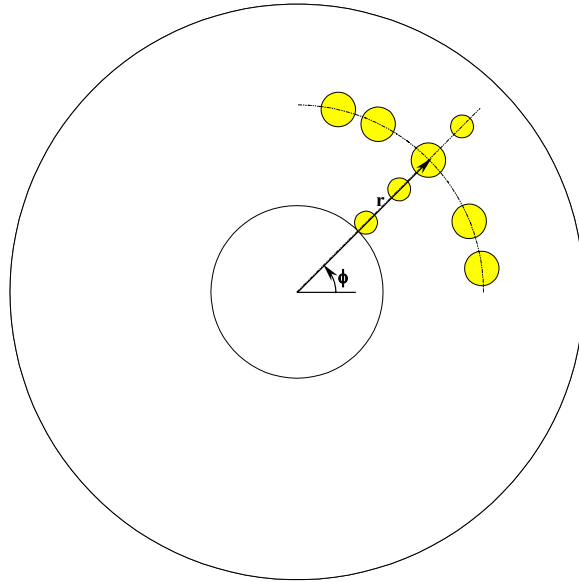


Figure 5.8 Simplified visualization for randomly varying three parameters of air holes

Other holey fibers were also examined to see if the possibility of having only a single mode will be improved. For example, the number of air holes was increased to 150 from 120 in the fiber of Figure 5.9 and then to 400. However, it turned out that these fibers also support a few modes. In view of waveguide structures, no special distinction between microstructure optical fibers guiding a single mode or a few modes is observed. Nonetheless it is expected that air holes around the core region play important role for the mode characteristics.

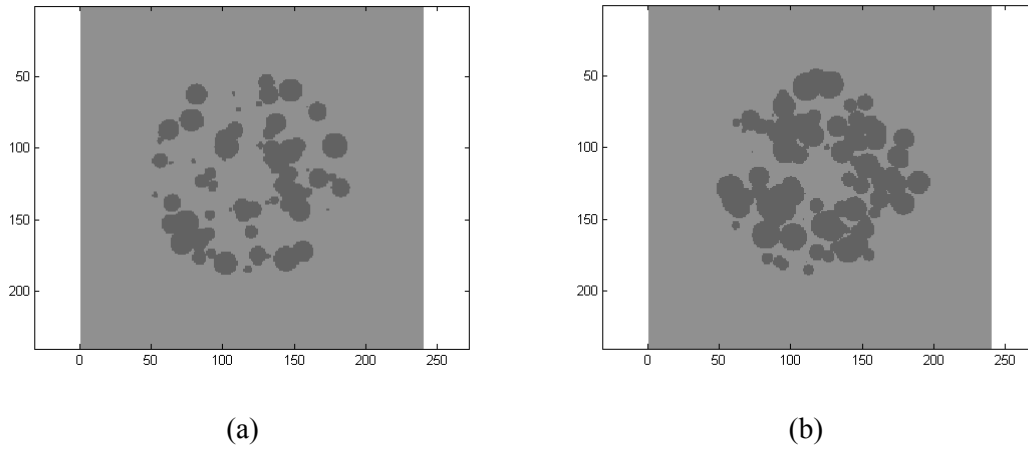


Figure 5.9 Cross-sectional view of holey fibers with (a) 80 air holes, and (b) 120 air holes, which guide only a single mode

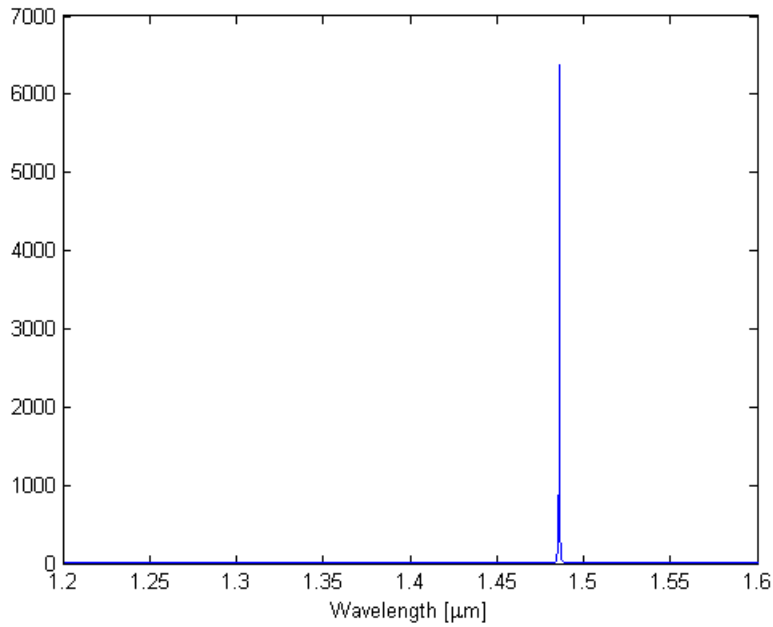


Figure 5.10 Spectrum for the holey fiber of Figure 5.9 (b)

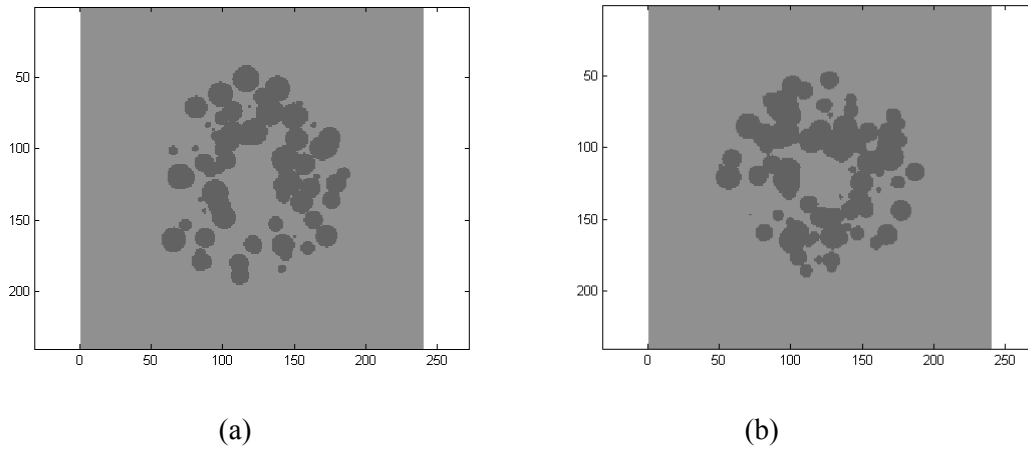


Figure 5.11 Cross-sectional view of holey fibers with (a) 80 air holes and (b) 120 air holes, which guide a few modes.

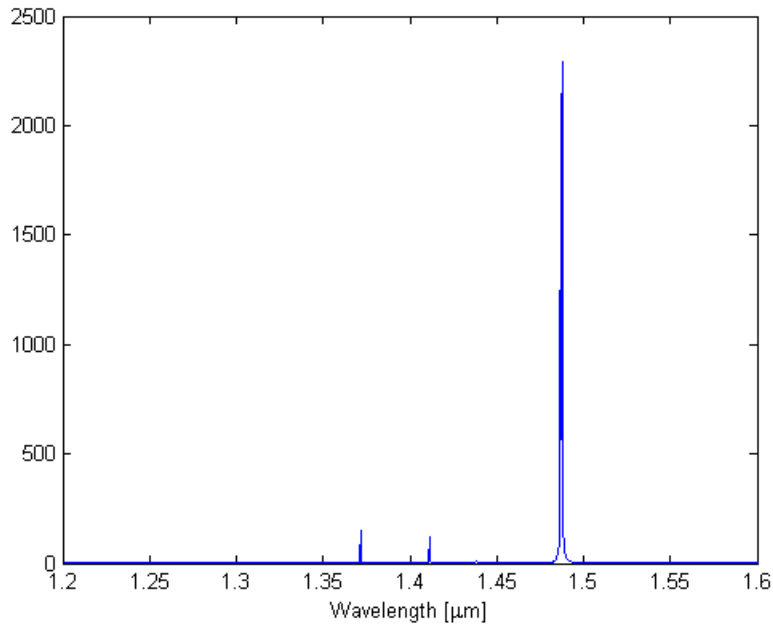


Figure 5.12 Spectrum for the holey fiber of Figure 5.11 (b)

5.2.2 Simulation Results by FDM

Once the mode characteristics of random holey fibers are investigated by the FDTD method, other propagation properties including mode field profile, effective area, and chromatic dispersion are computed by using the FDM technique. In the study of the 1D cylindrical microstructure optical fibers, 10 different random fibers corresponding to each one of 5 different reference fibers were generated and their transmission properties evaluated in section 5.1. However, when it comes to the 2D microstructure optical fibers, it is rather difficult to do similar comparison between a reference fiber and random air-holed fibers, because not only maintaining the same area ratio of glass/air for random holey fibers as for a reference photonic crystal fiber is not easy process, but also computer-simulation for 2D microstructure optical fibers by FDTD and FDM over interesting wavelength region with fine resolution is very time-consuming. Therefore, first the procedure to find a holey fiber with random air-hole distributions that is providing a single mode is presented and the transmission properties of the holey fiber is evaluated in this section. It is noted that about the same size of the core region is maintained as that of the 2D periodic photonic crystal fibers in chapter 4.

Considering from the previous section that holey fibers with random air-hole distributions can provide a strong fundamental mode to be propagated, now the random hole generator program is employed to generate random air holes for holey fibers. Figure 5.13 shows an example that is generated by the program. Again, the radius of a fictitious core is set to be $1.4 \mu\text{m}$, which is filled with silica glass. The area of air regions is $58.0 \mu\text{m}^2$. Based on FDTD simulation, this example fiber is turned out to provide a few modes around the wavelength range of $1.3 \mu\text{m}$ and $1.55 \mu\text{m}$. Several other holey fibers with random air-hole distributions with the radius of the core region $1.4 \mu\text{m}$ are created and analyzed, but all of them are guiding a few modes.

Therefore, computer-simulations are performed after reducing the radius of the fictitious core to $1.0 \mu\text{m}$ to try to have a single mode guiding. What is observed is that some cases are providing a single mode but most of cases are still providing a few modes. Figure 5.14 shows an example holey fiber with random air-hole distributions, out of 5 holey fibers generated, which is found to support a single mode. Here, 200 air holes are generated and the area of air regions is $53.76 \mu\text{m}^2$.

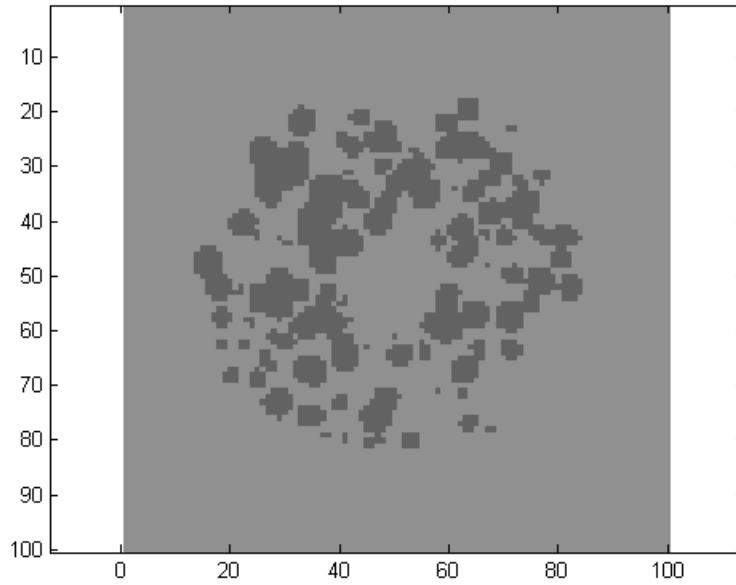


Figure 5.13 A cross-sectional view of an example holey fiber with 200 air holes, which is guiding a few modes

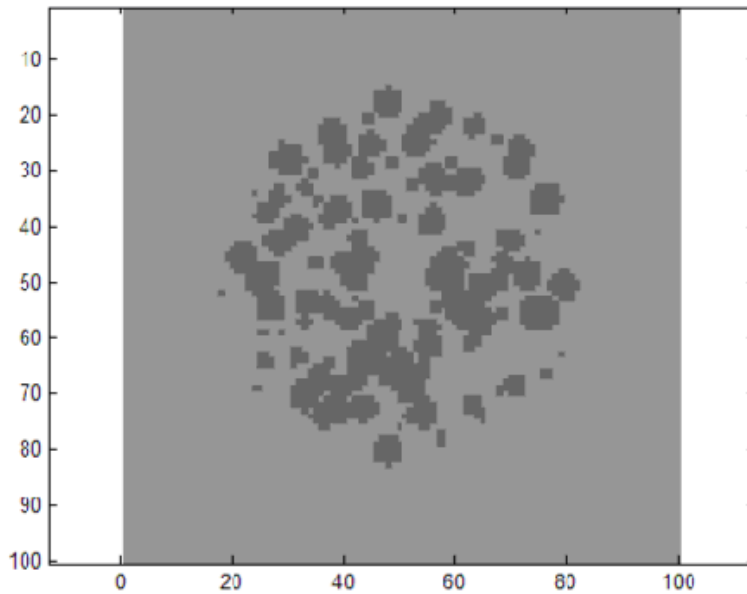


Figure 5.14 A cross-sectional view of an example holey fiber with 200 air holes, which is guiding a single mode

More investigations on the holey fiber of Figure 5.14 is performed by using FDM to find out a chromatic dispersion, a mode field distribution, and effective areas. Incorporating the material dispersion, the result of dispersion is shown in Figure 5.15. It is noticed that the fiber is providing the positive dispersion over the wavelength range between 1.1 μm and 1.55 μm . Particularly, the chromatic dispersion at 1.3 μm is 89.3254 ps/nm-km and at 1.55 μm 84.1994 ps/nm-km. Field distribution for the E_x component of the fundamental mode at 1.55- μm wavelength is shown in Figure 5.16 and is observed that most energy is confined within the core region. Weak ripples in the magnitude around the core come from the clustered regions of high refractive index, which are not observed in holey fibers with periodic air-hole distributions. Effective areas are also computed and tabulated in Table 5.3. It is noted that the effective areas are very small compared with those for the conventional step-index fiber, thus the holey fibers could be useful for applications to nonlinear devices.

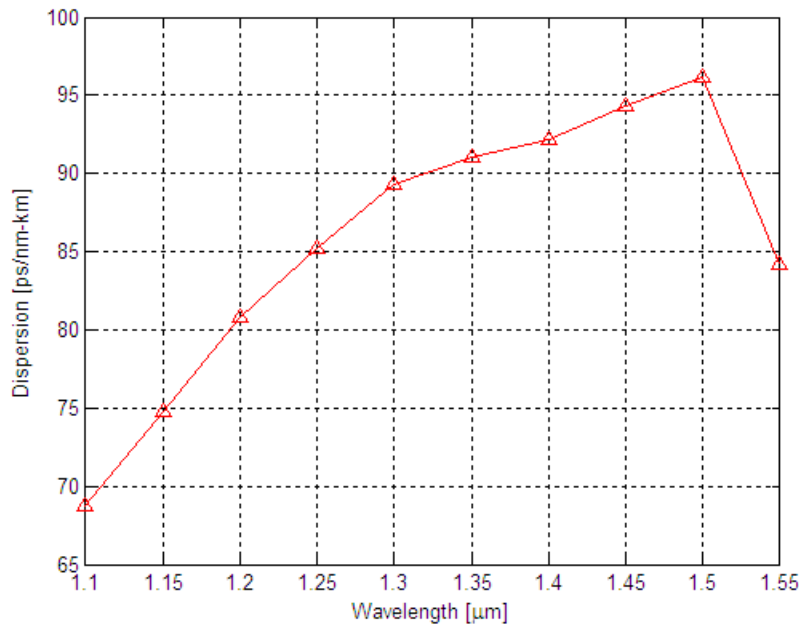
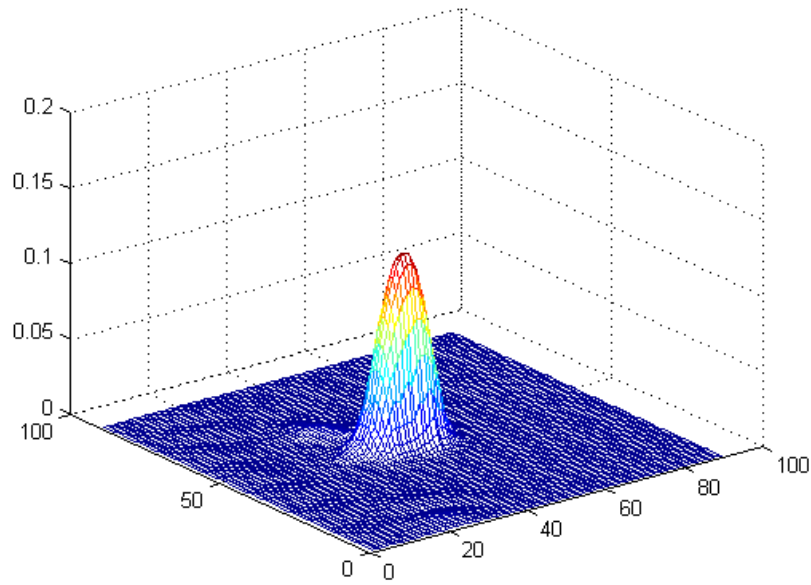


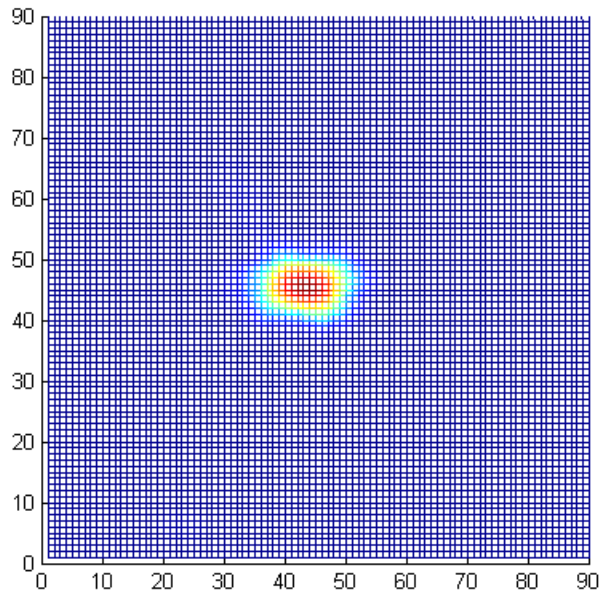
Figure 5.15 Chromatic dispersion versus wavelength of the fundamental mode for a holey fiber with random air-hole distributions of Figure 5.14

Table 5.3 The effective area for a holey fiber with random air-hole distributions, as shown in Figure 5.14

Operating wavelength [μm]	Effective area [μm^2]
0.8	3.6697
1.3	4.1410
1.55	4.4835
2.0	6.3824



(a)



(b)

Figure 5.16 Field distribution for the E_x component of the fundamental mode at $\lambda=1.55 \mu\text{m}$ for a holey fiber with random air-hole distributions of Figure 5.14. (a) 3D view (b) top view

Chapter 6

Measurements of Holey Fibers

Many holey fibers with random air-hole distributions were fabricated in the draw tower facility of the Fiber & Electro-Optic Research Center at Virginia Tech. The inner cladding region of these holey fibers is formed by a compound material that, when drawn into a fiber, will have many elongated air holes. Figure 6.1 shows the SEM (scanning electron micrograph) picture of the cross section of a sample of a fabricated holey fiber after removing the coating. The air holes, which correspond to dark regions, are, in fact, elongated air bubbles because they are not running from one end to the other end of the fiber, but over short distances on the order of several tens of centimeters.

The formation of holes in these holey fibers is unique in that they are formed in-situ, during the fiber fabrication process. First, in the preform preparation stage, a silica dielectric rod with a diameter of about 3 mm and a silica tube with an outer diameter of about 15 mm and an inner diameter of about 10 mm are fused together at one end on a preform lathe. Here, the silica rod is concentrically located inside the silica tube. Then, a dried mixture of GPP (gas producing powder) and pure fused silica powder is inserted to the gap inside the rod and the tube. The GPP is selected in such a way that after the fiber is drawn only pure fused silica would remain. The amount of air holes in drawn fibers can be controlled by the ratio of the GPP and fused silica powder. Finally, a holey fiber is drawn and coated with a polymer material as protective layer.

In this chapter, several measurement results are presented. In section 6.1, the transmission spectrum of a holey fiber that is subjected to pressure is measured and compared with the

spectrum of a conventional step-index multimode fiber under the same load condition. Loss measurement results are addressed in section 6.2. A far-field intensity pattern experiment is explained in section 6.3. Also, a computer-simulation result and its comparison with experimental results are presented in this section.

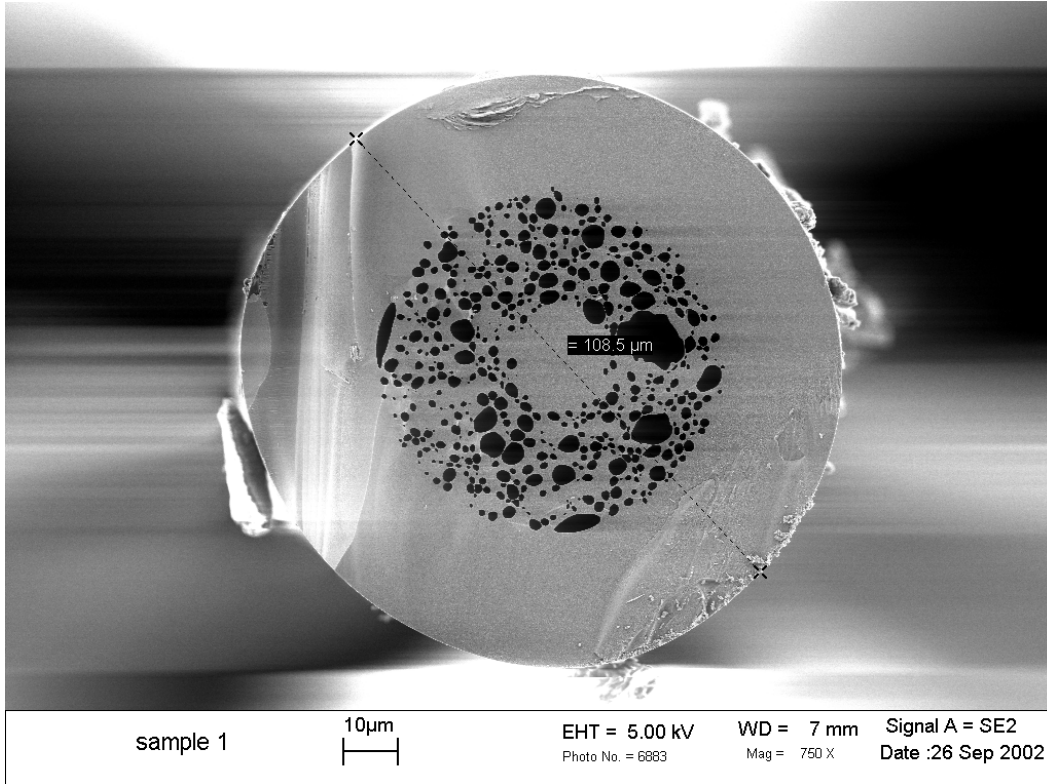


Figure 6.1 The SEM picture of the cross section of a holey fiber with random air-hole distribution

6.1 Transmission Properties

In exploring unique and potentially useful properties of holey fibers that were fabricated, we performed transmission measurements using a white light as input signal and an OSA (optical spectrum analyzer) as detector. The holey fiber is carefully connected to the white light source

and OSA to ensure accuracy of measurements. The blue line in Figure 6.2 illustrates variations of the received power versus wavelength. It is noticed that there are six intensity peaks in the 600-1600 nm wavelength range. These peaks are part of the characteristic of the white light source and are not caused by the holey fiber. The dip around 1350 nm is attributed to the well-known OH absorption.

In a next experiment, we placed an object weighing about 10 Kg on the fiber and measured the transmission spectrum. The red line shows the intensity spectrum of the loaded holey fiber. Again, six peaks are observed as in the first experiment (blue curve). Comparison of the two spectra reveals an interesting feature; namely, that the signal is attenuated under the load condition, with the largest attenuation occurring around 700 nm (by more than 3 dB). This loss is due to the fact that when the fiber is compressed by the object, the signal experiences microbending losses. This phenomenon may be exploited in making pressure sensors with this type of holey fibers.

In order to better appreciate this property of the holey fiber, the same experiment was performed on a conventional multimode fiber. Figure 6.3 shows the transmission spectra for this experiment. In this figure, the blue and red curves correspond to no-load and 10 kg load cases, respectively. The green curve shows the transmission spectrum after removing the 10 Kg load from the fiber for repeatability check. It is noticed that there is a very small intensity change over the entire scanned wavelength range. Also, it is worth noting that there are five intensity peaks instead of six in the 600-1600 nm wavelength range. This is because of the fact that the dip around 1350 nm doesn't happen, as the multimode fiber used in this experiment was deliberately manufactured to minimize the OH absorption. Without this dip, two peaks merge into one and only five peaks are observed.

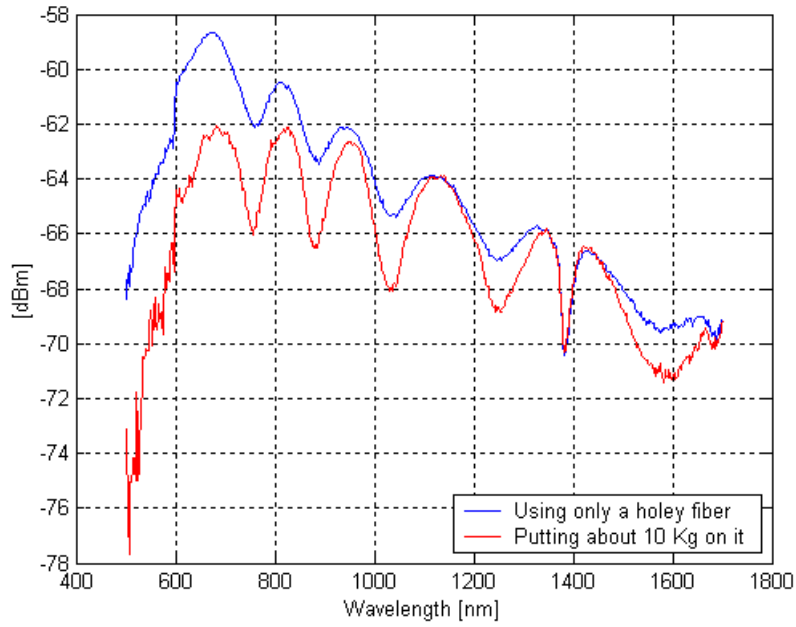


Figure 6.2 Transmission spectra of a holey fiber under no-load and load conditions

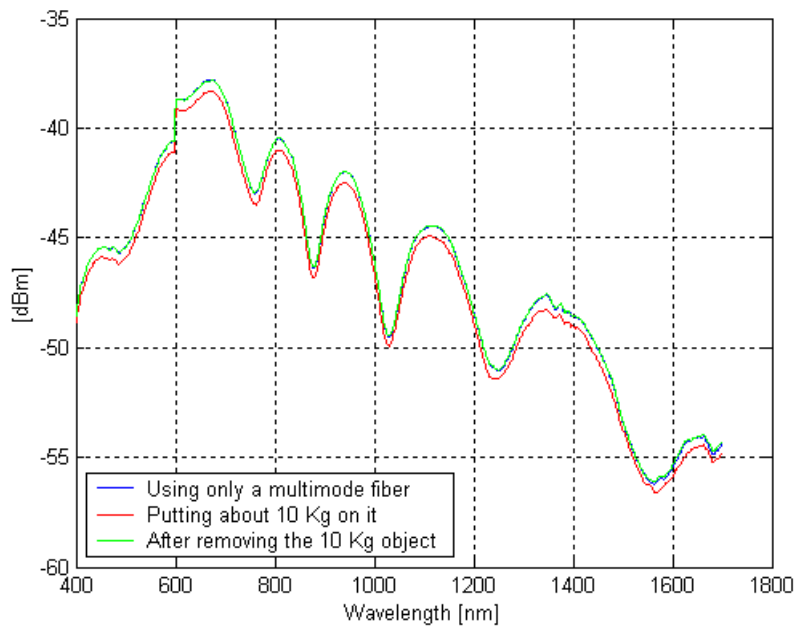


Figure 6.3 Transmission spectra of a conventional multimode fiber under no-load and load conditions

6.2 Loss Measurement

The loss of fabricated holey fibers was measured by the cut-back method. Using the same experiment setup as for the transmission spectra measurement, first the spectrum of the received light was measured for a 3-meter long holey fiber. The bottom curve in Figure 6.4 shows the transmission characteristic obtained from this measurement. Then, we cut out about 1 m from the fiber and performed the same measurement. The second bottom curve shows the results for this measurement. Subtracting the first bottom curve from the second one, the loss for the cut section (1 m) is obtained. The upper curve in Figure 6.4 shows the measured loss of the holey fiber in dB/m. As noted, the loss is about 12 dB/m. This is huge compared with the losses of about 0.2 dB/km for conventional step-index fibers, indicating that the manufacturing process of holey fibers at Virginia Tech facility needs a significant amount of improvement.

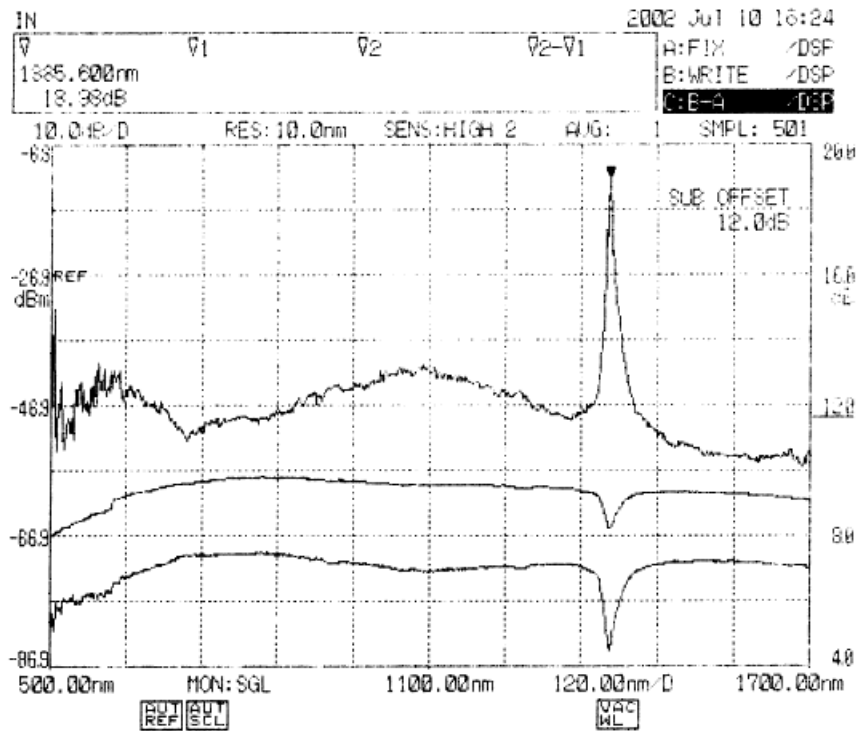


Figure 6.4 Loss spectrum of a holey fiber fabricated in the draw tower facility of Virginia Tech

6.3 Mode Characteristics and Far-Field Measurement

Mode characteristics of the holey fiber that were fabricated are also investigated. Since the holey fiber that is shown in Figure 6.1 has a rather large core region (about 20 μm diameter), it is guiding multimode around the wavelength of 632.8 nm. Even though many recent articles are focusing on the fact that the holey fibers, especially with periodically arranged air holes, are guiding a single mode over a wide wavelength range, this multimode feature of fabricated fibers is desirable for sensor applications because of better coupling efficiency and more sensitivity to external disturbances.

In this section, the mode characteristics of a fabricated holey fiber is analyzed numerically. First, a micrograph of the complicated random-holed optical fiber is taken carefully using a scanning electronic microscope. The digital image of the SEM is mapped into digital data using digital image processing. Based on the digital data, numerical analysis is performed to predict mode characteristics of the random-holed optical fiber. For example in this study, FDTD (finite-difference time-domain) method is utilized to determine whether a holey fiber with random air holes is single-mode or multimode.

From the SEM picture of Figure 6.1, it is noted that the outer diameter of the random-holed optical fiber is 108.5 μm (excluding the coating), which is a little smaller than that (125 μm) of the conventional step-index fiber. The dark regions between the central core and the outer solid cladding are air holes. The size of holes varies from about 2.5 micron radius to about 0.05 micron radius as measured by the SEM. Here, the space where the large and small pores are randomly distributed between the solid central core region and the solid outer tube region is designated as the pore band. Strictly speaking, the holey fiber does not have a clear boundary between the core and cladding regions.

Since the holey fiber in this study is composed of only two different materials (pure silica and air), digital image processing is employed to make a distinction between the two, based on the cross-sectional SEM micrograph. For example, pure silica can be mapped as 1 and air as 0. Once digital data is computed from the digital image, numerical analysis can be applied.

To determine if the holey fiber is single-mode or multi-mode, a compact two-dimensional FDTD analysis of the fiber is carried out. The holey fiber is assumed to be uniform along the z -axis, so that the 2D FDTD method becomes applicable. Since sampled points in a cross section of Figure 6.1 from the SEM micrograph provide refractive index information, the index data at the sampled points are utilized for numerical calculations of allowed modes. First, the continuous electromagnetic field at a distinct point in a given surface lattice is sampled at distinct equally spaced steps in time. Then the finite Fourier transform (FFT) is applied to obtain the mode spectrum as shown in Figure 6.5. Here, the cell size used for the 2D FDTD simulation is $0.302\ \mu\text{m}$ and the total number of cells is 410×410 including 16 perfectly matched layers (PML).

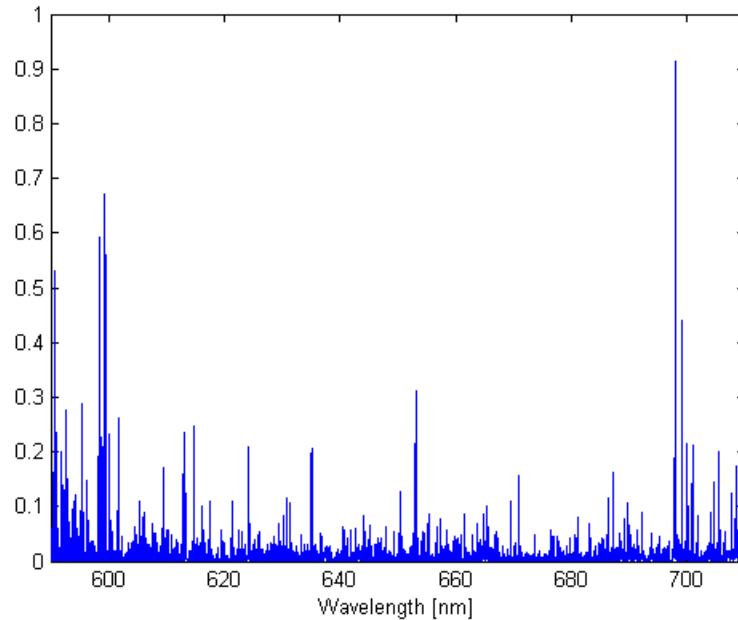


Figure 6.5 Mode spectrum around 632.8-nm wavelength for the holey fiber in Figure 6.1

The FDTD result shown in Figure 6.5 predicts that many modes are generated in the wavelength range between 600 nm and 700 nm. Clearly, the mode spectrum in Figure 6.5 indicates that the holey fiber of Figure 6.1 is multimode at the 632.8-nm wavelength. In order to experimentally verify if the holey optical fiber under investigation actually support a single mode or multiple modes, a far-field measurement was also performed using a He-Ne laser, which is operating at the wavelength of 632.8 nm. An experimental setup around source point is shown in

Figure 6.6. Incident light from the source laser is carefully focused on one end of the holey fiber through a lens and output light from the other end of the fiber is illuminated on a thin white paper [75]. The fiber section tested was about 25 cm long, where most of the random air holes are continuous throughout this length of fiber. While changing the longitudinal path of the fiber a little by pressing or relocating, pictures of the far-field patterns projected on the paper are taken using a CCD (charge-coupled device) camera. Figure 6.7 shows some of the pictures, among which output patterns are observed different. Because the fiber is highly multimode-guiding at 632.8-nm wavelength, interference between propagating modes occurs. As a consequence, lots of speckles are generated as expected from the FDTD simulation result.

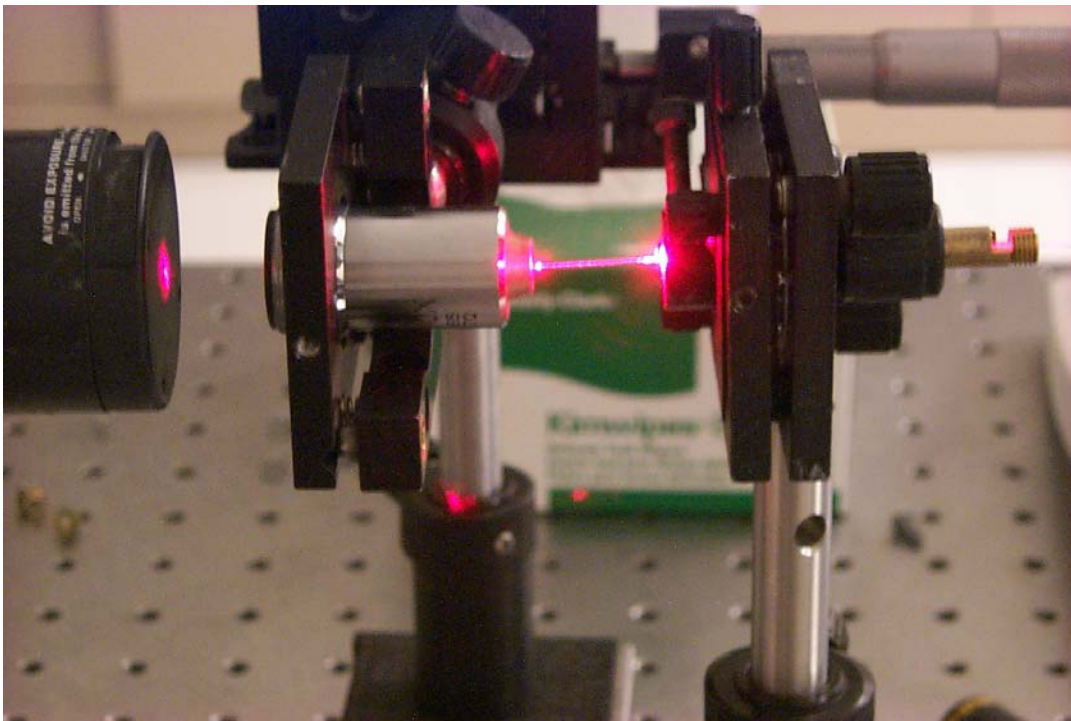


Figure 6.6 Experimental setup around source point for far-field pattern measurement

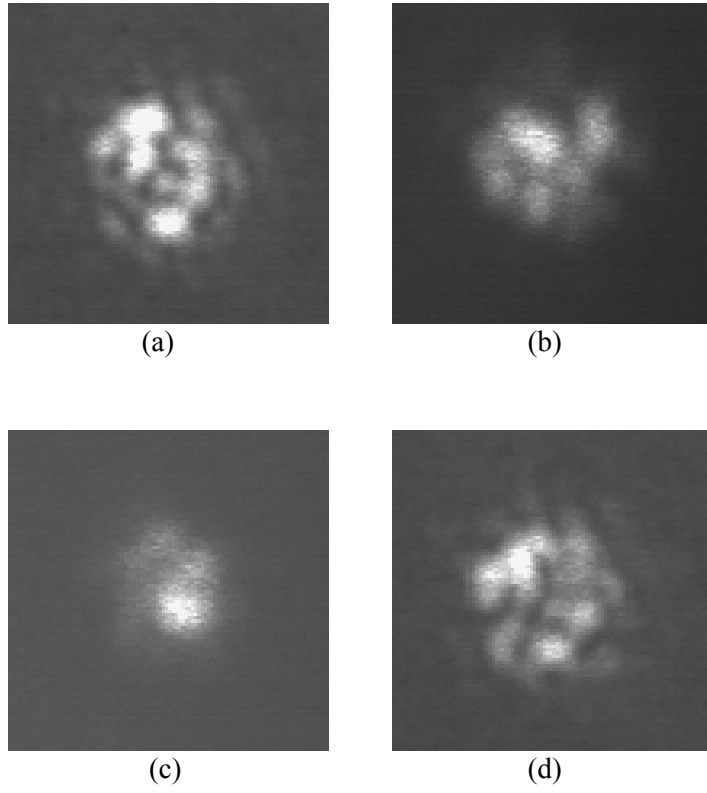


Figure 6.7 Far-field patterns due to interference among propagating modes

Chapter 7

Applications of Holey Fibers

Holey fibers that have been analyzed and designed in this research turn out to provide a single-mode guiding and very small effective area in the wavelength range of 1.3 μm and 1.55 μm for lightwave communications. Because of not only these remarkable properties but also the unique structures of holey fibers, which are quite different from the step-index or graded-index optical fibers, there is on-going investigation to find out applications of this new type of fiber.

Since the holey fibers basically constitute of air holes along the longitudinal direction, optical properties can be controlled rather easily by changing the structural parameters like the pitch length (Λ) and radius (r) of each air hole or the material inside of the small holes. For example, holey fibers incorporating gratings in the core region are designed as lightwave filter in section 7.1. Also, an application of holey fiber as a pressure sensor is addressed in section 7.2.

7.1 Grating-Incorporated Holey Fiber

As the telecommunication traffic increases due to the rapid growth in use of telephone, television, data transmission, and the Internet, the need for communication systems that could handle more and more information increases all over the world. Accordingly, more channels over wider bandwidth are required to fulfill the increased demand. Wavelength division multiplexing (WDM) to process multiple communication channels together in an optical link has been established as a promising solution for increased capacity. The WDM technique allows long-haul

point-to-point lightwave transmission systems to provide 4, 8, or more channels simultaneously in the 1.55- μm wavelength operation.

In a WDM communication system, one of the most essential components is the optical filter. Incorporating Bragg gratings in optical fibers, application-specific optical filters can be designed based on the well-developed grating theory [76]. In a cylindrical dielectric waveguide with an arbitrary cross section but uniform along the z -axis, the power reflection coefficient (R) at the input of a section of the waveguide where the grating is written can be found from the coupled mode theory [77]. Here the coefficient, R , measures how much power of the backward propagating mode is generated by the Bragg grating, compared with the power of the forward propagating mode.

As an example of the cylindrical dielectric waveguide with an arbitrary cross section, a holey fiber is considered in this section. The holey fiber is to be assumed longitudinally invariant and a perturbation of refractive index is introduced in the core region with the following expression,

$$\varepsilon_r + \Delta\varepsilon(z) = \left[n + \delta n_{eff}(z) \right]^2 \approx n^2 + 2n\delta n_{eff}(z) \quad (7-1)$$

Here, the refractive index modulation of the grating is described by

$$\delta n_{eff}(z) = \overline{\delta n_{eff}} \left[1 + \nu \cos\left(\frac{2\pi}{\Omega} z + \phi(z) \right) \right] \quad (7-2)$$

where $\overline{\delta n_{eff}}$ is the refractive index change averaged over a grating period, ν is the fringe visibility of the index change, Ω is the period of the grating perturbation, and $\phi(z)$ is the arbitrary spatially varying phase change to describe grating chirp.

If the grating is assumed uniform along the light propagation direction, $\overline{\delta n_{eff}}$ is a constant and $d\phi/dz = 0$. For a single-mode Bragg reflection grating, a “dc” (period-averaged) coupling coefficient, σ , and an “ac” coupling coefficient, κ , can be found by the following simple relation:

$$\sigma = \frac{2\pi}{\lambda} \overline{\delta n_{eff}} \quad (7-3)$$

$$\kappa = \frac{\pi}{\lambda} v \overline{\delta n_{eff}} \quad (7-4)$$

where σ and κ now become constants for the uniform grating [76].

After applying appropriate boundary conditions, the closed-form solution for the power reflection coefficient, R , of a uniform fiber grating of length L is found to be

$$R = \frac{\sinh^2\left(\sqrt{\kappa^2 - \hat{\sigma}^2} L\right)}{\cosh^2\left(\sqrt{\kappa^2 - \hat{\sigma}^2} L\right) - \frac{\hat{\sigma}^2}{\kappa^2}} \quad (7-5)$$

where $\hat{\sigma}$ is a “dc” self-coupling coefficient defined as

$$\hat{\sigma} \equiv \delta + \sigma \quad (7-6)$$

for the uniform grating. And the detuning term δ , which is independent of z for all grating, is defined as

$$\begin{aligned} \delta &\equiv \beta - \frac{\pi}{\Omega} \\ &= 2\pi n_{eff} \left[\frac{1}{\lambda} - \frac{1}{\lambda_d} \right] \end{aligned} \quad (7-7)$$

where $\lambda_d = 2n_{eff}\Omega$ is the design wavelength for an infinitesimally weak grating of refractive index change ($\delta n_{eff} \rightarrow 0$).

Figure 7.1 shows a schematic that is proposed in this research to realize the grating-incorporated holey fiber. First, the pitch length (Λ) is chosen as 1.0 μm and the radius of the

small holes is $0.4 \mu\text{m}$ with 5 layers in order to accommodate more optical functionality around $1.55\text{-}\mu\text{m}$ wavelength. Moreover, an induced refractive index change $\overline{\delta n_{eff}}$ is 8×10^{-4} , a visibility ν is 0.02, and a uniform grating length L is 70 mm. The small air holes of the fiber can be filled with any materials such as gas, liquid, or solid. Few researches have recently reported on holey fibers that are filled with liquid or solid-like polymers [78]. However, extensive survey reveals that there is no attempt on grating-incorporated holey fibers filled with gas. For the purpose of calculation of the reflectivity, R , of the proposed holey fiber with grating, effective refractive indexes for three different cases are obtained by FDM approach taking into account the material dispersion effect. Figure 7.2 shows variations of normalized propagation constants, when the 5 layers of small holes are filled by air, carbon dioxide (CO_2), or kerosene, which are represented by the red, green, and blue lines, respectively. It is found from a reference that the CO_2 gas has the dielectric constant of 1.6 at 32°F and the kerosene liquid has the dielectric constant of 1.8 at 70°F [79]. These values are used to get the effective refractive indices.

Once the effective refractive indices (1.2457 for air, 1.3339 for CO_2 , and 1.3721 for kerosene) are obtained at the design wavelength of $1.55 \mu\text{m}$, the reflectivity spectrum can be calculated by using (7-5). The reflectivity spectra are plotted in Figure 7.3 for the cases when the 5-layer holes are filled with air (red line), CO_2 (green line), or kerosene (blue line).

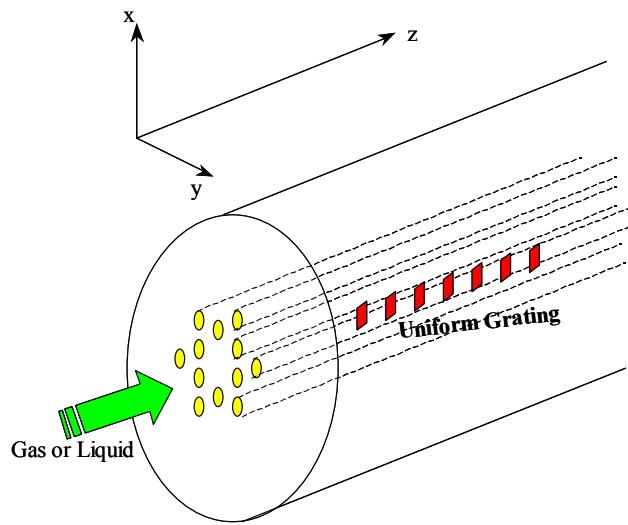


Figure 7.1 A schematic to realize the grating-incorporated holey fiber

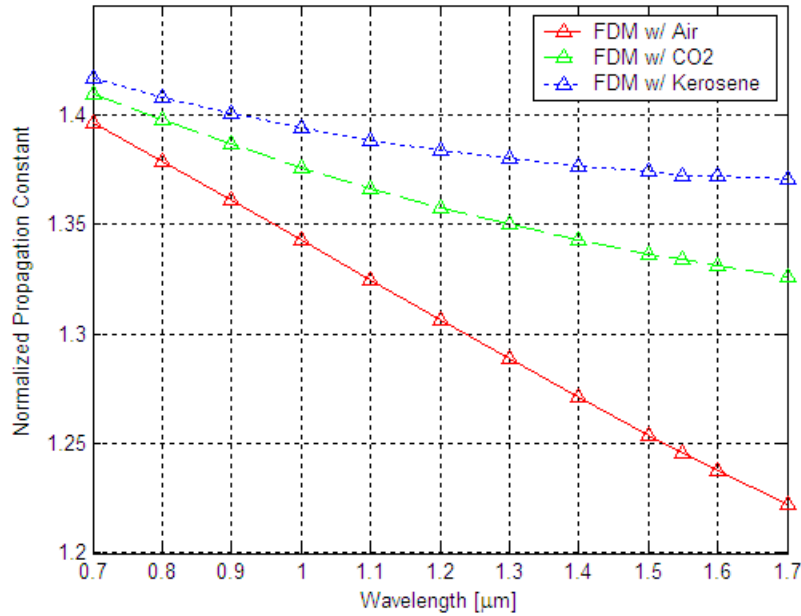


Figure 7.2 Comparison of normalized propagation constants of the fundamental modes, when the 5 layers of small holes are occupied by air, carbon dioxide (CO₂), or kerosene for a holey fiber with $\Lambda = 1.0 \mu\text{m}$ and $d = 0.8 \mu\text{m}$

In more details, the maximum reflectivities are 0.9582075 for air, 0.9582077 for CO₂, and 0.9582055 for kerosene, which are almost the same. The wavelength, λ_{max} , at which maximum reflectivity occurs, is 1.550995 μm for air, 1.550930 μm for CO₂, and 1.550903 μm for kerosene. And each has bandwidth of 4.24 GHz, 3.94 GHz, and 3.87 GHz, respectively, which are quite suitable for a channel allocation in the WDM transmission system. Here, the bandwidth is defined as the width between the first zeros on either side of the maximum reflectivity.

It is noticed that λ_{max} is shifted as the refractive index inside of the small holes is changed. As a result, a tunable optical filter by inserting different gases or liquids can be an application of holey fibers to communications. Also, it is proposed that this grating-incorporated holey fiber can be used as gas or liquid sensor devices.

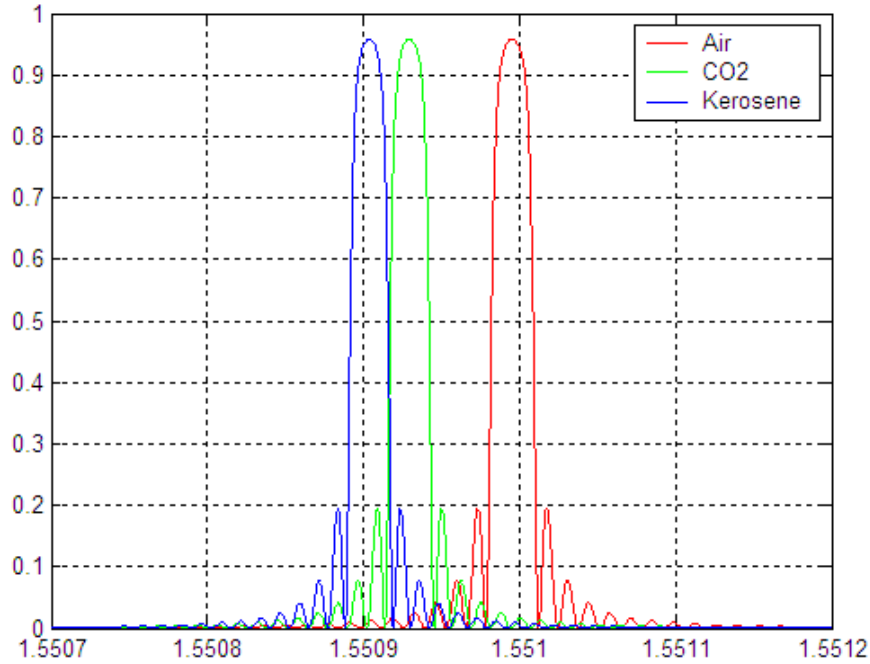


Figure 7.3 Reflectivity spectra for the cases when the 5-layer holes of the holey fiber as in Figure 7.2 are filled with air (red line), CO₂ (green line), or kerosene (blue line)

7.2 Pressure Sensor Applications

As discussed in section 6.1, the holey fiber is sensitive to external pressure. In real situations where optical fibers are used as pressure sensor, it is required that they be sensitive to pressure but be insensitive to other physical quantities such as temperature. If a sensor responds to two parameters like pressure and temperature at the same time, it is difficult to separate the effect of individual parameters.

There are demands for pressure sensors that work in high-temperature environments. For example, in places where oil reservoirs are located far away inside from the earth surface, temperature can reach 200°C or higher. Also, temperatures in gas turbine engine or power generation systems can easily go over 400°C. In these high-temperature harsh environments,

appropriate pressure measurements are required to fit the purposes of applications without the temperature cross sensitivity.

Considering the harsh environment sensing applications, the holey fiber is proposed to be applied as a pressure sensor with temperature insensitivity. The conventional step-index or graded-index fibers have dopants such as germanium in the central core region, which precludes the fiber from high temperature applications by the rapid diffusion of germanium. However, the holey fiber doesn't contain any dopant material as it consists of only pure silica (except for the impurities present), making it suitable for pressure sensing in high-temperature environments. In addition, because the holey fiber has small air holes running inside, force from outside of the fiber will change light propagation. Thus, signal from the output of a holey fiber will be changed. Based on this idea, the holey fiber is tested as an intensity-based pressure sensor as a preliminary work in this research.

As an extension of the measurement work that is presented in section 6.1, another section of the holey fiber about 2-meter long was inserted in a furnace (Thermolyne 47900), which provides temperatures as high as 1000°C. To ensure the heat inside of the furnace reaches the surface of cladding of the holey fiber, a process of burning out the coating was preceded. Then, one end of the holey fiber, after cleaving carefully to get a clean and flat end face, is connected to a white light source (MI-150) with 150W EKE quartz halogen lamp. And the other end is connected to an optical spectrum analyzer (OSA).

Figure 7.4 shows spectrum over the wavelength range between 400 nm and 1700 nm at different temperatures up to 1000°C. First, temperature starts from 23°C (room temperature). The blue line represents the light signal spectrum at one end. The green line represents the spectrum at 400°C. And the red line does at 1000°C. Then, the furnace was cooled down. Of this half cycle, the spectrum at 600°C is scanned, which is plotted as the yellow line. Finally, the dark line represents the spectrum at 32°C after one cycle of temperature change. Here, it is noticed that there is almost no dependency of the holey fiber on the temperature variation up to 1000°C – less than 0.3-dBm variations in the wavelength range between 600 nm and 1500 nm. This might go to even higher temperature, even though this was not tested because of the furnace limitation.

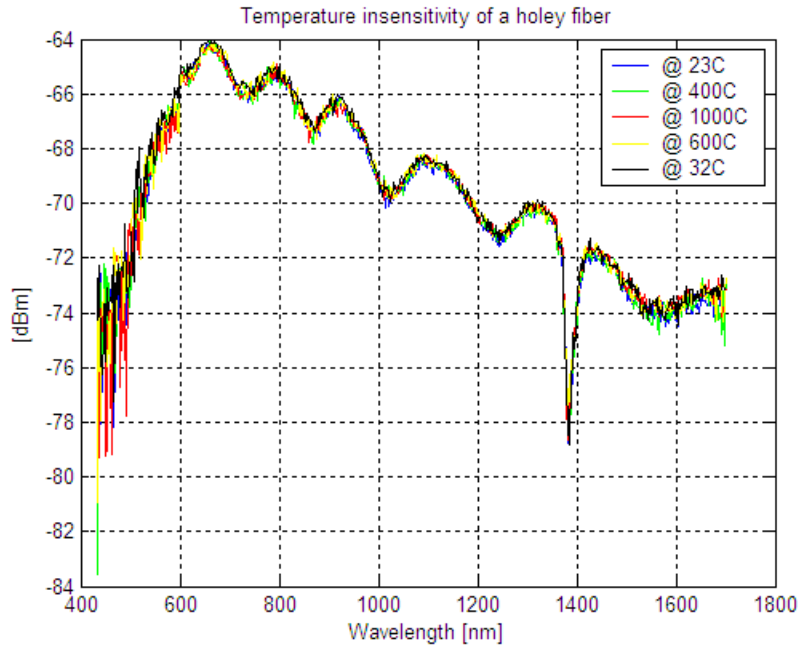
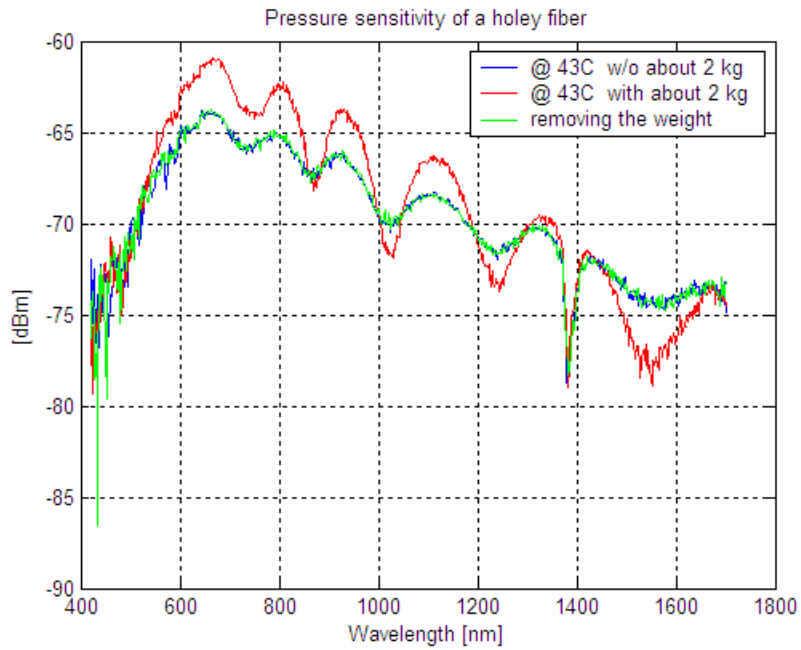


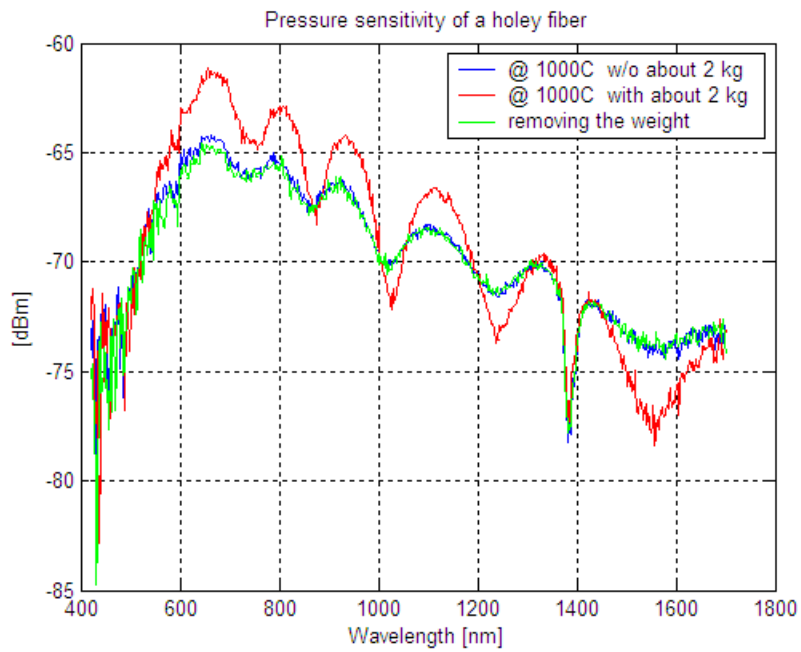
Figure 7.4 Temperature insensitivity of a holey fiber over the wavelength range between 400 nm and 1700 nm

To ensure that this holey fiber with temperature insensitivity has pressure sensitivity, about 2-kg weight was put on some part of the holey fiber outside the furnace. At 43°C, Figure 7.5 (a) shows how well the fiber responds to pressure. The blue line represents output spectrum when no weight is put on the fiber. And the red line represents output spectrum when the 2-kg weight is put on the fiber. About 3-dB difference is noticed at 670-nm wavelength. Then, the output spectrum, after the weight is removed, is scanned as the green line. Clearly, it is shown that the fiber does not have any hysteresis in this test. The same experiment is repeated after increasing the furnace temperature to 1000°C. And about the same performance – about 3-dB difference at 670-nm wavelength and no hysteresis is observed as shown in Figure 7.5 (b).

One thing we can notice here is that the intensity, when a weight is on a section of a holey, is increased, which is different from the result in Figure 6.2. The reason is that the section used here is different from the one tested in section 6.1. Due to the structural difference, the intensity response is different. This is also observed in the next isostatic pressure test in which another different section of a holey fiber is utilized.



(a)



(b)

Figure 7.5 Pressure sensitivity of a holey fiber over the wavelength range between 400 nm and 1700 nm at (a) 43°C and (b) 1000°C

Another test that has been performed on the holey fiber is the isostatic pressure test. In the previous two tests in sections 6.1 and 7.2, weights are put on parts of the holey fiber. As a result, force from the weights cannot be distributed uniformly to the parts of the holey fiber. Thus, it is difficult to predict that how much force is actually affected on the holey fiber. This leads to carry out the isostatic pressure test. Test setup is illustrated in Figure 7.6. First, a part of the holey fiber is inserted into a metal tube and epoxy-cured at both ends of the metal tube. After the preparation, this metal tube is connected to APP (automated pressure processor) machine, which provides the isostatic pressure on the part of the holey fiber inside of the metal tube. A PC that is connected to the APP machine controls the isostatic pressure.

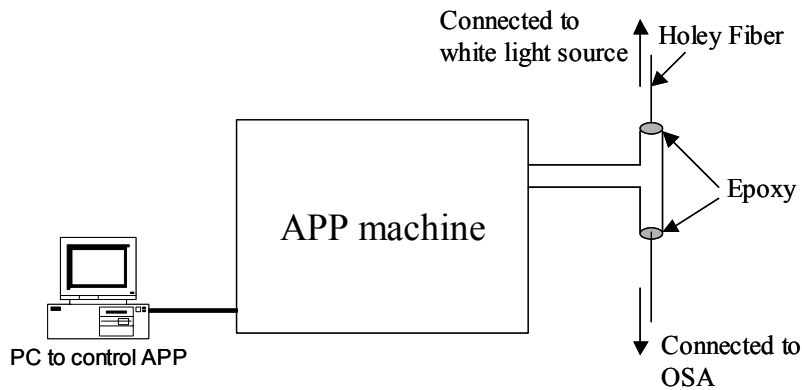
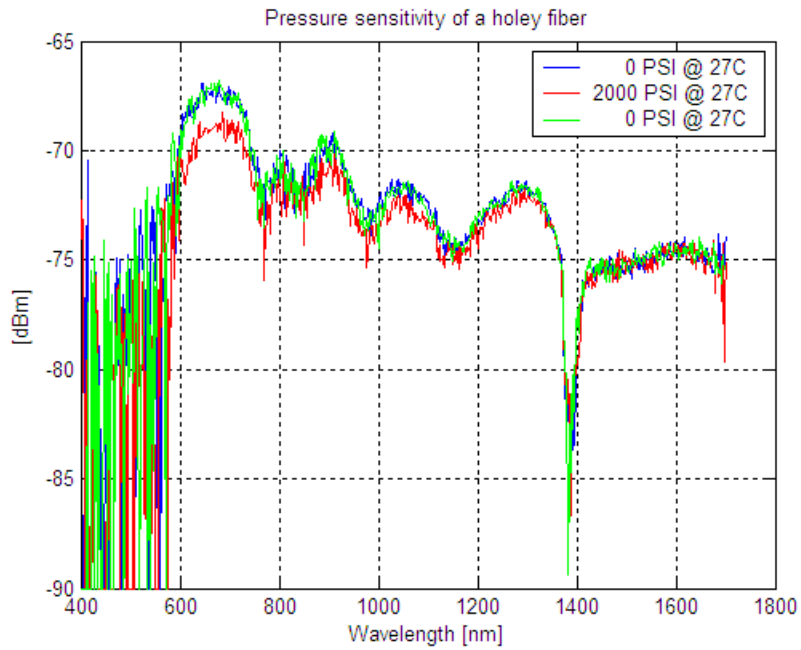
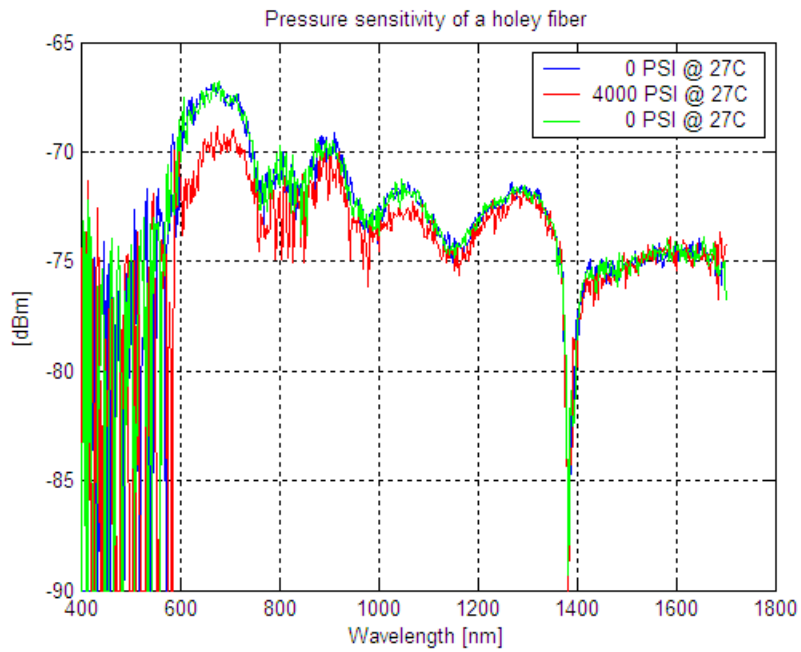


Figure 7.6 Setup schematic for isostatic pressure test

Figure 7.7 (a) shows how well the fiber responds to the isostatic pressure when 2000 PSI (Pounds per Square Inch) is applied by the APP machine at room temperature. The blue line represents output spectrum when zero PSI is applied on the fiber. And the red line represents output spectrum when 2000 PSI is applied. Here, about 2-dB difference is noticed at 670-nm wavelength. Then, the output spectrum, after the isostatic pressure is removed, is scanned as the green line. Again, it is clearly shown that the fiber does not have any hysteresis in this test. The same experiment is repeated after increasing the isostatic pressure to 4000 PSI. And about the same performance – about 2.5-dB difference at 670-nm wavelength and no hysteresis is observed as shown in Figure 7.7 (b). It should be mentioned that this time, the intensity of the source signal is lower. Thus the intensity of the output signal is lower and more noise is involved.



(a)



(b)

Figure 7.7 Isostatic pressure sensitivity of a holey fiber over the wavelength range between 400 nm and 1700 nm by forcing (a) 2000 PSI and (b) 4000 PSI at room temperature

Chapter 8

Conclusions and Recommendations for Future Work

Towards exploring new types of optical fibers, with the aim of improving the performance and reducing the cost for applications in communication systems, sensor devices, medical instrumentation, and many kinds of optical components, the analysis and design of photonic crystal and microstructure optical fibers have been undertaken in this dissertation. In particular, two types of such fibers have been investigated: (i) one-dimensional (1D) cylindrical photonic crystal waveguides, and (ii) two-dimensional (2D) photonic crystal and microstructure fibers.

Measurements of holey fibers with random air holes, which were fabricated in the draw tower facility at Virginia Tech, have also been performed, opening the possibility of applications to pressure sensing. Grating-incorporated holey fibers were investigated, with potential applications in both sensor devices and fiber-optic communication systems. The important results and conclusions of this research work are summarized in section 8.1, and recommendations for future work are presented in section 8.2.

8.1 Conclusions

First, one-dimensional cylindrical photonic crystal waveguides were analyzed using a systematic 4×4 matrix approach based on vector field analytical solutions. As an example case with desirable transmission properties, a 1D photonic crystal fiber with dimensions $r_1 = 1.0 \mu\text{m}$,

$d_a = 0.2 \mu\text{m}$, and $d_g = 0.3 \mu\text{m}$ has been considered. It was found that once the number of cladding layers is large enough, adding more cladding layers does not affect the propagation properties significantly. This is due to the fact that fields decay exponentially in the cladding layers, and the layers beyond which fields become sufficiently small have little influence on propagation properties. This convergence behavior for the second and higher-order modes occurred more slowly for the same number of layers. This example 1D photonic crystal waveguide provides a chromatic dispersion of $-3.8248 \text{ ps/nm}\cdot\text{km}$ at $1.55 \mu\text{m}$ and very small effective areas ($2 - 4 \mu\text{m}^2$). The low-index core PCFs provided somewhat larger effective areas ($3 - 5.5 \mu\text{m}^2$).

This study was extended to microstructure optical fibers with 1D random cladding index distributions. Comparison of results for the average values of normalized propagation constant, chromatic dispersion, and effective area with the corresponding results for the reference fibers indicates that they are generally in good agreement. It was noted that this agreement becomes better as the thickness of glass/air becomes smaller. The effective area in all fibers examined is very small ($2 - 3 \mu\text{m}^2$), indicating that these microstructure optical fibers are well suited for nonlinear optical devices. Results for a 1D microstructure optical fiber with $d_a = d_g = 0.1 \mu\text{m}$ and 32 layers show percentage differences less than 5 % between the average and reference values of dispersion and effective area at $1.3 \mu\text{m}$ and $1.55 \mu\text{m}$ wavelengths.

The second of the work involved analysis and design of 2D holey fibers. To examine the propagation properties of holey fibers, the numerical techniques, FDTD method and FDM, were employed. The FDTD method allows reliable calculation of the normalized propagation constant, while the FDM can be used to efficiently compute field distributions. The FDM can also be used to calculate the propagation constant. But verifications of the results are required, because many spurious modes are generated in the FDM approach. It was noted that increasing the number of layers of small air holes beyond a certain point (at least 3 layers) does not affect the propagation properties significantly, which means that the layers close to the center of the holey fiber play a more significant role on its performance. The field distribution of the fundamental mode is nearly Gaussian in shape at shorter wavelengths.

The single-mode guiding property was also sought for the holey fibers with random air-hole distributions. This was achieved by increasing the number of small air holes with random sizes

and reducing the size of the core region. In doing so, it was found that a holey fiber with 1.0- μm radius for the core region and 200 random air holes supports a single mode over the wavelength range from 1.1 μm to 1.55 μm . Weak ripples in the field magnitude around the core were observed and the effective areas ranging from 4 to 5 μm^2 over the above wavelength range were obtained.

To determine if fabricated holey fibers are guiding a single mode or multiple modes, refractive-index information were obtained from the SEM micrograph for each fiber cross section. Then, the index data at the sampled points were utilized for numerical calculations of allowed modes in the given waveguide. The FDTD method of analysis predicts many modes are generated over the wavelength range between 600 nm and 700 nm. This mode spectrum indicates that the holey fibers are multimode at the 632.8 nm wavelength. Far-field measurements, using a He-Ne laser with the operation wavelength of 632.8 nm, were also conducted. The measured results show that many speckles, generated due to interference between multi-propagating modes, exist.

As an initial attempt to see if the holey fiber can be used as a pressure sensor, about 2-kg weight was put on some part of the holey fiber, while another part of the fiber was heated in a furnace. A drop of about 3-dB in the transmitted power level was observed at 670-nm wavelength. No hysteresis were observed and the power level did not change when the temperature varied from 43°C and 1000°C. For more precise measurements, an APP machine was used at room temperature. When 2000 PSI was applied, about 2-dB drop in power level was noticed at 670-nm wavelength. After increasing the isostatic pressure to 4000 PSI, the power drop reached to about 2.5-dB at the same wavelength.

As another application of the holey fiber, uniform grating for a holey fiber with $\Lambda = 1.0 \mu\text{m}$ and $d = 0.8 \mu\text{m}$ was incorporated and analyzed. When the grating-incorporated holey fiber was filled with three different materials (air, CO_2 , or kerosene), it was noticed that λ_{max} is shifted. As a result, tunable optical filters can be realized by filling grating-incorporated holey fibers with different gases or liquids. Also, such holey fiber can be utilized as gas or liquid sensor devices.

8.2 Recommendations for Future Work

For 1D cylindrical photonic crystal waveguides, the investigation might be extended to find equivalent step-index fiber models for simpler and faster analysis and design work. With the core radius (r_1) the same, the alternating-index cladding could be replaced by an equivalent cladding with a constant index, n_{eq} , making this new equivalent model behave like a step-index fiber. The equivalent cladding index is obviously a function of wavelength and parameters of the periodic cladding.

For the 2D microstructure optical fibers with random air-hole distributions, comparison of average values of propagation properties with those of the corresponding reference fiber with periodic hole arrangements is useful. This analysis, although intensely time-consuming, is straightforward.

For the pressure sensor development, more tests and measurements are required. Such effort will lead to more reliable and improved optical fiber sensors. The prospects for commercialization of such sensors in high temperature environments appear to be good.

References

- [1] E. Yablonovitch, "Inhibited spontaneous emission in solid state physics and electronics," *Phys. Rev. Lett.*, Vol. 58, pp. 2059-2062, 1987
- [2] M. M. Sigalas, R. Biswas, Q. Li, D. Crouch, W. Leung, R. Jacobs-Woodbury, B. Laogh, S. Nielsen, S. McCalmont, G. Tuttle, K. M. Ho, "Dipole antennas on photonic band-gap crystals—experiment and simulation," *Microwave Opt. Tech. Lett.*, Vol. 15, pp. 153-158, 1997
- [3] G. P. Gauthier, A. Courtay, and G. M. Rebeiz, "Microstrip antennas on synthesized low dielectric-constant substrates," *IEEE Trans. Antennas Propag.*, Vol. 45, pp. 1310-1314, 1997
- [4] J. G. Maloney, M. P. Kesler, B. L. Shirley, and G. S. Smith, "A simple description for waveguiding in photonic bandgap materials," *Microwave Opt. Tech. Lett.*, Vol. 14, pp. 261-265, 1997
- [5] <http://www.elec.gla.ac.uk/~areynolds/>
- [6] D. N. Chigrin, A. V. Lavrinenko, D. A. Yarotsky, S. V. Gaponenko, "All-dielectric one-dimensional periodic structures for total omnidirectional reflection and partial spontaneous emission control," *J. of Lightwave Technology*, Vol. 17, pp.2018-2024, Nov. 1999
- [7] J. D. Joannopoulos, R. D. Meade, and J. N. Winn, *Photonic Crystals: Molding the flow of light*, Princeton University Press, 1995
- [8] T. A. Birks, J. C. Knight, and P. St. J. Russell, "Endlessly single-mode photonic crystal fiber," *Optics Letters*, Vol. 22, pp. 961-963, July 1997

- [9] D. Mogilevtsev, T. A. Birks, and P. St. J. Russell, "Group-velocity dispersion in photonic crystal fibers," *Optics Letters*, Vol. 23, pp. 1662-1664, Nov. 1998
- [10] B. J. Mangan, J. C. Knight, T. A. Birks, and P. St. J. Russell, "Dual-core photonic crystal fibre," *CLEO '99, JFB8*, pp. 559-560, 1999
- [11] A. Ferrando, E. Silvestre, J. J. Miret, P. Andrés, M. V. Andrés, "Full-vector analysis of a realistic photonic crystal fiber," *Optics Letters*, Vol. 24, pp. 276-278, Mar. 1999
- [12] A. Ferrando, E. Silvestre, J. J. Miret, and P. Andrés, "Nearly zero ultraflattened dispersion in photonic crystal fibers," *Optics Letters*, Vol. 25, pp. 790-792, June 2000
- [13] T. M. Monro, D. J. Richardson, N. G. R. Broderick, and P. J. Bennett, "Holey optical fibers: an efficient modal model," *Journal of Lightwave Technology*, Vol. 17, pp. 1093-1102, June 1999
- [14] T. M. Monro, P. J. Bennett, N. G. R. Broderick, and D. J. Richardson, "Holey fibers with random cladding distributions," *Optics Letters*, Vol. 25, pp. 206-208, Feb. 2000
- [15] J. Broeng, S. E. Barkou, A. Bjarklev, T. Sondergaard, and E. Knudsen, "Review paper: Crystal fibre technology," *DOPS-NYT*, pp. 22-28, 2000
- [16] T. P. Hansen, J. Broeng, S. E. B. Libori, E. Knudsen, A. Bjarklev, J. R. Jensen, H. Simonsen, "Highly birefringent index-guiding photonic crystal fibers," *IEEE Photonics Technology Letters*, Vol. 13, pp. 588-590, June 2001
- [17] A. Bjarklev, J. Broeng, S. E. B. Libori, E. Knudsen, and H. R. Simonsen, "Photonic crystal fiber modeling and applications," *OFC conference*, TuC1-1, Mar. 2001
- [18] M. J. Steel and R. M. Osgood, Jr., "Elliptical-hole photonic crystal fibers," *Optics Letters*, Vol. 26, pp. 229-231, Feb. 2001
- [19] J. K. Ranka, R. S. Windeler, and A. J. Stentz, "Optical properties of high-delta air-silica microstructure optical fibers," *Optics Letters*, Vol. 25, pp. 796-798, June 2000

- [20] T. P. White, B. T. Kuhlmeiy, R. C. McPhedran, D. Maystre, G. Renversez, C. Martijn de Sterke, L. C. Botten, "Multipole method for microstructured optical fibers," *Journal of Opt. Soc. Am. B*, Vol. 19, pp. 2322-2340, Oct. 2002
- [21] J. M. Fini, "Analysis of microstructure optical fibers by radial scattering decomposition," *Optics Letters*, Vol. 28, pp. 992-994, June 2003
- [22] B. T. Kuhlmeiy, R. C. McPhedran, and C. M. de Sterke, "Modal cutoff in microstructured optical fibers," *Optics Letters*, Vol. 27, pp. 1684-1686, Oct. 2002
- [23] J. Lægsgaard, A. Bjarklev, and S. E. B. Libori, "Chromatic dispersion in photonic crystal fibers: fast and accurate scheme for calculation," *Journal of Opt. Soc. Am. B*, Vol. 20, pp. 443-448, Mar. 2003
- [24] J. Kim, U. -C. Paek, D. Y. Kim and Y. Chung, "Analysis of the dispersion properties of holey optical fibers using normalized dispersion," OFC conference, WDD86-1, Mar. 2001
- [25] L. P. Shen, W. -P. Huang, G. X. Chen, S. S. Jian, "Design and optimization of photonic crystal fibers for broad-band dispersion compensation," *IEEE Photonics Technology Letters*, Vol. 15, pp. 540-542, Apr. 2003
- [26] N. Guan, S. Habu, K. Himeno, A. Wada, "Characteristics of field confined holey fiber analyzed by boundary element method," OFC conference, ThS5, Mar. 2002
- [27] A. Cucinotta, S. Selleri, L. Vincetti and M. Zoboli, "Photonic crystal fibers: perturbation analysis of polarization and dispersion properties," OFC conference, ThS2, Mar. 2002
- [28] J. C. Knight, T. A. Birks, P. St. J. Russell, and D. M. Atkin, "All-silica single-mode optical fiber with photonic crystal cladding," *Optics Letters*, Vol. 21, pp. 1547-1549, Oct. 1996
- [29] P. St. J. Russell, J. C. Knight, T. A. Birks, R. F. Cregan, B. J. Mangan, and J. -P. De Sandro, "Photonic crystal fibres," *ECOC 97*, pp. 63-64, Sep. 1997

- [30] J. C. Knight, T. A. Birks, P. St. J. Russell, and J. G. Rarity, "Bragg scattering from an obliquely illuminated photonic crystal fiber," *Applied Optics*, Vol. 37, pp. 449-452, Jan. 1998
- [31] Y. Fink, D. J. Ripin, S. Fan, C. Chen, J. D. Joannopoulos, E. L. Thomas, "Guiding optical light in air using an all-dielectric structure," *Journal of Lightwave Technology*, Vol. 17, pp. 2039-2041, Nov. 1999
- [32] B. J. Mangan, J. C. Knight, T. A. Birks, P. S. J. Russell, A. H. Greenaway, "Experimental study of dual-core photonic crystal fibre," *Electronics Letters*, Vol. 36, pp. 1358-1359, Aug. 2000
- [33] J. K. Ranka, R. S. Windeler, and A. J. Stentz, "Visible continuum generation in air-silica microstructure optical fibers with anomalous dispersion at 800 nm," *Optics Letters*, Vol. 25, pp. 25-27, Jan. 2000
- [34] J. C. Knight, J. Arriaga, T. A. Birks, A. Ortigosa-Blanch, W. J. Wadsworth, P. St. J. Russell, "Anomalous dispersion in photonic crystal fiber," *IEEE Photonics Technology Letters*, Vol. 12, pp. 807-809, July 2000
- [35] D. Gerard, L. Berguiga, F. de Fornel, L. Salomon, C. Seassal, X. Letartre, P. Rojo-Romeo, P. Viktorovitch, "Near-field probing of active photonic-crystal structures," *Optics Letters*, Vol. 27, pp. 173-175, Feb. 2002
- [36] K. Tajima, K. Nakajima, K. Kurokawa, N. Yoshizawa, and M. Ohashi, "Low-loss photonic crystal fibers," *OFC conference*, ThS3, Mar. 2002
- [37] K. Tajima, J. Zhou, K. Nakajima, and K. Sato, "Ultra low loss and long length photonic crystal fiber," *OFC conference*, PD1-1, Mar. 2003
- [38] B. Zsigri, C. Peucheret, M. D. Nielsen, P. Jeppesen, "Transmission over 5.6 km large effective area and low-loss (1.7 dB/km) photonic crystal fibre," *Electronics Letters*, Vol. 39, pp. 796-797, May. 2003

- [39] P. St. J. Russell, J. C. Knight, T. A. Birks, B. J. Mangan and W. J. Wadsworth, "Recent progress in photonic crystal fibres," OFC conference, ThG1-1, Mar. 2000
- [40] W. J. Wadsworth, A. Ortigosa-Blanch, J. C. Knight, T. A. Birks, T.-P. M. Man, P. St. J. Russell, "Supercontinuum generation in photonic crystal fibers and optical fiber tapers: a novel light source," *Journal of Opt. Soc. Am. B*, Vol. 19, pp. 2148-2155, Sep. 2002
- [41] S. Coen, A. H. L. Chau, "White-light supercontinuum generation with 60-ps pump pulses in a photonic crystal fiber," *Optics Letters*, Vol. 26, pp. 1356-1358, Sep. 2001
- [42] Y. Wang, Y. Zhao, J. S. Nelson, Z. Chen, R. S. Windeler, "Ultrahigh-resolution optical coherence tomography by broadband continuum generation from a photonic crystal fiber," *Optics Letters*, Vol. 28, pp. 182-184, Feb. 2003
- [43] P. Petropoulos, T. M. Monro, H. Ebendorff-Heidepriem, K. Frampton, R. C. Moore, H. N. Rutt, D. J. Richardson, "Soliton-self-frequency-shift effects and pulse compression in an anomalously dispersive high nonlinearity lead silicate holey fiber," OFC conference, PD3-1, Mar. 2003
- [44] P. Petropoulos, T. M. Monro, W. Belardi, K. Furusawa, J. H. Lee, D. J. Richardson, "2R-regenerative all-optical switch based on a highly nonlinear holey fiber," *Optics Letters*, Vol. 26, pp. 1233-1235, Aug. 2001
- [45] N. Nishizawa, Y. Ito, and T. Goto, "0.78–0.90- μm wavelength-tunable femtosecond soliton pulse generation using photonic crystal fiber," *IEEE Photonics Technology Letters*, Vol. 14, pp. 986-988, July 2002
- [46] D. G. Ouzounov, K. D. Moll, M. A. Foster, W. R. Zipfel, W. W. Webb, A. L. Gaeta, "Delivery of nanojoule femtosecond pulses through large-core microstructured fibers," *Optics Letters*, Vol. 27, pp. 1513-1515, Sep. 2002

- [47] C. Kerbage, P. Steinvurzel, P. Reyes, P. S. Westbrook, R. S. Windeler, A. Hale, B. J. Eggleton, "Highly tunable birefringent microstructured optical fiber," *Optics Letters*, Vol. 27, pp. 842-844, May 2002
- [48] G. Kakarantzas, T. A. Birks, and P. St. J. Russell., "Structural long-period gratings in photonic crystal fibers," *Optics Letters*, Vol. 27, pp. 1013-1015, June 2002
- [49] C. Kerbage, R. S. Windeler, B. J. Eggleton, P. Mach, M. Dolinski, and J. A. Rogers, "Electrically driven motion of micro-fluids in air-silica microstructure fiber: application to tunable filter/attenuator," OFC conference, ThK1, Mar. 2002
- [50] C. Kerbage, J. Ging, P. Steinvurzel, A. Hale, A. Yablon, R. S. Windeler, and B. J. Eggleton, "Air-silica microstructure fiber based variable optical attenuator device," OFC conference, ThK4, Mar. 2002
- [51] Y. C. Youk, U. C. Paek, D. Y. Kim, K. W. Park, "Fabrication of a tapered holey optical fiber and its guiding properties," OFC conference, ThGG14, Mar. 2002
- [52] G. E. Town and J. T. Lizier, "Tapered holey fibers for spot-size and numerical-aperture conversion," *Optics Letters*, Vol. 26, pp. 1042-1044, July 2001
- [53] K. G. Hougaard, J. Broeng, and A. Bjarklev, "Low pump power photonic crystal fibre amplifiers," *Electronics Letters*, Vol. 39, pp. 599-600, Apr. 2003
- [54] P. -T. Lee, J. R. Cao, S. -J. Choi; Z. -J. Wei; J. D. O'Brien, P. D. Dapkus, "Room-temperature operation of VCSEL-pumped photonic crystal lasers," *IEEE Photonics Technology Letters*, Vol. 14, pp. 435-437, Apr. 2002
- [55] F. Villa, L. E. Regalado, F. Ramos-Mendieta, J. Gaspar-Armenta, T. Lopez-Ros, "Photonic crystal sensor based on surface waves for thin-film characterization," *Optics Letters*, Vol. 27, pp. 646-648, Apr. 2002
- [56] G. Keiser, *Optical Fiber Communications*, McGraw Hill, 3rd Ed., 2000

- [57] A. Safaai-Jazi and L. J. Lu, "Accuracy of approximate methods for the evaluation of chromatic dispersion in dispersion-flattened fibers," *Journal of Lightwave Technology*, Vol. 8, pp. 1145-1150, Aug. 1990
- [58] H. T. Hattori and A. Safaai-Jazi, "Fiber designs with significantly reduced nonlinearity for very long distance transmission," *Applied Optics*, Vol. 37, pp. 3190-3197, May 1998
- [59] M. J. Adams, *An introduction to optical waveguides*, Wiley, 1981
- [60] P. Petropoulos, T. M. Monro, W. Belardi, K. Furusawa, J. H. Lee and D. J. Richardson, "A highly nonlinear holey fiber and its application in a regenerative optical switch," OFC conference, TuC3-1, Mar. 2001
- [61] K. S. Yee, "Numerical solution of initial boundary value problems involving Maxwell's equations in isotropic media," *IEEE Trans. Antennas and Propagation*, Vol. 14, pp. 302-307, May 1966
- [62] A. Taflove and S. C. Hagness, *Computational Electromagnetics: the finite-difference time-domain method*, 2nd Ed., Artech House, 2000
- [63] K. S. Kunz and R. J. Luebbers, *The finite difference time domain method for electromagnetics*, Boca Raton : CRC Press, 1993
- [64] S. M. Rao, *Time Domain Electromagnetics*, Academic Press, 1998
- [65] J. Berenger, "A perfectly matched layer for the absorption of electromagnetic waves," *Journal of Computational Physics*, Vol. 114, pp. 185-200, 1994
- [66] D. M. Sullivan, "An unsplit step 3-D PML for use with the FDTD method," *IEEE Microwave and guided wave letters*, Vol. 7, pp. 184-186, July 1997

- [67] A. Taflove and M. E. Brodwin, "Numerical solution of steady-state electromagnetic scattering problems using the time-dependant Maxwell's equations," IEEE Trans. Microwave Theory Tech., MTT-23, pp. 623-630, Aug. 1975
- [68] A. Thom and C. J. Apelt, *Field Computations in Engineering and Physics*, London, 1961
- [69] W. P. Huang, C. L. Xu, and S. K. Chaudhuri, "A finite-difference vector beam propagation method for three-dimensional waveguide structures," IEEE Photonics Technology Letters, Vol. 4, pp. 148-151, Feb. 1992
- [70] W. P. Huang, C. L. Xu, and S. K. Chaudhuri, "A vector beam propagation method based on H fields," IEEE Photonics Technology Letters, Vol. 3, pp. 1117-1120, Dec. 1991
- [71] E. Schweig, "Computer analysis of dielectric waveguides: A finite-difference method," IEEE Trans. on Microwave Theory and Tech., Vol. MTT-32, pp. 531-541, May 1984
- [72] D. Gloge, "Weakly guiding fibers," Appl. Opt., Vol. 10, pp. 2252-2258, Oct. 1971
- [73] A. Bjarklev, J. Broeng, S. E. B. Libori, E. Knudsen, and H. R. Simonsen, "Photonic crystal fiber modeling and applications," OFC conference, TuC1-1, Mar. 2001
- [74] G. P. Agrawal, *Nonlinear Fiber Optics*, Academic Press, 2nd Ed., 1995
- [75] A. Kumer, N. K. Goel, and R. K. Varshney, "Studies on a few-mode fiber-optic strain sensor based on LP01-LP02 mode interference," Journal of Lightwave Technology, Vol. 19, pp. 358-362, Mar. 2001
- [76] T. Erdogan, "Fiber grating spectra," Journal of Lightwave Technology, Vol. 15, pp. 1277-1294, Aug. 1997
- [77] A. Othonos and K. Kalli, *Fiber Bragg Gratings (Fundamentals and Applications in Telecommunications and Sensing)*, Artech House, 1999

[78] B. J. Eggleton, P. S. Westbrook, C. A. White, C. Kerbage, R. S. Windeler, G. L. Burdge, "Cladding-mode-resonances in air-silica microstructure optical fibers," *Journal of Lightwave Technology*, Vol. 18, pp. 1084-1100, Aug. 2000

[79] <http://www.asiinstr.com/dc1.html>

Vita

Jeong Il Kim was born to Hong Gil Kim and Jeong Gon Koh in 1971 in Daejeon, South Korea. He graduated from MyungSeok High School, Daejeon, in 1990 and attended Chungnam National University, where he received the Bachelor of Science degree in electronics engineering in February 1996. He also continued for Master Program in the Chungnam National University and transferred as an exchange student to Virginia Polytechnic Institute and State University, where he received the Master of Science degree and the Doctor of Philosophy in electrical and computer engineering in 1999 and 2003, respectively.